2014

# SHAPE MEMORY BEHAVIOR OF SINGLE AND POLYCRYSTALLINE NICKEL RICH NICKEL TITANIUM ALLOYS

Irfan Kaya
*University of Kentucky*, irfankay5@gmail.com

**STUDENT AGREEMENT:**

I represent that my thesis or dissertation and abstract are my original work. Proper attribution has been given to all outside sources. I understand that I am solely responsible for obtaining any needed copyright permissions. I have obtained needed written permission statement(s) from the owner(s) of each third-party copyrighted matter to be included in my work, allowing electronic distribution (if such use is not permitted by the fair use doctrine) which will be submitted to UKnowledge as Additional File.

I hereby grant to The University of Kentucky and its agents the irrevocable, non-exclusive, and royalty-free license to archive and make accessible my work in whole or in part in all forms of media, now or hereafter known. I agree that the document mentioned above may be made available immediately for worldwide access unless an embargo applies.

I retain all other ownership rights to the copyright of my work. I also retain the right to use in future works (such as articles or books) all or part of my work. I understand that I am free to register the copyright to my work.

**REVIEW, APPROVAL AND ACCEPTANCE**

The document mentioned above has been reviewed and accepted by the student's advisor, on behalf of the advisory committee, and by the Director of Graduate Studies (DGS), on behalf of the program; we verify that this is the final, approved version of the student's thesis including all changes required by the advisory committee. The undersigned agree to abide by the statements above.

Irfan Kaya, Student

Dr. Haluk E. Karaca, Major Professor

Dr. James M. McDonough, Director of Graduate Studies

# SHAPE MEMORY BEHAVIOR OF SINGLE AND POLYCRYSTALLINE NICKEL RICH NICKEL TITANIUM ALLOYS

---

## DISSERTATION

---

A dissertation submitted in partial fulfillment of the
requirements for the degree of Doctor of Philosophy in the
College of Engineering
at the University of Kentucky

By
Irfan Kaya
Lexington, Kentucky

Director: Dr. Haluk E. Karaca, Professor of Mechanical Engineering
Lexington, Kentucky

2014

# ABSTRACT OF THE DISSERTATION

## SHAPE MEMORY BEHAVIOR OF SINGLE AND POLYCRYSTALLINE NICKEL RICH NICKEL TITANIUM ALLOYS


NiTi is the most commonly used shape memory alloy (SMA) and has been widely used for bio-medical, electrical and mechanical applications. Nickel rich NiTi shape memory alloys are coming into prominence due to their distinct superelasticity and shape memory properties as compared to near equi-atomic NiTi shape memory alloys. Besides, their lower density and higher work output than steels makes these alloys an excellent candidate for aerospace and automotive industry. Shape memory properties and phase transformation behavior of high Ni-rich $Ni_{54}Ti_{46}$ (at.%) polycrystals and Ni-rich $Ni_{51}Ti_{49}$ (at.%) single-crystals are determined. Their properties are sensitive to heat treatments that affect the phase transformation behavior of these alloys.

Phase transformation properties and microstructure were investigated in aged $Ni_{54}Ti_{46}$ alloys with differential scanning calorimetry (DSC) and transmission electron microscopy (TEM) to reveal the precipitation characteristics and R-phase formation. It was found that $Ni_{54}Ti_{46}$ has the ability to exhibit perfect superelasticity under high stress levels (~2 GPa) with 4% total strain after 550°C-3h aging. Stress independent R-phase transformation was found to be responsible for the change in shape memory behavior with stress.

The shape memory responses of [001], [011] and [111] oriented $Ni_{51}Ti_{49}$ single-crystals alloy were reported under compression to reveal the orientation dependence of their shape memory behavior. It has been found that transformation strain, temperatures and hysteresis, Classius-Clapeyron slopes, critical stress for plastic deformation are highly orientation dependent.

The effects of precipitation formation and compressive loading at selected temperatures on the two-way shape memory effect (TWSME) properties of a [111]-oriented $Ni_{51}Ti_{49}$ shape memory alloy were revealed. Additionally, aligned $Ni_4Ti_3$ precipitates were formed in a single crystal of $Ni_{51}Ti_{49}$ alloy by aging under applied

compression stress along the [111] direction. Formation of a single family of $Ni_4Ti_3$ precipitates were exhibited significant TWSME without any training or deformation. When the homogenized and aged specimens were loaded in martensite, positive TWSME was observed. After loading at high temperature in austenite, the homogenized specimen did not show TWSME while the aged specimen revealed negative TWSME.

KEYWORDS: NiTi; Shape memory alloys; Mechanical characterization; High strength shape memory alloy; Two-way shape memory effect

Irfan Kaya

Student's Signature

04/29/2014

Date

# SHAPE MEMORY BEHAVIOR OF SINGLE AND POLYCRYSTALLINE NICKEL RICH NICKEL TITANIUM ALLOYS

By

Irfan Kaya

Haluk E. Karaca

Director of Dissertation

James M. McDonough

Director of Graduate Studies

04/29/2014

This work is dedicated to my mother and father.

# ACKNOWLEDGEMENTS

Foremost, I would like to sincerely thank my advisor, Prof. Haluk E. Karaca, who provided his guidance to complete this research and thought me how to do scientific research. His willingness to dedicate his time so generously has been very much appreciated. He was always approachable when I had questions about the research. This dissertation could not have been made possible without his tremendous guidance and invaluable comments. I cannot thank him enough for his patient guidance and enthusiastic encouragement during my research.

I would also like to express my very great appreciation to my co-advisor, Prof. Yang-Tse Cheng, and committee members, Prof. Keith Rouch and Prof. Y. Charles Lu for their valuable suggestions and comments during this work.

A special thanks also go to Prof. Chumlyakov for providing single crystals and his valuable suggestions. I would also like to thank Prof. R. Kainuma and Dr. M. Nagasako for all their help on the TEM work and the valuable comments about the findings. My grateful thanks are also extended to Dr. Burak Basaran for his help to conduct the experiments.

I would also like to offer my special thanks to my lab-mates, Ali Sadi Turabi, Emre Acar, Sayed Saghaian, Peizhen Li, Mohammed Souri and Sesha Spandana Pulla. I also appreciate the generous help from Dr. Hirobumi Tobe for TEM experiments. Thanks also to the technicians of the mechanical engineering department for their help.

I would like to express my gratitude to my father, mother, and brothers for their constant support. Especially, many thanks go to my brother, Adnan Kaya, who encouraged me during my research.

Finally, I would like to thanks the Turkish Ministry of National Education, the NASA Fundamental Aeronautics Program, Supersonics Project and the NASA EPSCOR program for funding the project.

## Table of Contents

## List of Tables

## List of Figures

# 1 Introduction

## 1.1 Motivation and Purpose of the study

Ni-rich NiTi alloys are the most commonly used shape memory alloys and they been widely used for bio-medical, electrical and mechanical applications due to their high strength, good corrosion resistance and smooth surface properties as compared to equiatomic NiTi SMAs [1]. Recently, high Ni-rich NiTi SMAs are coming into prominence owing to their distinct superelasticity and shape memory properties [2]. It was reported that in high Ni-rich NiTi alloys stable superelasticity and shape memory effect can be obtained provided that special heat treatment conditions without any "additional training" were employed in contrast to equiatomic NiTi alloys [3].

Aging is a simple process to optimize and improve the mechanical properties of Ni-rich NiTi SMAs without any additional mechanical training [4]. It is well known that the precipitation and corresponding shape memory properties highly depend on aging temperature, aging time and cooling rate [5, 6]. NiTi alloys that contain more than 50.6 at.% nickel are sensitive to aging as compared to equiatomic NiTi SMAs due to the formation of precipitates by aging [7]. Ni-rich NiTi alloys could demonstrate two- and/or three-step ('multi-step') transformations after thermal processing due to precipitation formation [5, 8]. In Ni-rich NiTi SMAs, the Ni content of the matrix is an important factor to control the transformation temperatures and it can be altered by formation of Ni-rich precipitates [9]. The limited number of studies in high Ni-rich NiTi alloys have revealed that their shape memory properties are quite sensitive to heat treatments [10] and cooling rate [5].

In the past, highly Ni-rich NiTi alloys (>52 at. % of Ni) did not attract high interest due to the difficulties in forming and working [11]. Nowadays, researchers overcame these obstacles through the new hot rolling and fabrication methods for these alloys [12-14]. However, only limited number of studies exist on the mechanical properties of these Ni-rich NiTi SMAs [15]. To the best of my knowledge, no work has been conducted on the mechanical properties of high Ni-rich $Ni_{54}Ti_{46}$ alloy.

It is well known that the shape memory properties of NiTi alloys are highly orientation dependent [16-19]. Thus, SMA single crystals have highly anisotropic properties such as different shape memory and superelastic strains along certain directions that are very beneficial for sensor and actuator applications [20].

The highest recoverable strain in compression was observed in the [148] orientation amongst the [112], [100] and [111] orientations for aged single crystal $Ni_{50.8}Ti_{49.2}$ (at.%) alloys [21]. In the [001] orientation of NiTi alloys, slip deformation is minimized due to the lack of available slip systems [22].

NiTi shape memory alloys exhibit shape memory effect (SME) and superelastic behavior that are related to the reversible thermoelastic martensitic transformation [8]. In SME, the shape of the austenitic phase is remembered and the material should be deformed in martensite or thermally cycled under stress to observe reversible shape change. However, it is possible to train the material to observe shape change without the application of any external force. This behavior is called as two-way shape memory effect (TWSME). TWSME in shape memory alloys mostly refers to the reversible shape change with thermal cycling under zero stress. TWSME can be obtained by suitable thermomechanical processing [23, 24] when internal stresses, often formed by the

presence of precipitates or dislocations, bias martensite variants enabling a net shape change upon austenite to martensite phase transformation. Upon heating, the change in shape will be recovered by martensite to austenite transformation. Thus, the material has the ability to remember two different shapes that can be activated by temperature.

Aging of Ni-rich NiTi shape memory alloys at intermediate temperatures results in the formation of $Ni_4Ti_3$ precipitates [25]. It has been revealed that formation of $Ni_4Ti_3$ precipitates is the most useful methods for improving the TWSME property of NiTi alloys [26]. The aging under a constant applied stress induce the TWSME property through the formation of aligned precipitates which are result of applied stress [27]. In stress-free aging of $Ni_{51}Ti_{49}$, four families of $Ni_4Ti_3$ precipitates are produced. On the other hand, aging under compressive stress in the [111] direction of $Ni_{51}Ti_{49}$ single crystal leads to the creation of a single family of $Ni_4Ti_3$ precipitates [28-32].

In Ni-Ti based alloys, a few studies reported that the TWSME can be generated to have different shape recovery directions [33, 34]. When plastic strain is induced by deformation of martensite, the TWSME takes place in the direction of the preliminary deformation of martensite which is called “positive” TWSME [33]. The “negative” TWSME occurs after the deformation of austenite and the TWSME corresponding to the spontaneous shape change in the opposite direction of the preliminary deformation [34]. Although this property would be very useful in many practical applications such as actuators and sensors, not much attention is paid on gaining the fundamental understanding of this behavior.

Systematic shape memory effect tests as a function of applied stress and superelasticity tests as a function of temperature were conducted in compression. Phase

transformation was investigated in Ni-rich NiTi SMA with differential scanning calorimetry (DSC), X-ray diffraction (XRD) and transmission electron microscopy (TEM) to observe the influence of precipitates and R phase on the phase transformation behavior. Chapter 2 presents background information on SMAs. Experimental procedures are introduced in Chapter 3. In Chapter 4, the effects of aging and cooling rate on the transformation temperatures, strain, hysteresis, and R-phase were investigated in $Ni_{54}Ti_{46}$ (at.%) high Ni-rich NiTi alloys. Chapter 5 discusses the orientation effects on the shape memory behavior of Ni-rich $Ni_{51}Ti_{49}$ single crystals. Chapter 6 focuses on the effects of aging and compressive loading at selected temperatures on the two-way shape memory effect properties of a Ni-rich $Ni_{51}Ti_{49}$ single crystals along the [111] orientation. Finally, conclusions are provided in Chapter 7.

## 1.2 Objectives

The objectives of this study are to:

- Characterize the shape memory behavior of $Ni_{54}Ti_{46}$ (at.%) SMAs under compression as functions of stress and temperature to develop high strength SMAs which can operate at stress levels higher than 500 MPa.
- Understand the multi-step transformations in aged Ni-rich NiTi shape memory alloys.
- Investigate the effects of aging on the microstructure and formation of R-phase in Ni-rich $Ni_{54}Ti_{46}$ alloys.
- Reveal the effects of aging temperature, aging time and cooling rate on transformation hysteresis, temperatures and strain in Ni-rich $Ni_{54}Ti_{46}$ alloys.

- Understand the superelasticity and the shape memory behavior of Ni-rich $Ni_{51}Ti_{49}$ (at.%) single crystalline alloys.
- Reveal the orientation dependent shape memory behavior of $Ni_{51}Ti_{49}$ shape memory alloys.
- Investigate the influence of precipitates and dislocations on the two-way shape memory effect in $Ni_{51}Ti_{49}$ (at. %) single crystal alloys.

# 2 Background

## 2.1 History and Overview of Shape Memory Alloy (SMA)

The first shape memory behavior was found by A. Ölander in Au-Cd alloy in 1932 [35]. Later, Chang and Read observed shape memory effect in Au- 47.5 at. %Cd in 1951 [36]. The shape memory behavior of InTi and CuZn was reported in 1953 [37]. In early 1960s, William J. Buehler was a metallurgist at the Naval Ordnance Laboratory (NOL) worked on the equiatomic nickel–titanium (NiTi) alloys and discovered the SME in NiTi. This alloy was named Nitinol (**Ni**ckel **Ti**tanium **N**aval **O**rdnance **L**aboratory) by Buehler [38]. The SME was also found in Cu-Al-Ni alloy by Arbuzova and Khandros [39]. However, it should be noted that Cu-based SMAs are brittle in a polycrystalline state. On the other hand, the NiTi alloys have high ductility and good corrosion resistance.

Previously, the technology was not mature enough to give the exact form to alloy for practical applications [40]. Discrepancy among batches of Nitinol was a major problem to consider. Therefore, Buehler et al. focused on the Nitinol manufacturing process to overcome this problem [41, 42]. Since the development of manufacturing techniques, the intensive investigations have been done and the commercial use of Nitinol increased during the 1970s and 1980s. Nitinol was employed for couplings, bio-medical, actuators, sensors, heat engines, lifting devices, safety products and military products.

## 2.2 Shape Memory Alloy

The development of novel materials is very important for the advancement of materials engineering. The shape memory alloys are called active or multifunctional

material. In general, active materials give mechanical response when they are subjected to a non-mechanical field.

A high actuation frequency and energy density are very important properties of ideal active materials. The actuation energy densities and frequencies of some common active materials are given in Figure 2.1 and Figure 2.2 [43]. The actuation energy density that is shown by the dotted lines in Figure 2.1 is the product of the actuation strain with the actuation stress with the assumption is that the active material is operating under constant stress. The specific actuation energy density can be calculated from Figure 2.1 by dividing the actuation energy density by the mass density. While SMAs have high actuation energy densities as shown in Figure 2.1, they exhibit low frequency response as shown in Figure 2.2.

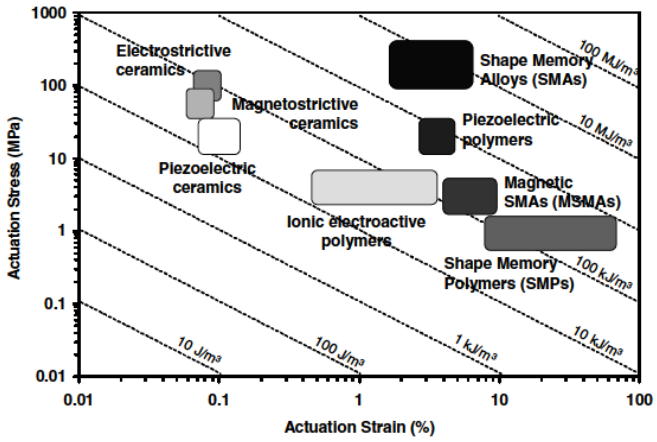


**Figure 2.1** Actuation energy density diagram indicating typical ranges of actuation stress, actuation strain, and the actuation energy densities of different active materials [43].

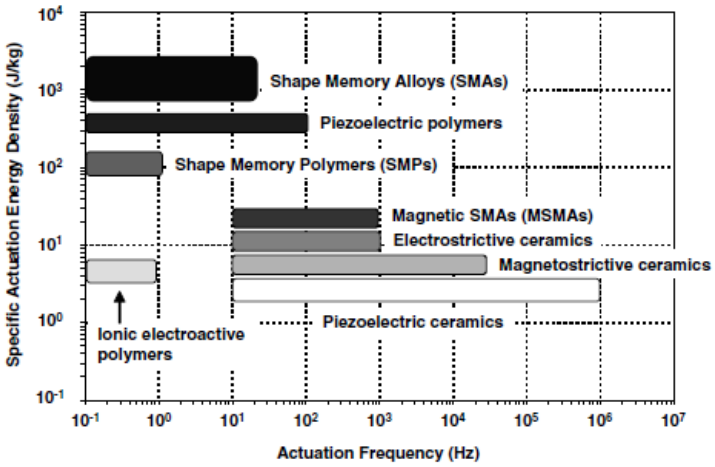


**Figure 2.2** Actuation frequency diagram comparing the actuation frequency ranges [43].

Shape memory alloys have two phases. The high temperature phase is called austenite and the low temperature phase is called martensite. These two phases have different crystal structures. In general, while austenite is cubic, martensite can be tetragonal, orthorhombic, and monoclinic. The transformation from one phase to other phase occurs by shear lattice distortion.

The forward transformation is the phase transformation from austenite to martensite. When the material is heated from martensite, the crystal structure transforms back to austenite which is called reverse transformation. During these phase transformations, there are four essential temperatures such as martensite start temperature ($M_s$), martensite finish temperature ($M_f$), austenite start temperature ($A_s$), and austenite finish temperature ($A_f$). These temperatures can be obtained from the Differential Scanning Calorimeter (DSC) which is given in Figure 2.3.

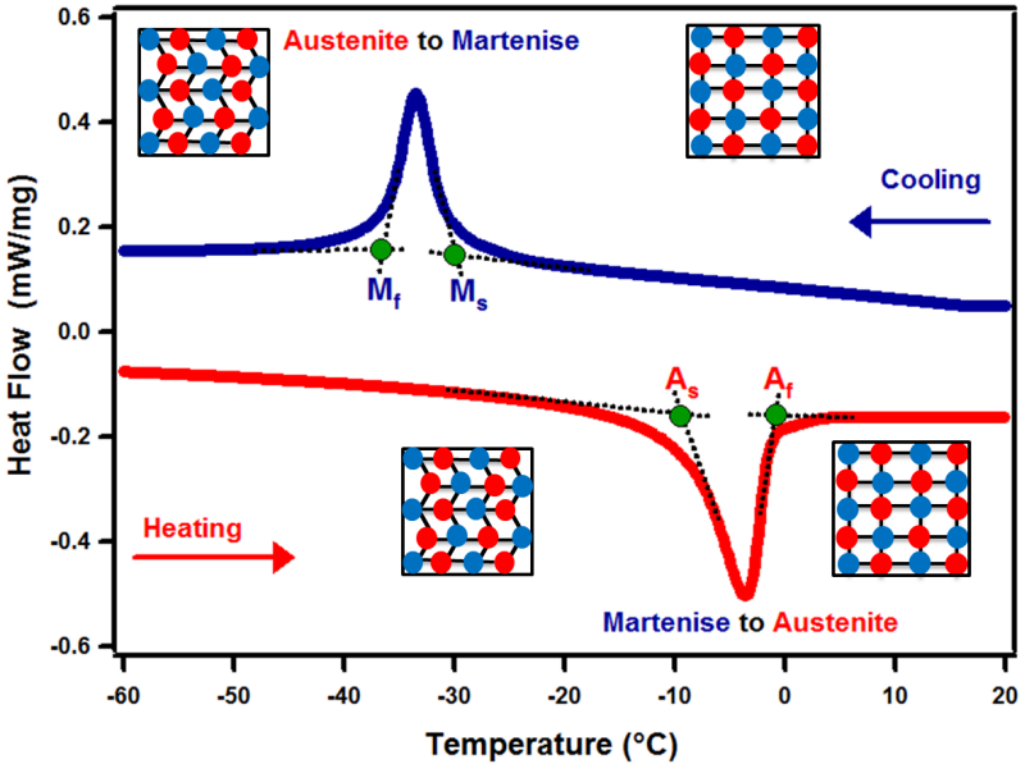


**Figure 2.3** DSC response of aged $Ni_{55}Ti_{45}$ SMA showing the transformation temperatures and associated latent heat of transformation during thermal cycling.

There are two essential phenomena for shape memory alloys; shape memory effect and superelasticity.

### 2.2.1 Shape Memory Effect

When the test specimen is deformed at a temperature below $A_s$, twinned martensite becomes detwinned martensite (A-B) and after unloaded (B-C) the induced strain cannot be fully recovered. Subsequent to heating it up to a temperature above $A_f$ (C-D), it recovers the retained strain as it transform to austenite which is shown in Figure 2.4.

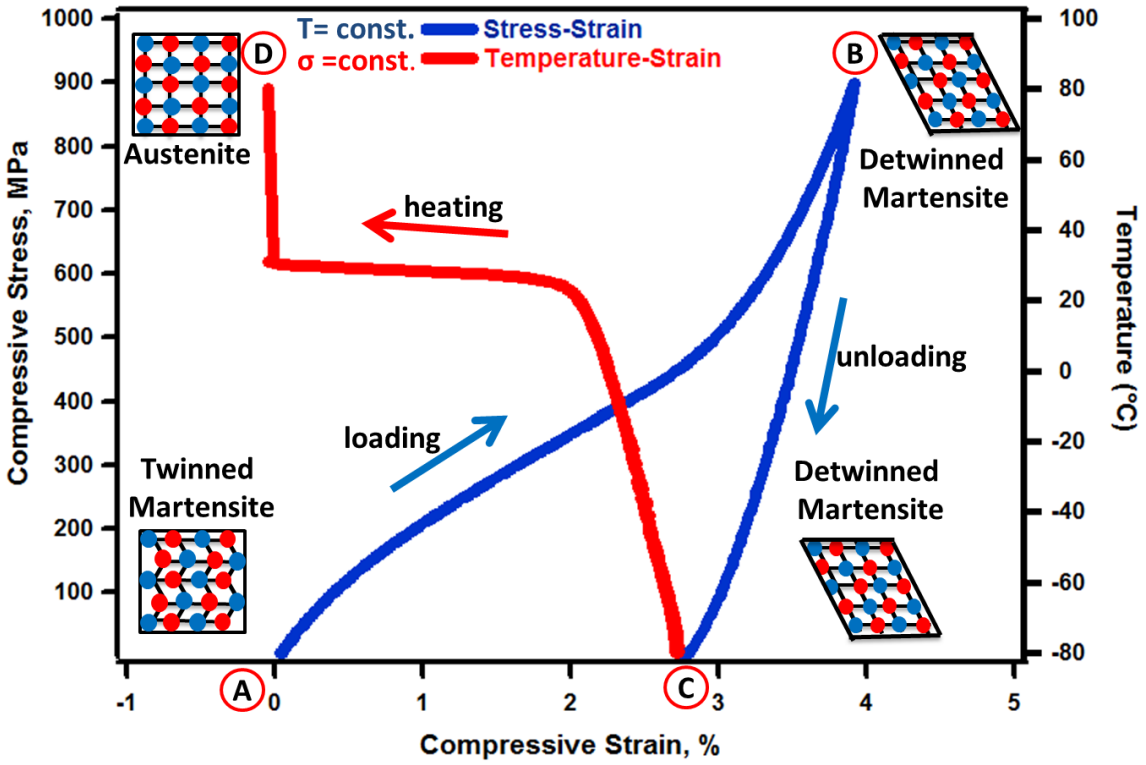


**Figure 2.4** Stress vs. strain and temperature vs. strain curves of aged $Ni_{51}Ti_{49}$ single crystal alloys.

### 2.2.2 Superelasticity

One of the commercial uses of shape memory alloy exploits the superelastic properties of the metal during the high-temperature, austenitic phase. The superelasticity (SE) is associated with stress-induced transformation. When the sample was loaded and unloaded at a temperature above $A_f$, superelastic behavior was observed with large recoverable strain (see Figure 2.5).

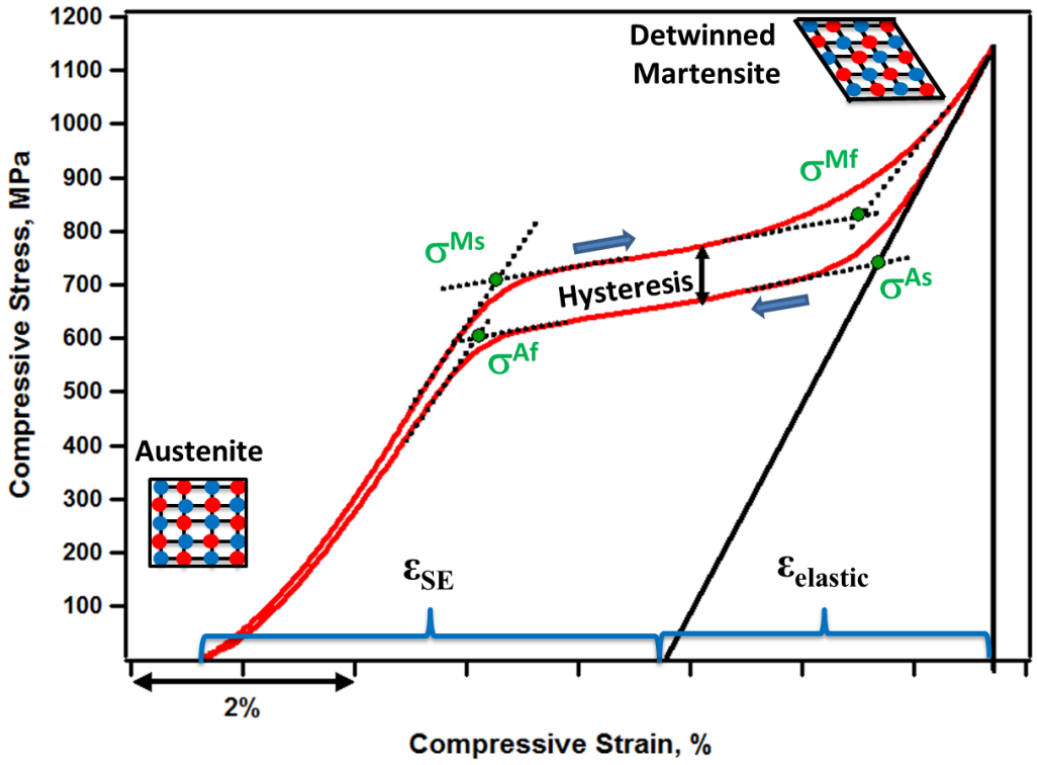


**Figure 2.5** A typical SMA superelastic cycle.

The $\sigma^{Ms}$ represents the critical stress which is the onset of stress-induced transformation from austenite to martensite. Transformation ends at $\sigma^{Mf}$. During unloading, back transformation from martensite to austenite starts at $\sigma^{As}$ and ends at $\sigma^{Af}$. Upon unloading, the SE strain is denoted by the $\varepsilon_{SE}$ while the elastic part of the strain is represented by $\varepsilon_{elastic}$. The stress hysteresis which is shown with vertical arrow in Figure 2.5 is found at the midpoint of plateau strain between the forward and back transformations.

## 2.3 Nickel Titanium Shape Memory Alloys

Nitinol is well known shape memory alloy by exhibiting strong shape memory effect, superelasticity and good mechanical properties under the right conditions [44].

### 2.3.1 Ni-rich Nickel Titanium Shape Memory Alloys

Ni-rich NiTi shape memory alloys are coming into prominence due to their distinct superelasticity and shape memory properties as compared to near equiatomic NiTi SMAs. If the alloy contains 52 at. % or more of Nickel, NiTi alloys are generally considered to be “high Ni-rich” NiTi SMAs [45]. High Ni-rich NiTi SMAs show many unique properties such as good corrosion resistance, smooth surface finish and high toughness [46]. Besides, its lower density than steel makes this alloy an excellent candidate for aerospace and automotive industries [45]. The NiTi alloys that contain more than 50.6 at.% nickel are sensitive to aging as compared to equiatomic NiTi SMAs due to the formation of precipitates by aging [7].

In Ni-rich alloys, $Ni_4Ti_3$ precipitates can be formed after aging at around 400 $^{o}$C. The R-phase appears between the austenite and martensite phases in Ni-rich NiTi shape memory alloys. The crystal structure of R-phase is rhombohedral. This phase generally disappears with heat treatments at high temperatures and thus its existence is associated with certain conditions [47].

### 2.3.2 Phase Diagram of NiTi Alloy

The NiTi phase diagram is crucial for heat-treatments of the alloys and advancement of the shape memory characteristics. Before the NiTi phase diagram was established, it has been controversial for approximately thirty years. Laves and Wallbaum found that NiTi was a single phase near the equiatomic composition at higher temperatures [48]. The decomposition of NiTi into $NiTi_2$ and $Ni_3Ti$ at 800 °C was first stated by Duwez and Taylor [49]. However, the similar decomposition was not found by Margolin et al. [50], and Purdy and Parr [51]. The solubility limit of the NiTi phase

above 900 °C metallographically was determined by Poole and Hume-Rothery in 1955 [52]. According to their result, the boundary on Ti-rich side is close to 50NiTi, and is steep. In contrast, on Ni-rich side, the solubility decreases greatly with lowering temperature. According to the proposed phase diagram by Purdy and Parr [51], the solubility limit on the Ni-rich side was similar to the Poole and Hume -Rothery's report [52]. They found that the NiTi phase transforms to π phase which is the reversible transformation. It was the first observation of martensitic transformation in the NiTi alloy. In 1963, Wasilewski et al. reported a new phase $Ni_3Ti_2$, and proposed a phase diagram, which involves a peritectoid reaction at 625 °C [53].

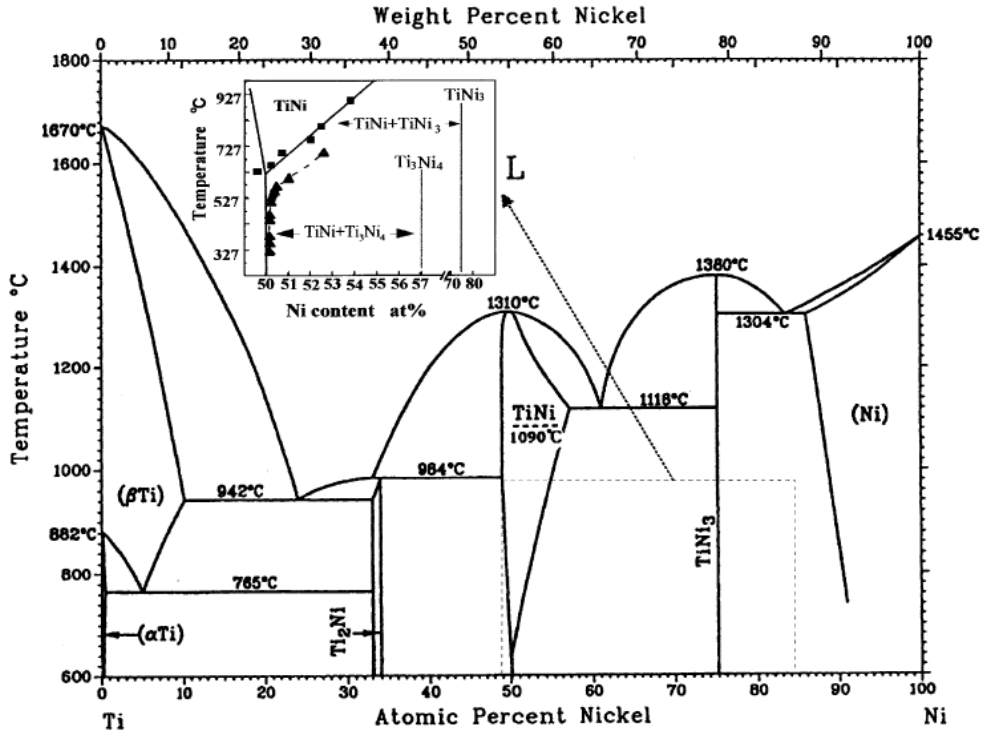


**Figure 2.6** Phase diagram of binary NiTi alloy [54][55].

Nishida et al. showed that three phases $Ni_4Ti_3$, $Ni_3Ti_2$ and $Ni_3Ti$ could appear depending upon aging temperature and time [56]. $Ni_4Ti_3$ appears at lower aging temperature and shorter aging time while $Ni_3Ti$ appears at higher aging temperature and

longer aging time and at intermediate temperature and time, $Ni_3Ti_2$ appears. They also report that the preexisted $Ni_4Ti_3$ is dissolved in the matrix by prolonged aging, and the number and size of $Ni_3Ti_2$ increase. After that, the number and size of the $Ni_3Ti$ increase with the $Ni_3Ti_2$ is absorbed into the matrix by prolonged aging. They confirmed that the $Ni_3Ti$ is the equilibrium phase while the both $Ni_4Ti_3$ and $Ni_3Ti_2$ are intermediate phases. $Ni_4Ti_3 \rightarrow Ni_3Ti_2 \rightarrow Ni_3Ti$ transformations occur which are summarized by time-temperature-transformation (TTT) diagram shown in Figure 2.7. Besides, the TTT diagram also shows the upper temperature limit for each precipitate. Kainuma et al. determined the TTT diagrams for the Ti–54Ni, Ti–56Ni and Ti–52Ni alloys [57]. According to Otsuka and Ren , the most reliable phase diagram of NiTi is as shown in Figure 2.6 which is similar to Massalski et al. [54].

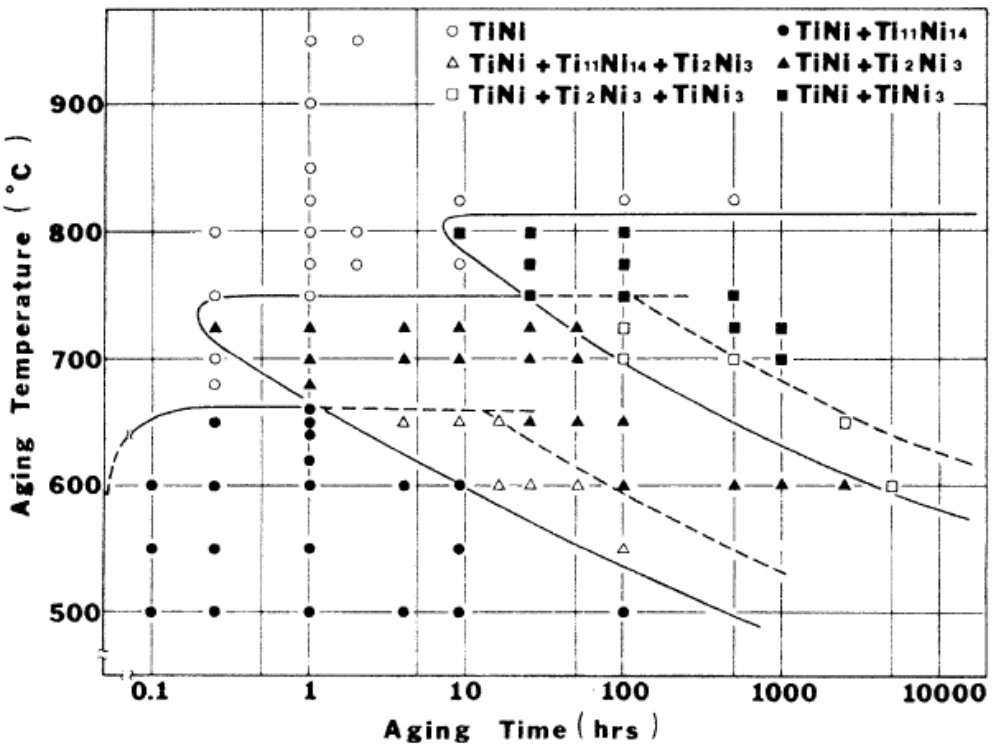


**Figure 2.7** TTT diagram describing aging behavior for Ti–52Ni alloy [7].

### 2.3.3 Effects of Nickel Composition

One of the most important parameters that governs the transformation temperatures in NiTi alloys is the Ni composition of the alloy. The martensite start temperature is directly related to Ni concentration, as shown in Figure 2.8 [58]. In Nickel rich NiTi alloys, even an increase in Ni composition by 1% decreases the $M_s$ by 100 °C (in solution-treated condition) [59, 60]. On the other side, the transformation temperature is almost composition independent on Ti-rich side.

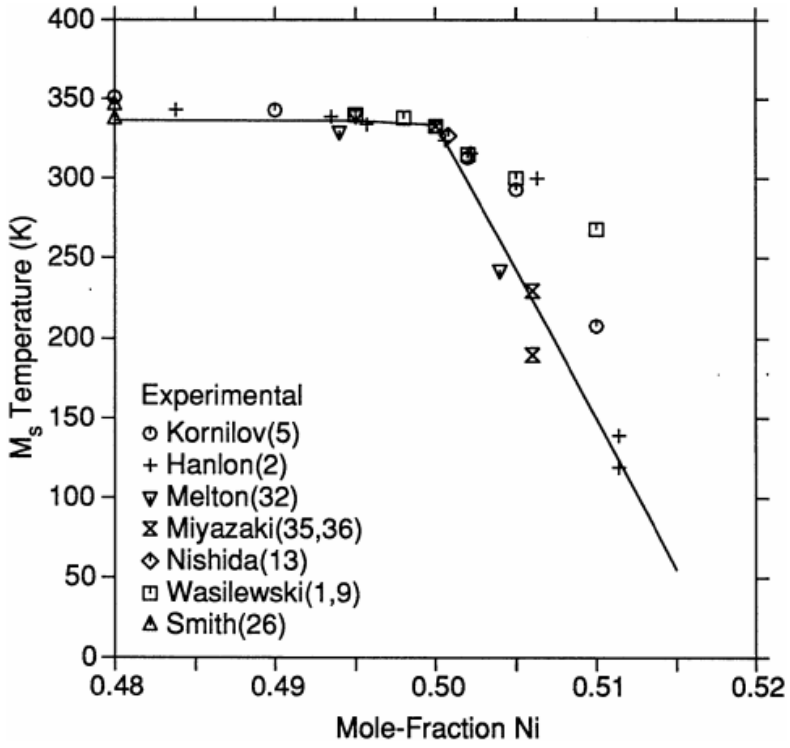


**Figure 2.8** $M_s$ temperature as a function of Ni content for NiTi SMAs [58].

### 2.3.4 Effects of precipitation in NiTi Shape Memory Alloys

Another major factor that affects the phase transformation temperatures in Ni-rich NiTi shape memory alloys is the formation of $Ni_4Ti_3$ precipitates. Ni-rich Ni-Ti shape memory alloys aged at intermediate temperatures form precipitates of the metastable $Ni_4Ti_3$ phase [25]. These precipitates have a lenticular shape (see Figure 2.9) and a rhombohedral structure [61]. These metastable precipitates could act as an obstacle for martensite nucleation and growth which is associated with high transformation strain [62]. The $Ni_4Ti_3$ metastable precipitates give rise to coherency stress fields [63, 64]. Also, the external stress applied during aging can favor the occurrence of certain $Ni_4Ti_3$ variants [65, 66]. In Ni-rich NiTi SMAs, the TTs increase after the formation of $Ni_4Ti_3$ precipitates that decreases the Ni concentration of the matrix [9]. The Precipitates are widely spaced with long-term aging and they do not directly affect martensitic transformations [67].

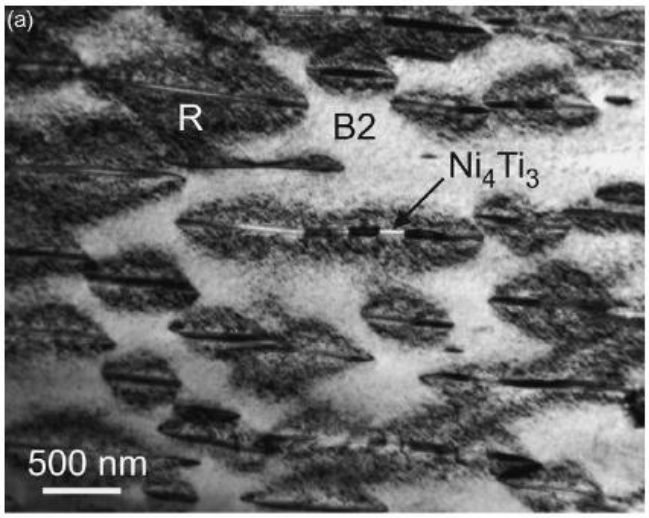


**Figure 2.9** TEM micrographs of the B2→R transformation in aged single crystal [14].

Small lenticular $Ni_4Ti_3$ precipitates form on and near grain boundaries and near oxide particles while the major part of the grain is free of precipitates after short aging time (3.6 ks) at 773 K (see Figure 2.10a) [68, 69]. Increasing the aging time to 36 ks results the precipitation formation in the interior of the grain (see Figure 2.10b) [69]. The coherent stress fields of the early small precipitates assist the nucleation of other precipitates in the interior of the grain.

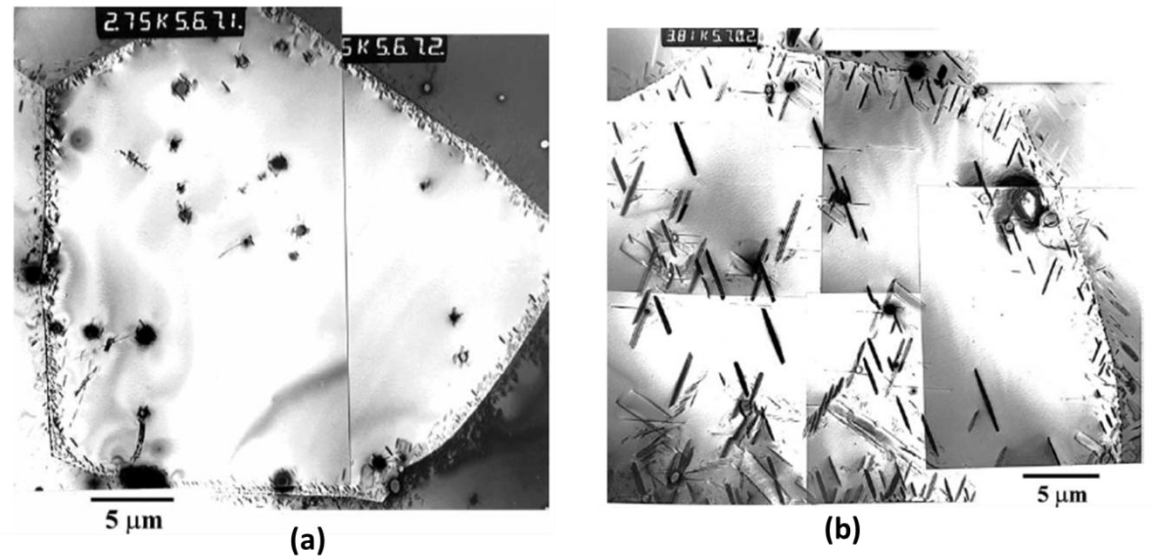


**Figure 2.10** TEM micrograph of the Ni-rich $Ni_{50.7}Ti_{49.3}$ (at.%) SMA after **a)** short aging time (773 K, 3.6 ks) **b)** long aging time (773 K, 36 ks) [69].

The aging of NiTi to create $Ni_4Ti_3$ precipitates provides some advantages such as increased austenite yield strength, two way shape memory effect and superelasticity [70]. On the other hand, the maximum transformation strain decreases as a result of the formation of untransformable precipitate formation [71]. In polycrystals, the precipitates may also hinder the process of detwinning that could result in less transformation strain [72].

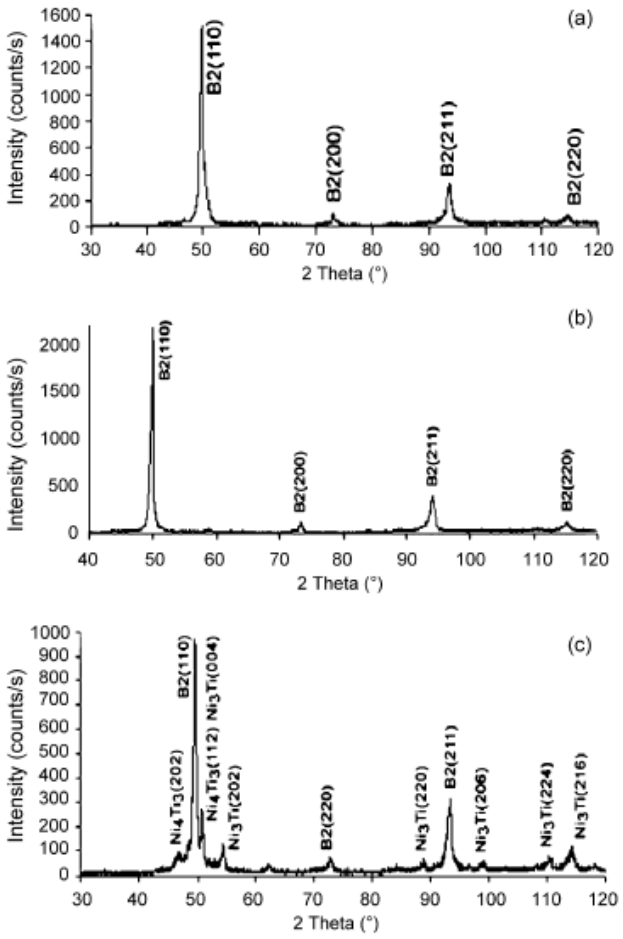


**Figure 2.11** X-ray diffraction analyses of the Ni-rich NiTi alloy cooled in different condition: **(a)** quench in dry-ice bath; **(b)** quench in water; **(c)** cooled in furnace [73].

The effects of cooling rate on the phase transformation temperature of Ni-rich NiTi alloy were investigated by Motemani et al. [73]. Various cooling techniques were employed such as; furnace cooling, water quenching and dry-ice bath quenching. According to their results, one phase (austenite, B2) was observed in samples cooled in the dry-ice bath and water (see Figure 2.11a and b), while the intermetallic phases ($Ni_4Ti_3$ and $Ni_3Ti$) were also seen in addition to austenite phase for furnace cooled sample (see Figure 2.11c). Therefore, we can conclude that the cooling rate affects the precipitates formation. It was also shown by Zang et al. that in NiTi SMAs, the decrease of the

cooling rate results the decrease of $M_s$ and $M_f$ temperatures due to formation of the precipitates [74].

### 2.3.5 Multiple-Stage Transformation

Changes in microstructure affect the shape memory behavior of NiTi shape memory alloys. After certain thermomechanical treatments or adding a third element, the transformation sequence can be changed from one-stage (B2-M) to two-stage (B2-R, R-M) transformation on cooling. The presence of the precipitates provides the resistance supporting the formation of R-phase and thus, a two-stage (B2→R→B19') martensitic transformation occurs in Ni-rich NiTi alloys [5, 75-77]. Moreover, in some cases more complicated transformation path of the R→B19' transition occurs due to the presence of $Ni_4Ti_3$ precipitates [5, 76, 77]. B2-R, R-M and B2-M transformations can be characterized by difference in of temperatures hysteresis and transformation energies.

A.J. Wagoner Johnson et al. examined the origin of the multi-step transformations on heating and cooling in single-crystal NiTi shape-memory alloys. While the effect of local composition on the multi-step transformations was shown, the work also confirms that inhomogeneous precipitation plays a dominant role in the multiple stage transformation [78].

### 2.3.6 R-Phase in NiTi Shape Memory Alloys

In Ni-Ti alloys under certain conditions, three transformations (B2→ M, B2→ R-phase, R-phase → M) are possible. In addition to B2 austenite to B19' martensite phase transformation, R-Phase can also be formed in NiTi alloys subsequent to cold working, aging of Ni-rich alloys and the addition of a third element [79]. It was reported that two-stage transformation observed in NiTi alloys is associated with the R-phase transition and

the martensitic transformation [80, 81]. H. Morawiec et al. reported that when the R-phase transition was present in the alloy, the final structure of the martensite did not change and remained monoclinic [82]. Large transformation hysteresis and large distortions are observed during the B2→ M and R→M whereas temperature hysteresis and distortions are small for B2→ R-phase transformation. The B2→R-phase transformation is characterized by a small temperature hysteresis (1-10°C) compared to the B2→B19' (20-50°C) [83]. During transformation, the large distortion implies a huge defect to the microstructure while the small distortion denotes a small defect to the microstructure. B2 to R-phase transformation results in quite a small transformation strain and temperature hysteresis in comparison to those of the martensitic transformation of monoclinic-B19' [10]. These unique properties of R-phase renders it very useful for small amplitude but the higher frequency actuator and damping applications [84].

The narrow hysteresis during B2→ R-phase transformation provides the capability of the high response rate and high reversibility that makes them promising for actuator and sensor applications [77].

The R-phase transformation can be obtained by several methods:

1- Cold working by annealing at low temperatures,

2- Addition of third element, such as iron,

3- Aging between 400°C and 500°C.

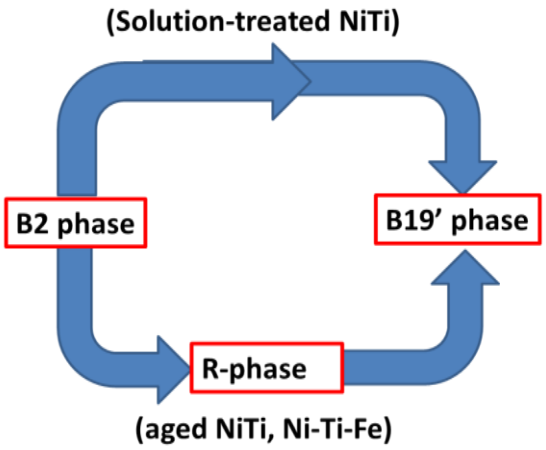


**Figure 2.12** Possible martensitic transformation paths in NiTi alloys.

The presence of the R-phase can be detected as double-peaks in the cooling cycle of a DSC scan as shown in Figure 2.13.

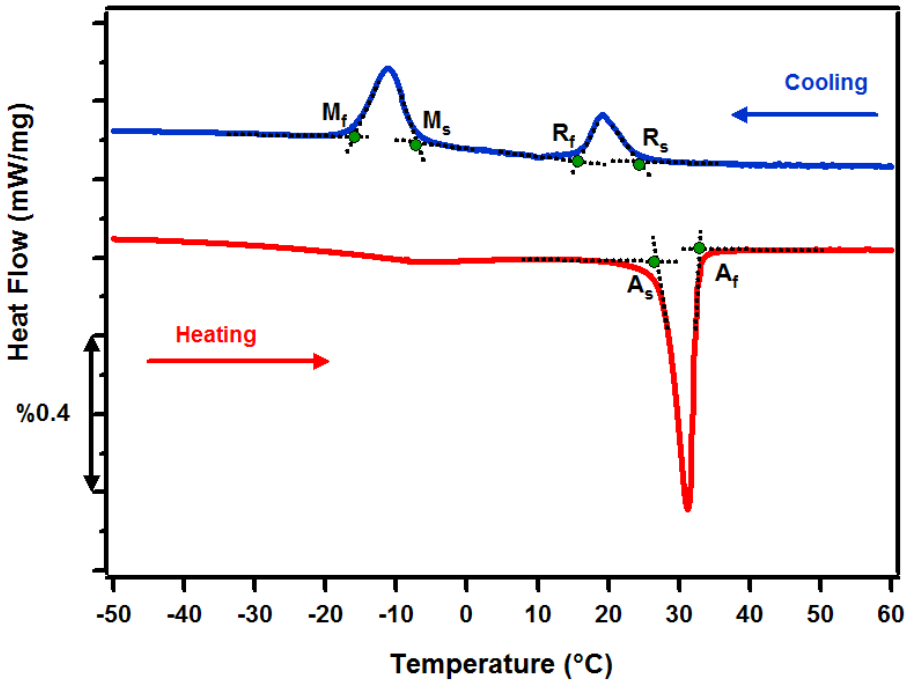


**Figure 2.13** R-phase transformation identified on a DSC response of aged Ni-rich $Ni_{51}Ti_{49}$ SMA.

The shape memory and superelastic effects are observed by B2→R-phase transformation which confirms the thermoelastic nature of transformation [47]. The crystallography of B2 to R-phase and the subsequent R-phase to B19 martensite transitions was stated by Xiangyang Zhang and Huseyin Sehitoglu [85]. T. Fukuda et al. stated that a $Ni_{51}Ti_{49}$ (at.%) alloy with aligned $Ti_3Ni_4$ precipitates formed by aging under an applied stress shows an anomalous transformation [86]. According to their study, stress induced R to B2 transformation occurs in this alloy since thermally induced R-phase variants are preferable for the stress field formed by the aligned particles. However, these variants are not preferable for the applied stress.

Jafar Khalil-Allafi et al. worked on multiple-step martensitic transformations in a $Ni_{51}Ti_{49}$ (at.%) single crystal. According to their study, $M_s$ and $A_s$ temperatures increase with increasing aging time due to Ni depletion of the matrix. After 45 min of aging time, $R_s$ reaches a constant value (see Figure 2.14). It might be related to the nucleation of the R-phase at the interface between B2 matrix and $Ni_4Ti_3$ precipitates, where the Ni content of the B2 matrix adjacent to the precipitate is constant for different aging times [87].

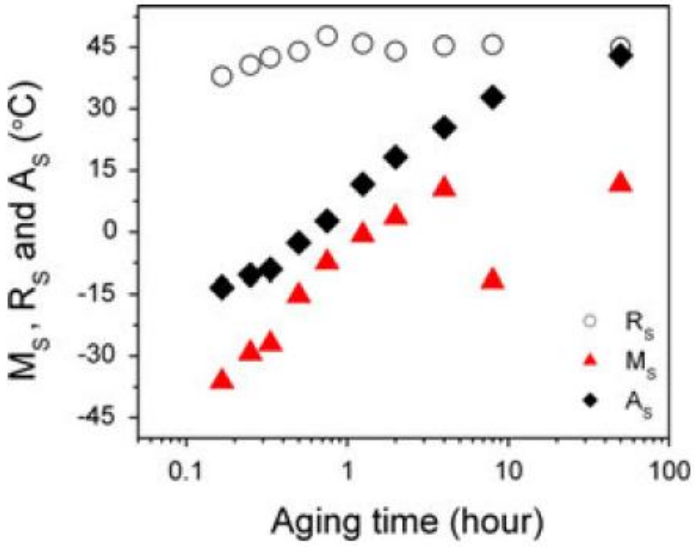


**Figure 2.14** Transformation temperatures versus aging time for NiTi alloy [87].

### 2.3.7 Two-Way Shape Memory Effect

Two-way shape memory effect represents the reversible and a spontaneous shape change of materials with thermal cycling without application of external stress. TWSME is the unique property when SMAs are applied as the actuator. It is well known that TWSME property is not intrinsic to SMAs while it can be obtained commonly after specific shape memory [88], pseudoelastic [89], and thermal cycling under a constant stress [90, 91] training methods. Once that the material has learned the behavior, it is possible to modify the shape of the material, in a reversible way between two different shapes without applying stress or load, only by changing the temperature across $A_f$ and $M_f$. TWSME is a useful property that can be achieved in both Ni-rich and near equiatomic NiTi SMAs.

The two main mechanisms for TWSME are attributed to either residual stresses induced in matrix by dislocation arrays or on retained (stabilized) martensite [92-95]. Perkins revealed that TWSME takes place as a result of a macroscopic non-uniform

residual stress field, concluding that plastic deformation was necessary to observe TWSME [96]. Enami et al. reported that complex dislocation arrays are generated by thermomechanical cycling during the training procedure [29]. They assumed that these dislocations are responsible for TWSME because of the residual strain of stress fields which they generated. The magnitude of TWSME depends heavily on the microstructural properties such as dislocations, orientation of martensite variants and internal stress [97]. An optical microscopy study has suggested that the martensite nuclei retained after a partial transformation to austenite on heating, are responsible for the formation of preferential martensite variants on subsequent cooling [98]. It is commonly accepted that the generation of an anisotropic dislocation structure into the parent phase matrix during training processes create an anisotropic stress fields that help to formation of preferentially oriented martensite variants. As a result of these oriented martensite variants reversible shape changes occurred during thermal cycle [29, 99].

Ni-rich $Ni_4Ti_3$ precipitates that play an essential role in two-way shape memory are formed during aging at intermediate temperatures in Nickel rich NiTi [25]. Internal stress fields that control the growth of the martensite variants providing TWSME are produced by these Ni-rich precipitates [26, 97, 98].

When the sample undergoes a thermal cycling at constant stress as a part of the training procedure, it induces stress-assisted two-way memory effect (SATWME) in which martensitic transformation would be assisted by the external stress [100]. The magnitude of TWSME and SATWME depends heavily on the microstructural change such as dislocations, reorientation of martensite variants and internal stress [97]. The optical microscopy study has suggested that the martensite nuclei retained after a partial

transformation to austenite on heating, are responsible for the formation of preferential martensite variants on subsequent cooling [101]. On heating to above austenite finish temperature under a constant load showed an increasing fraction of retained martensite together with a portion of permanent strain generated at the end of each thermal cycle [102]. There is also experimental evidence showing that the amount of retained martensite variants increases as the number of thermomechanical cycling increases and these retained variants aide in the development of TWSME [88].

# 3 Experimental Procedures

## 3.1 Polycrystalline Sample Preparation

Vacuum Arc Melted $Ni_{54}Ti_{46}$ (at.%) rods were obtained from Sophisticated Alloys, Inc. The $Ni_{54}Ti_{46}$ ingots were contained in Argon filled quartz ampoules and homogenized at 1000℃ for 4 hours and quenched in water. Solution heat treatment refers to the process of dissolving precipitate phases created during the casting and/or hot-rolling process without melting the matrix. The solution heat treatment temperatures were selected based on the binary Ti-Ni phase diagram. Following homogenization, they were aged at various temperatures for 3 hours. Aged SMAs were cooled down by water quenching (WQ) or furnace cooling (FC) with a rate of 2 °C/min. Lindberg/Blue M BF5114841 box furnace (Figure 3.1) was used for heat treatments.

**Figure 3.1** Lindberg/Blue M BF5114841 box furnace.

## 3.2 Single Crystalline Sample Preparation

Single crystalline samples of $Ni_{51}Ti_{49}$ were prepared by using the Bridgman method in a He atmosphere. Compression specimens were cut by Electro Discharge Machine (EDM) (Figure 3.2.). The $Ni_{51}Ti_{49}$ single crystalline specimens were solution treated at 1000℃ for 2 hours in argon atmosphere in quartz tubes, followed by quenching into water. After specimens were homogenized, they were aged at selected temperatures.

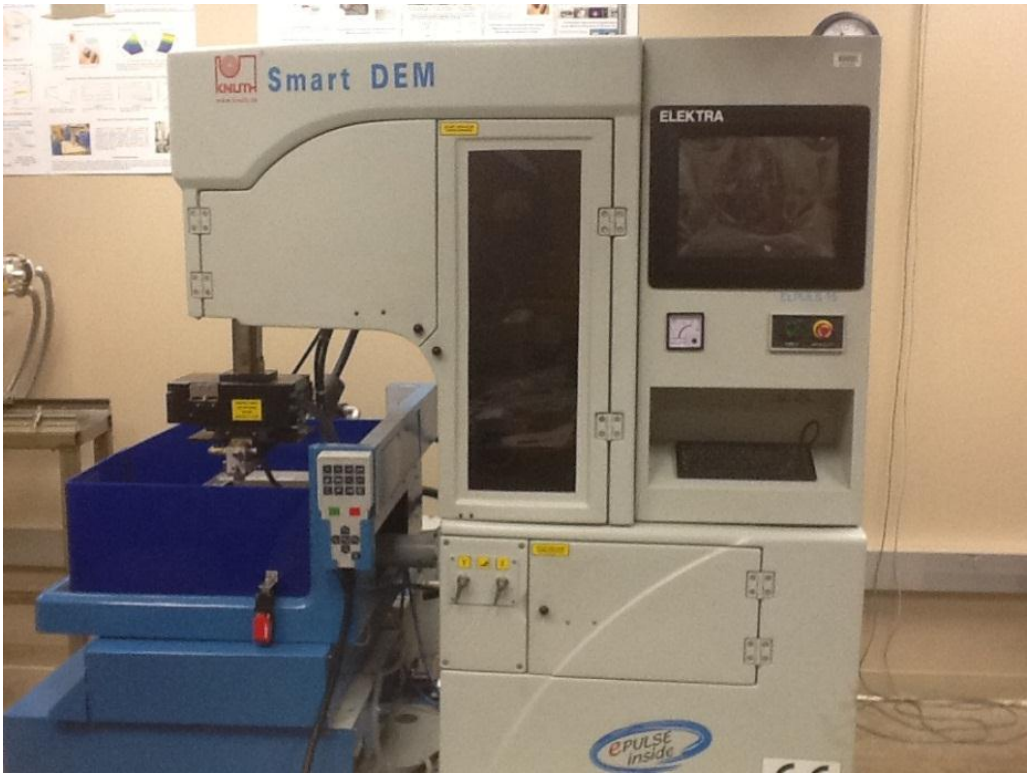


**Figure 3.2** Electro Discharge Machine.

## 3.3 The Differential Scanning Calorimeter and Transmission Electron Microscopy

Transformation temperatures of the material were determined by Perkin Elmer Pyris 1 differential scanning calorimetry (DSC) (Figure 3.3) with a heating/cooling rate of 10℃/min in He atmosphere. The microstructure after aging was investigated by

transmission electron microscopy (TEM). The thin foil specimens for TEM were prepared by the twinjet electropolishing device in a solution consisting of (all vol. %) 8% perchloric acid, 72% acetic acid, 12% methanol and 8% ethylene glycol at room temperature. TEM observations were carried out by JEOL JEM-2100HR (and HC) operated at an acceleration voltage of 200kV.

**Figure 3.3** Perkin-Elmer Pyris 1 Differential Scanning Calorimetry.

### 3.4 Hardness Test

Vickers hardness values were determined by using Sun-Tec model FM-7 microhardness test equipment (Figure 3.4). Before the hardness test, samples are placed in epoxy and polished. Hardness tests were performed with a 100 gf force and 15 seconds dwell time. Hardness test was conducted ten times for each sample. The lowest and the

highest values were omitted and the average of the rest eight values was taken as a final hardness result of samples.

**Figure 3.4** Sun-tec model FM-7 microhardness test equipment.

## 3.5 Mechanical Testing

Compression specimens with dimensions of 4mm x 4mm x 8mm were tested by 100 kN MTS Landmark servo-hydraulic load frame with a strain rate of $10^{-4}$ $s^{-1}$ (Figure 3.5). The temperature of the sample was monitored by K-type thermocouples attached on the sample and grips. Omega CN8200 series temperature controller was used to govern a heating rate of 10℃/min and a cooling rate of 5℃/min.


**Figure 3.5** MTS Landmark servo-hydraulic machine.

### 3.6 XRD analysis

X-ray diffraction (XRD) measurements to reveal the lattice parameters were carried out on a Bruker AXS D8 DISCOVER diffractometer using Cu Kα radiation (Figure3.6). The highly polished specimens were scanned at room temperature to capture the crystalline structure of the samples.


**Figure 3.6** Bruker AXS D8 DISCOVER diffractometer.

# 4 Shape Memory Behavior of Ultra High Strength Highly Ni-rich $Ni_{54}Ti_{46}$ Shape Memory Alloys

## 4.1 Introduction

In this chapter, shape memory properties of highly Ni-rich $Ni_{54}Ti_{46}$ alloys are determined. Shape memory behavior as a function of applied stress and superelasticity behavior as a function of temperature tests were conducted in compression. The effects of aging on transformation temperatures, strain and hysteresis; microstructure and formation of R-phase were revealed.

DSC, hardness, XRD, TEM and compression test (thermal cycling under stress and superelasticity) were carried out. The $Ni_{54}Ti_{46}$ alloys were selected for investigation since they exhibit higher strength and more stable behavior than near equiatomic NiTi. In this chapter, all The $Ni_{54}Ti_{46}$ ingots were homogenized at 1000℃ for 4 hours in argon atmosphere in evacuated quartz tubes, followed by quenching into water.

## 4.2 DSC Results

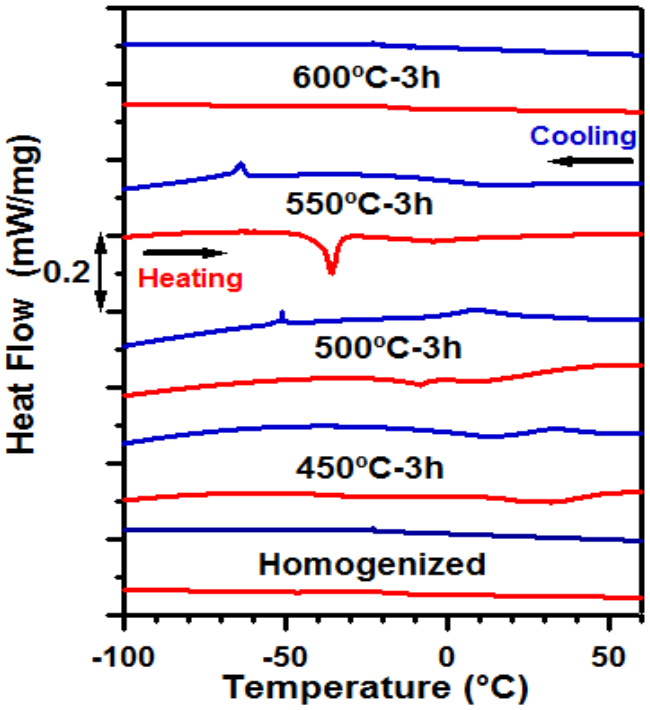


**Figure 4.1** DSC curves of homogenized and aged $Ni_{54}Ti_{46}$ alloys.

The effects of aging temperature on transformation temperatures are investigated by using DSC. Changes in the sample that are related with endothermic or exothermic reaction cause a change in the differential heat flow that is then recorded as a peak. Figure 4.1 depicts the heating (bottom) and cooling (top) DSC curves of homogenized and aged (between 450°C and 600°C for 3 h) $Ni_{54}Ti_{46}$. The TTs were determined by using the intersection method. In Figure 4.1, transformation peaks are not observed for the homogenized sample, even when it is cooled down to -160°C. After 450°C aging, only R-phase was observed with $R_s$ = 47°C and $R_f$ =17°C. In contrast, the specimen exhibited a multiple transformation peaks after aging at 500°C for 3 hours. While the first peak during cooling is attributed to the R-phase formation, the second peak during

cooling can be attributed to the B19' martensite formation. The TTs were; $R_s$ = 25°C, $R_f$ = 4°C, $M_s$ = -47°C, $M_f$ = -53°C, $A_s$ = -12°C, $A_f$ = -3°C. The TTs for 550°C-3h aged specimen were; $M_s$ = -61°C, $M_f$ = -66°C, $A_s$ =-40°C, $A_f$ = -33°C. Transformation peaks were not observed after 600C-3h aging.

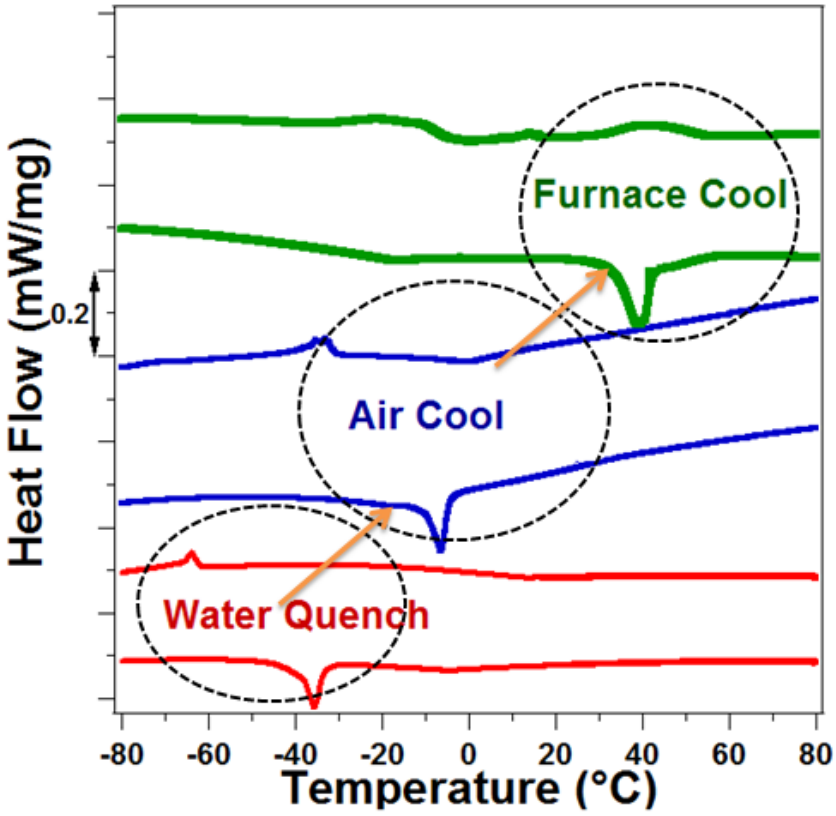


**Figure 4.2** DSC curves of the $Ni_{54}Ti_{46}$ alloy aged at 550°C for 3 hours and then cooled down by different rates.

Figure 4.2 shows the DSC results of homogenized and 550°C-3h aged $Ni_{54}Ti_{46}$ samples. In order to determine the effects of cooling rate (CR), the samples were aged at 550°C for 3 hours and then cooled down by three methods; water quenching (WQ), air cooling (AC) and furnace cooling (FC) where 2°C/min cooling rate was applied for

furnace cooling. TTs obtained from Figure 4.2 are given in Table 4.1. The decrease in cooling rate after 550°C aging increased the TTs and also broadened the peaks. The decrease in cooling rate promoted the formation of Ni-rich $Ni_4Ti_3$ precipitates, which in turn decreased the Ni concentration of the matrix [5]. Since the TTs of Ni rich Ni-Ti alloys decrease with the increasing Ni content of matrix, lower Nickel content of the matrix after 550°C-FC samples resulted in an increase in TTs [103]. In 550°C-FC, the first peak during cooling at about 40°C was attributed to the R-Phase formation. The other two peaks during cooling can be attributed to the B2-B19' or R-B19' martensite transformations due to inhomogeneity in microstructure [104]. Upon heating, B19'-R-B2 or B19'-B2 transformations occurred at temperatures very close to each other. R-peak in heating manifests itself in the shape of a shoulder in Figure 4.2 that is consistent with the work of Genlian Fan et al. who provided the detailed multi-stage martensitic transformation information [105]. It is clear that the cooling rate affects the thermal hysteresis. The highest hysteresis of 95 °C ($A_f$-$M_f$) is observed with the lowest cooling rate which is the FC sample.

**Table 4.1** Phase transformation temperatures for 550°C aged samples.

| **TTs (°C)** / **CR** | **$R_s$** | **$R_f$** | **$M_s^I$** | **$M_f^I$** | **$M_s^{II}$** | **$M_f^{II}$** | **$A_s$** | **$A_f$** |
|---|---|---|---|---|---|---|---|---|
| **WQ** | - | - | -61 | -66 | - | - | -40 | -33 |
| **AC** | - | - | -38 | -30 | -65 | -74 | -21 | -4 |
| **FC** | 56 | 31 | 20 | 11 | -3 | -38 | 32 | 57 |

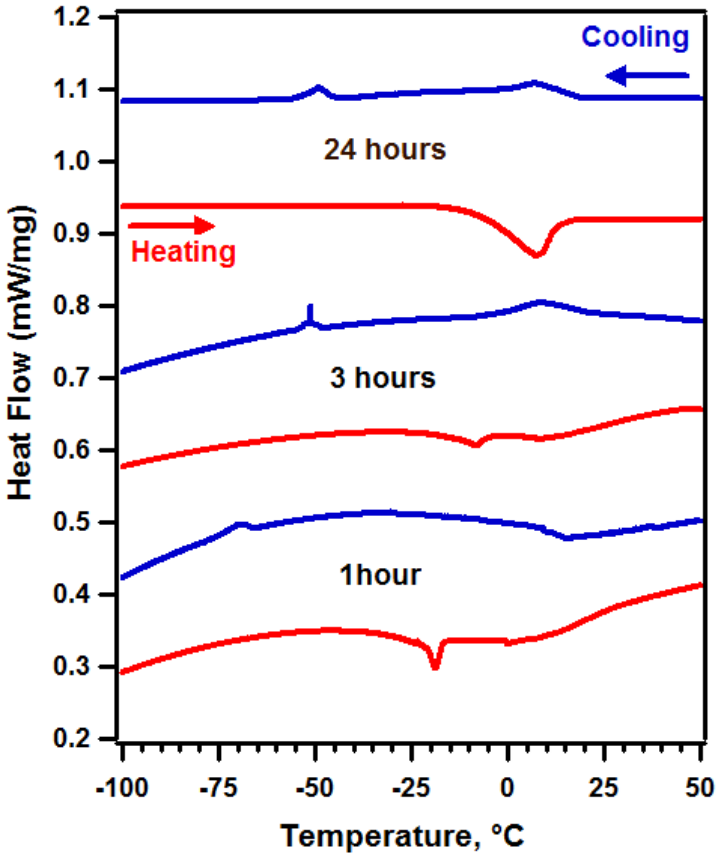


**Figure 4.3** DSC curves for $Ni_{54}Ti_{46}$ alloy aged at 500°C for various durations. It shows the effects of aging time on the martensitic transformation.

Aging time also influences the formation of $Ni_4Ti_3$ precipitates in Ni-rich NiTi alloys. Therefore, the Ni content of the matrix changes with aging time and the forward and reverse phase transformation temperatures such as $M_f$ and $A_f$ are shifted [55, 103]. Figure 4.3 shows the effects of aging time on the TTs. The sample was aged at 500°C for various time periods from 1 hour to 24 hours. The TTs increase with increasing aging time where $M_s$ was -66°C, -47°C and -43°C after aging at 500°C for 1hour, 3 hours and 24 hours, respectively.

## 4.3 XRD Results

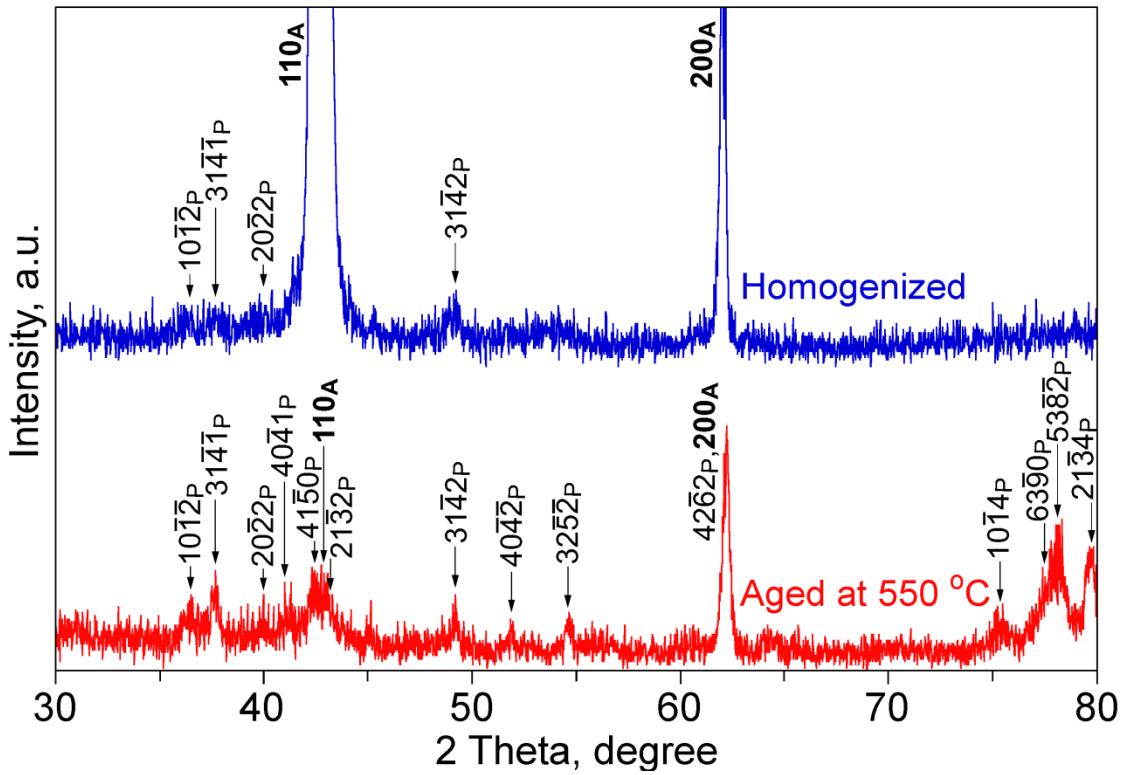


**Figure 4.4** X-ray diffraction patterns obtained at room temperature for the homogenized and 550°C-3h aged $Ni_{54}Ti_{46}$ alloys. Subscripts A and P indicate B2 austenite and $Ni_4Ti_3$ precipitate, respectively.

Figure 4.4 shows the XRD profiles of the homogenized and aged (550°C-3h) $Ni_{54}Ti_{46}$ alloys. In both homogenized and aged specimens, strong diffraction peaks are observed at about 42.5° and 62° which correspond to the austenite phase with cubic B2 structure while the other smaller peaks are indexed as $Ni_4Ti_3$ precipitate. Aging at 550 °C for 3 hours did not affect the crystal structure of the precipitate. There are no peaks corresponding to the $Ni_3Ti_2$ and $Ni_3Ti$ precipitates in the aged specimen, indicating that the transformations from the metastable $Ni_4Ti_3$ precipitates to $Ni_3Ti_2$ and $Ni_3Ti$ precipitates did not occur after 550 °C-3h aging. The lattice parameters of B2 (austenite)

were; a = 0.2991 nm and a = 0.2983 nm for homogenized and 550°C-3h aged $Ni_{54}Ti_{46}$ alloys, respectively. Additionally, the lattice parameters of $Ni_4Ti_3$ precipitates were: a =1.127 nm and c = 0.5084 nm for 550°C-3h aged $Ni_{54}Ti_{46}$ alloy.

## 4.4 TEM Results

Figure 4.5a shows the bright field TEM image and the corresponding selected area diffraction (SAD) pattern for the homogenized specimen. In the SAD pattern, there are superlattice reflections in addition to the fundamental reflections of the austenite phase; the 1/7 $<321>_{B2}^{*}$ superlattice reflections are the characteristic of $Ni_4Ti_3$ precipitates. Figure 4.5b shows the dark field image obtained using the superlattice reflection arrowed in the SAD pattern in Figure 4.5a. It is clear that fine $Ni_4Ti_3$ precipitates with about ~10-30 nm in size are homogeneously distributed in the specimen. The fine $Ni_4Ti_3$ precipitates are considered to be formed very rapidly during water quenching due to the high excess of Ni in the austenite matrix. Figure 4.5c shows the bright field image and the corresponding SAD pattern for the specimen aged at 550°C for 3h. The $Ni_4Ti_3$ precipitates grew after 550°C-3h aging and high density of lenticular precipitates were observed on $\{111\}_{B2}$ planes.

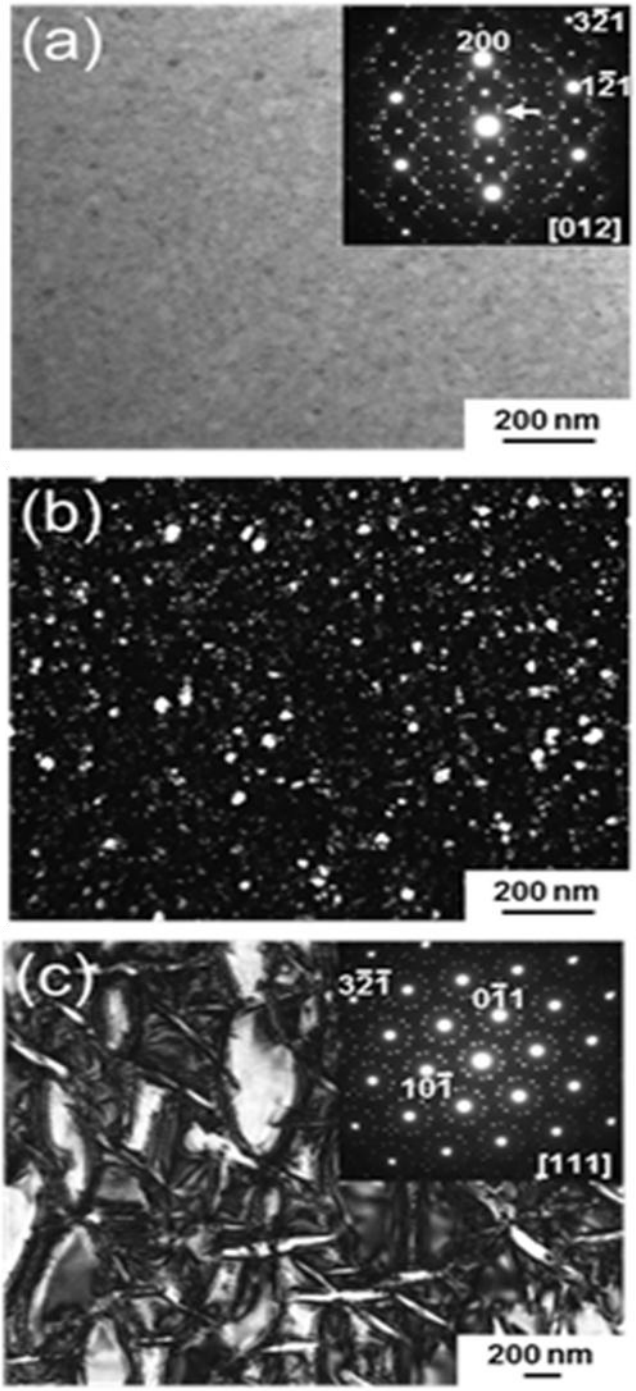


**Figure 4.5 (a)** Bright field image with the corresponding SAD pattern of the homogenized $Ni_{54}Ti_{46}$ alloy and **(b)** its dark field image to show $Ni_4Ti_3$ precipitates. **(c)** Bright field image with the corresponding SAD pattern of the 550°C-3h aged $Ni_{54}Ti_{46}$ alloy.

In order to investigate the effects of aging temperature on the volume fraction of $Ni_4Ti_3$ precipitates, TEM observations were conducted for the specimens aged at 500°C and 550 °C from the direction close to $[110]_{B2}$. Figures 4.6a and b are the dark field images of the specimens aged at 500°C and 550°C, respectively, showing the regions where only a single variant of $Ni_4Ti_3$ precipitates was observed. The bright and dark regions in Figure 4.6a correspond to the austenite matrix and $Ni_4Ti_3$ precipitates, respectively, while they are vice versa in Figure 4.6b. It should be noted that some precipitates are overlapping along the $[110]_{B2}$ direction in both dark field images. The volume fractions of $Ni_4Ti_3$ precipitates were calculated using the thicknesses of precipitates and interparticle distances following the method described by Michutta et al. [106]. The volume fraction of the $Ni_4Ti_3$ precipitates determined for the 500°C aged specimen was ~55% while it was ~43% for the 550°C aged specimen. It can be concluded that lower temperature aging results in a higher volume fraction of precipitates.

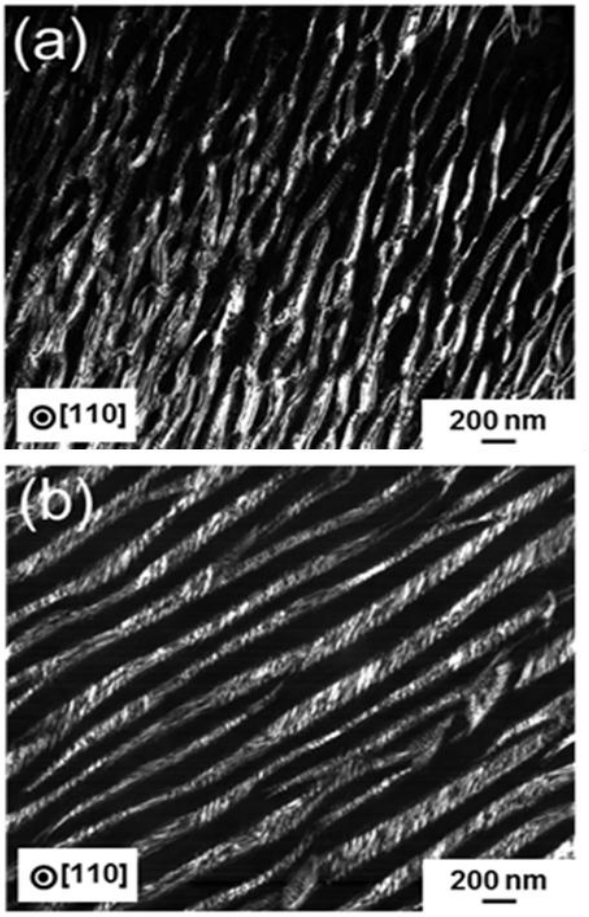


**Figure 4.6** Dark field images of the **(a)** 500°C-3h aged $Ni_{54}Ti_{46}$ obtained using a $<001>_{B2}^{*}$ reflection and **(b)** 550°C-3h aged $Ni_{54}Ti_{46}$ obtained using one of 1/7 $<321>_{B2}^{*}$ reflections.

Figures 4.7a and 4.7b show the bright field TEM image of the 550°C-3hr-FC sample and the corresponding selected area diffraction (SAD) pattern at room temperature, respectively. In Figure 4.7a, bright regions correspond to $Ni_4Ti_3$ precipitates. The length of the longitudinal direction of the lenticular $Ni_4Ti_3$ precipitates varies from 200 nm to 600 nm, approximately. There are sharp superlattice reflections in Figure 4.7b at 1/7 positions along $<321>_{B2}$* in reciprocal space, which correspond to $Ni_4Ti_3$ precipitates. Besides, we can see the superlattice reflections at 1/3 positions and 1/2

positions along <110>$_{B2}$*, which are indicated by single and double arrows, respectively. The 1/3 <110>$_{B2}$* reflections correspond to R-phase while the 1/2 <110>$_{B2}$* reflections correspond to B19′ martensite phase. This result is consistent with the DSC result shown in Figure 4.2 that R-phase and B19′ martensite phase transformation peaks were observed in the FC sample. By means of the high resolution TEM, it was confirmed that there is also the retained austenite phase in the microstructure in addition to the R-phase and B19' martensite phase. It can be argued that aging and furnace cooling might have promoted the formation of Ni-rich $Ni_4Ti_3$ precipitates, which in turn depleted the Ni concentration of the matrix [5]. The precipitates do not undergo phase transformation and since the TTs of Ni-rich Ni-Ti alloys decrease with the increasing Ni content of matrix, after 550°C-3hr-FC treatment the lowered Ni content of the matrix resulted in an increase of TTs [103].

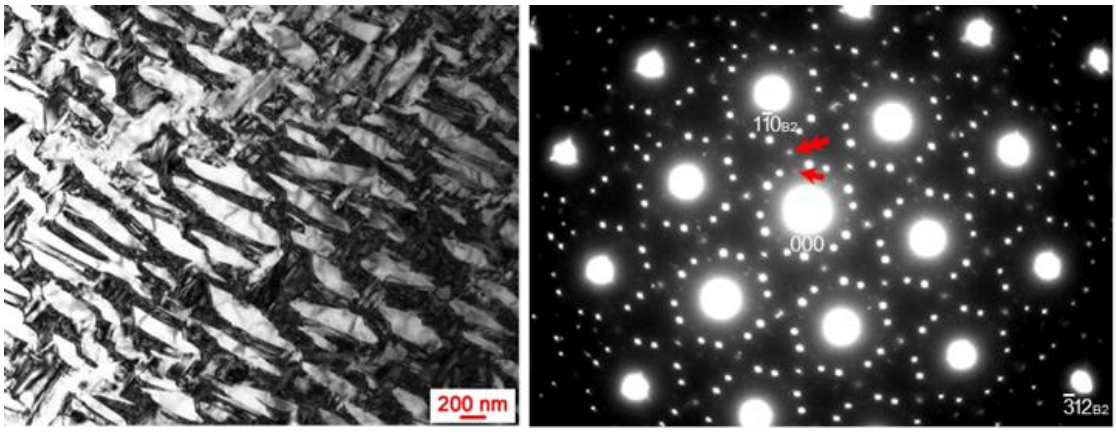


**Figure 4.7 a)** TEM bright field micrograph formations and **b)** selected area diffraction (SAD) pattern for [111]B2 zone axis of $Ni_{54}Ti_{46}$ 550°C-3hr-FC alloy.

## 4.5 Hardness Results

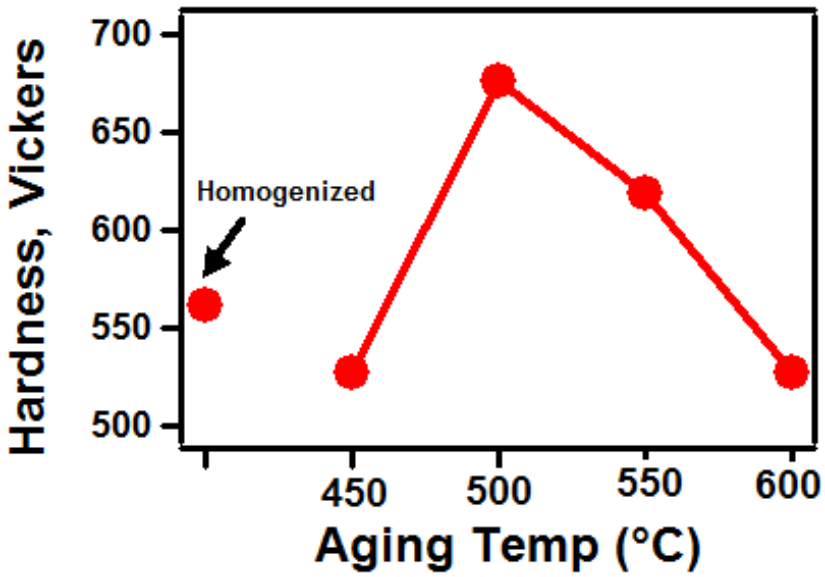


**Figure 4.8** The Vickers hardness of $Ni_{54}Ti_{46}$ as a function of aging temperature.

The hardness values of $Ni_{54}Ti_{46}$ alloy are shown as a function of aging temperature in Figure 4.8. In general, hardness is related to the material strength and formation of precipitates are responsible for the change in strength [107]. It should be noted that fine and homogeneously distributed $Ni_4Ti_3$ precipitates are observed in the homogenized specimen (Chapter 4.4). Vickers hardness value is 562 for homogenized sample. Increasing the aging temperature from 450 °C to 500 °C increases the hardness from 527 to 675 on the Vickers scale due to the formation of $Ni_4Ti_3$ precipitates. Furthermore, increasing aging temperature 550 °C decreases the hardness to 619 which can be attributed to a decrease is the volume fraction of precipitates. After 500 °C-3h aging, the density of precipitate is the highest.

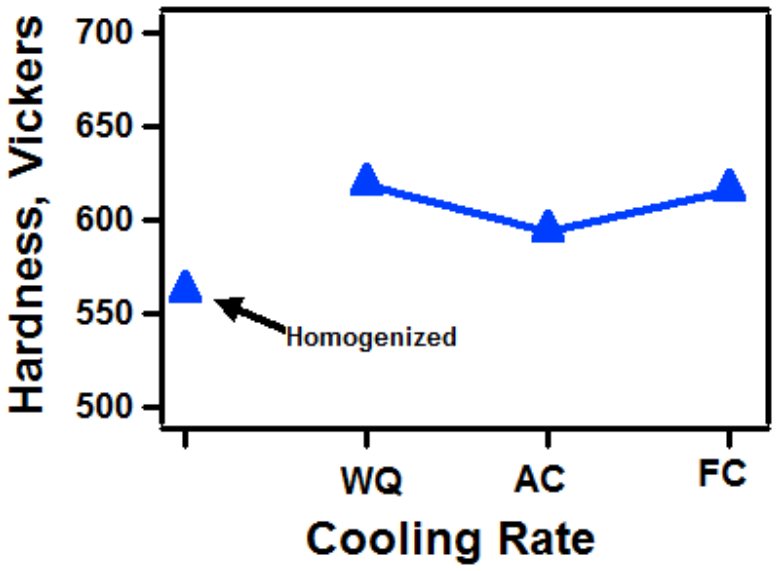


**Figure 4.9** Hardness vs cooling rate values at fixed temperature of 550°C at 3 hours for the $Ni_{54}Ti_{46}$ alloy.

The average hardness values of $Ni_{54}Ti_{46}$ alloy are shown as a function of cooling rate in Fig.4.9. Cooling rate also affects the hardness and strength of the material. The average hardness values are 619, 594 and 615 on the Vickers scale for WQ, AC and FC samples, respectively.

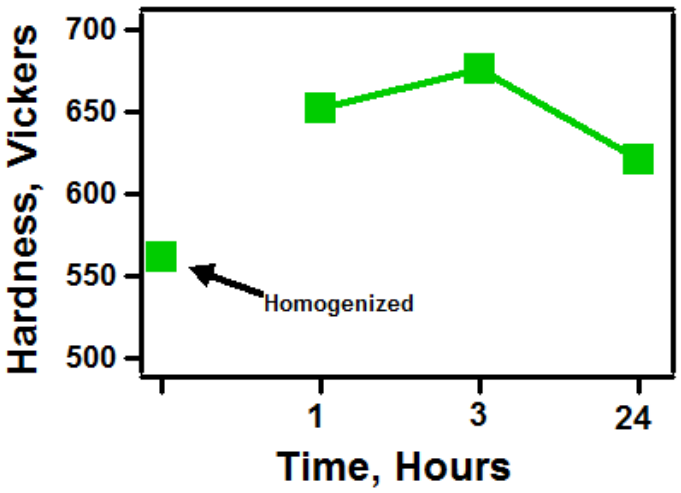


**Figure 4.10** The hardness as a function of aging time of 500°C aged $Ni_{54}Ti_{46}$ alloys.

The hardness values of the aged $Ni_{54}Ti_{46}$ alloy are shown as a function of aging time in Figure 4.10. The maximum hardness value of 675 is observed at aging for 3 hours.

## 4.6 Mechanical Characterization

### 4.6.1 Thermal Cycling Under Constant External Stress

Figure 4.11 (a-d) shows the thermal cycling under stress curves of homogenized and aged $Ni_{54}Ti_{46}$ alloys. The samples were loaded in austenite at a temperature above $A_f$ and cooled below $M_f$ and then, heated above $A_f$. Stress was kept constant during the each cycling test. The applied stress was increased incrementally either until 1800 MPa or until significant plastic strain was observed.

Figure 4.11a shows the methods used to determine the transformation strain, TTs, and temperature hysteresis. The transformation temperatures were determined by the tangent line method. The TTs increased with stress in all cases. For 450°C-3h aging, $M_s^\sigma$ (martensite (B19') start temperature under stress) and $A_s^\sigma$ (austenite start temperature under stress) were 14°C and -5°C under 800 MPa while they were increased to 86 °C and 30°C under 1500 MPa, respectively. $M_s^\sigma$ and $A_s^\sigma$ temperatures after 500°C -3h aging were -34°C and -1°C under 200 MPa and 81°C and 22°C under 1500 MPa, respectively. In the 550°C-3h aged alloy, $M_s^\sigma$ and $A_s^\sigma$ were -41°C and -46°C under 200 MPa while they were 48°C and -17°C under 1500 MPa, respectively. The $M_s^\sigma$ and $A_s^\sigma$ were -72°C and -113°C under 200 MPa and 28°C and 39°C under 1500 MPa, respectively, for the 600°C-3h aged alloy.

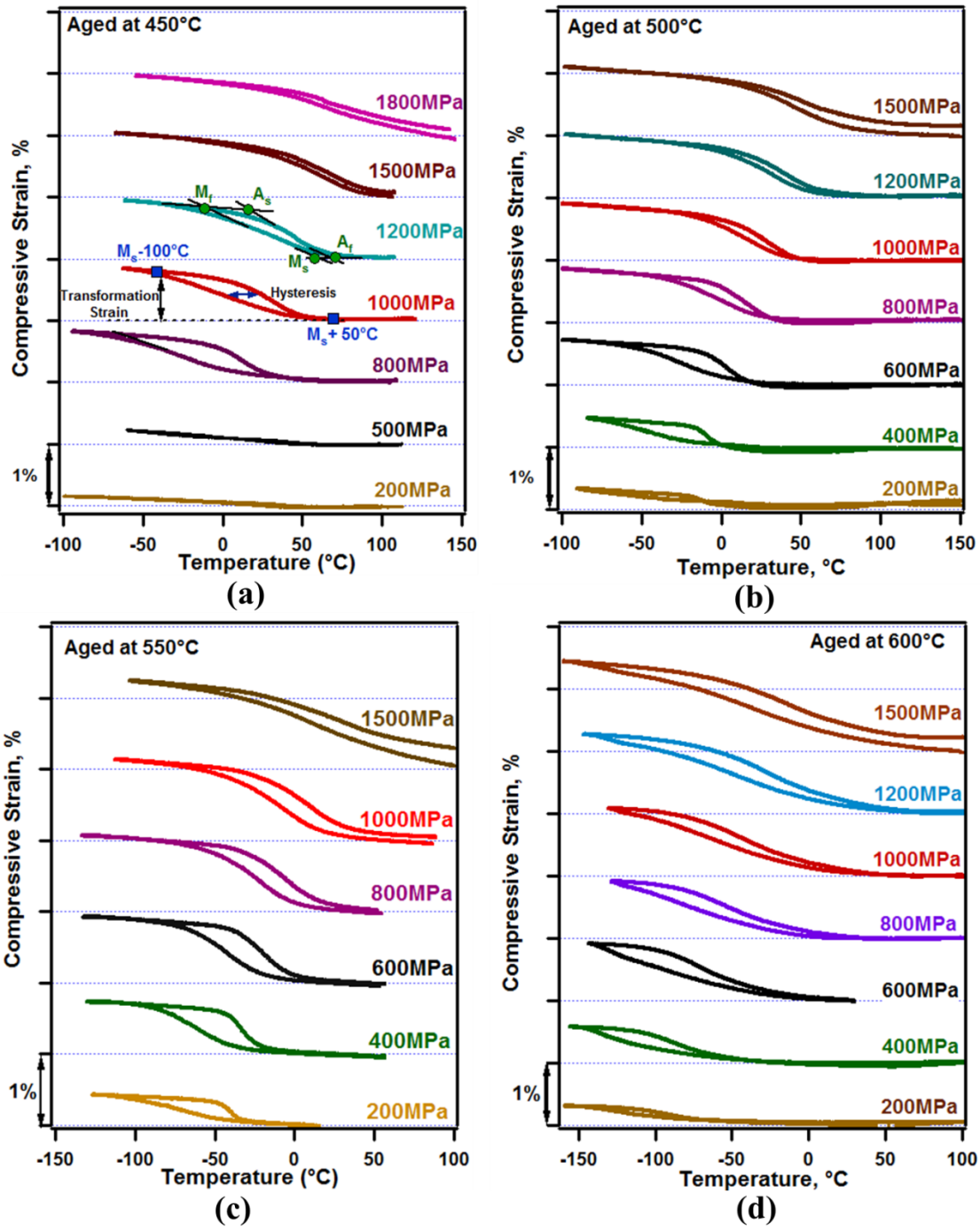


**Figure 4.11** Thermal cycling under compressive stress results of homogenized and aged $Ni_{54}Ti_{46}$ alloys.

Figure 4.11 also shows that the transformation strain was increased with stress. While transformation strain was 0.86% under 800 MPa, it was 0.92% under 1500 MPa for 450°C-3h aged alloy. After 500°C-3h aging, transformation strain was 0.26% under 200 MPa and it increased to 0.9% under 1200 MPa. The transformation strains were 0.43% and 1.09% under 200 MPa and 1200 MPa, respectively, for the 550°C-3h aged case. In the 600°C-3h aged condition, the transformation strains were 0.26% and 1.16% under 200 MPa and 1500 MPa, respectively.

The temperature hysteresis which is measured graphically at the midpoint of the transformation strain was shown with the horizontal arrow in Figure 4.11a. The temperature hysteresis after 450°C-3h aging was found to substantially decrease with stress where it was 26°C under 800 MPa and 8°C under 1500 MPa. Temperature hysteresis was 29°C under 200 MPa and 13°C under 1500 MPa for 500°C-3h aging; 25°C under 200 MPa and 18°C under 1000 MPa for 550°C-3h aging; 20°C under 200 MPa and 17°C under 1000 MPa for 600°C-3h aging.

The irrecoverable strain was calculated at $(A_f^{\sigma}+20)$°C by measuring the difference between the strain values of cooling and heating curves. A very small quantity of irrecoverable strains of about 0.07% and 0.13% were observed at 1500 MPa and 1800 MPa, respectively, for 450°C-3h aged sample. Best of my knowledge, this is the highest stress level under which shape memory effect with almost negligible irrecoverable strain has been obtained in NiTi alloys. The irrecoverable strain was 0.14% at 1500 MPa after 500°C-3h aging; 0.08% at 1000 MPa and 0.23% at 1500 MPa after 550°C-3h aging; 0.22% at 1500 MPa after 600°C-3h aging.

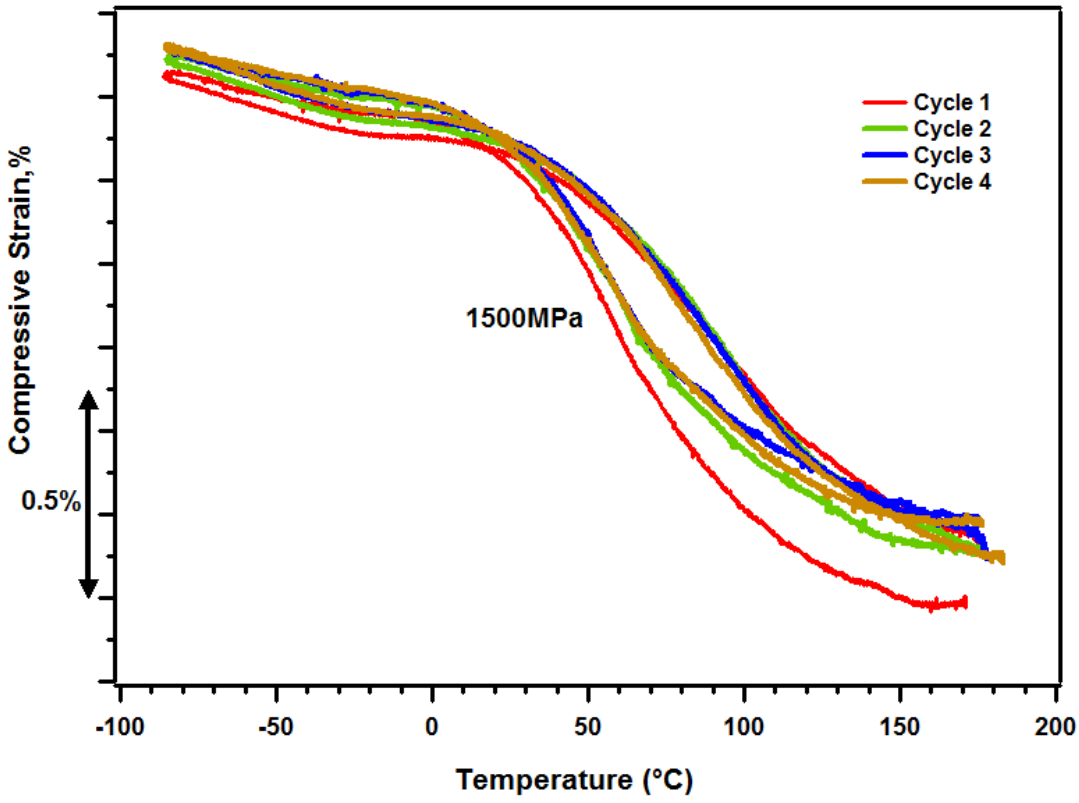


**Figure 4.12** Thermal cycling under 1500 MPa response of the 500°C-3h aged $Ni_{54}Ti_{46}$ sample.

The four thermal cycling under ultra high stress level of 1500 MPa responses of 500°C-3h aged $Ni_{54}Ti_{46}$ are shown in Figure 4.12. After the first cycle, the irrecoverable strain of the sample was 0.14% and it decreased with further cycling. These results show that the shape memory behavior of $Ni_{54}Ti_{46}$ alloy under ultra high stress level of 1500 MPa can be stabilized with training in compression.

### 4.6.2 Isothermal Stress Strain Behavior

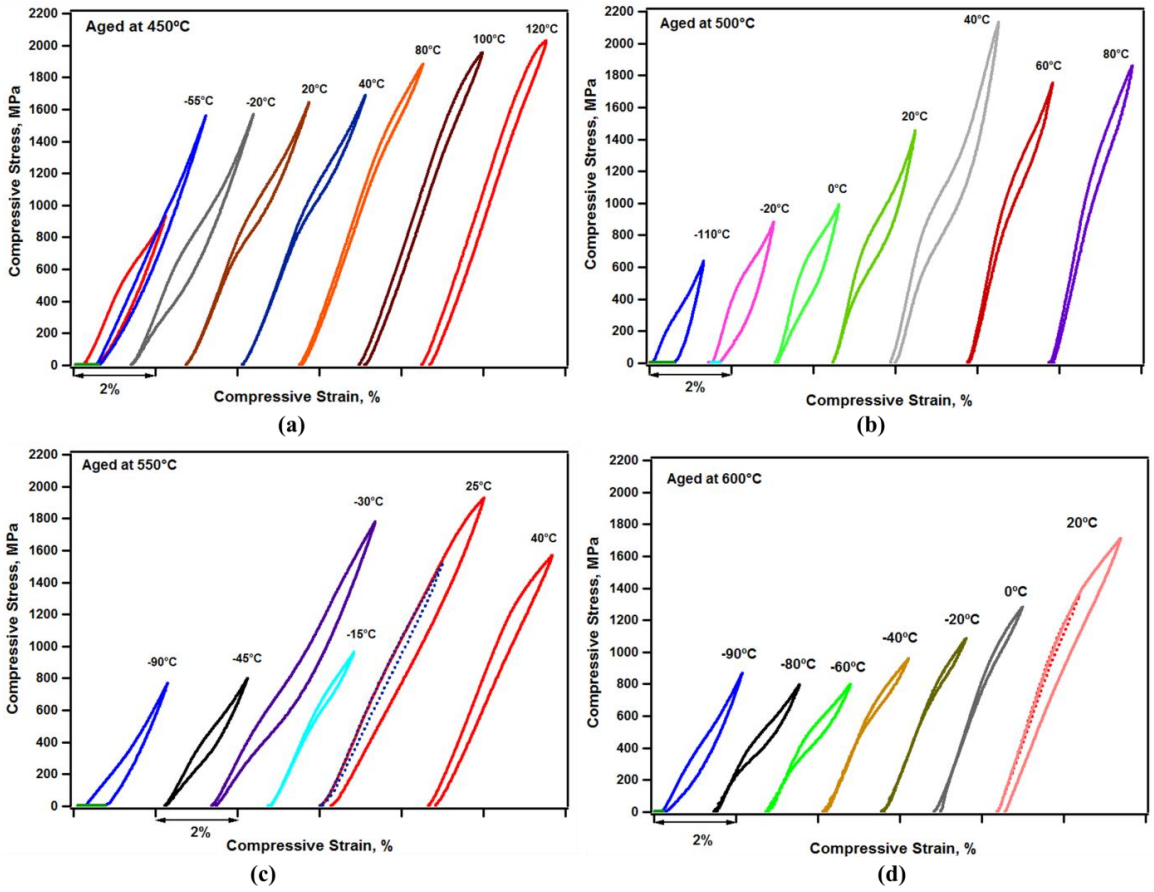


**Figure 4.13** The compressive stress-strain response of $Ni_{54}Ti_{46}$ aged samples as a function of temperature.

Figure 4.13 shows the compressive stress-strain responses of aged $Ni_{54}Ti_{46}$ samples. In some cases, the testing temperature was lower than $A_f$, thus retained strain was observed after unloading. However, upon subsequent heating above $A_f$, the retained strain was recovered by transforming into austenite. In all conditions, superelastic behavior was observed above $A_f$. The alloys started to show superelasticity at different temperatures depending on their aging temperature. The fully recoverable superelasticity starts at -20°C, 0°C, -45°C, and -80°C for the 450°C-3h , 500°C-3h, 550°C-3h and 600°C-3h aged samples, respectively. The total strain of 3%, 2.5%, 4%, and 3% was

observed for the 450°C-3h, 500°C-3h, 550°C-3h and 600°C-3h aged samples, respectively. After 550°C-3h aging, the sample showed perfect superelasticity when it was loaded till 1900 MPa and a strain of 4% at room temperature. Except the 600°C-3h aged condition, all aged samples showed superelasticity around body temperature which makes them promising for biomedical applications [108]. The aged $Ni_{54}Ti_{46}$ alloys have very high strength without any extensive thermomechanical treatments such as rolling or extrusion [109]. The superelasticity was observed with a recoverable strain of 2.5% under an ultra-high stress level of 2100 MPa without any training for the 500°C-3h aged sample. A huge superelastic window of 140°C was observed for 450°C-3h aged sample. The superelastic window was around 80°C for the other aging conditions. It should also be noted that, huge hardening was observed for all aged samples.

### 4.6.3 Discussion

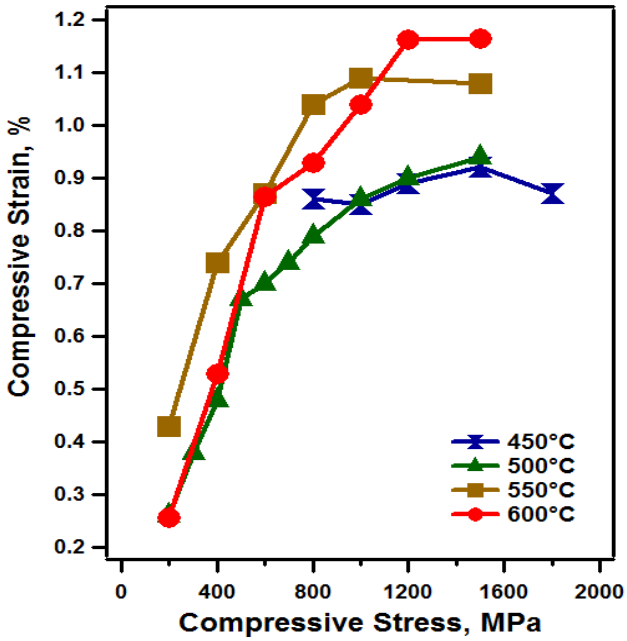


**Figure 4.14** Transformation strain as a function of applied stress.

The transformation strains of aged samples are shown as a function of stress in Figure 4.14. Initially, the transformation strains increase with stress due to the increased volume of favored martensite variants and then saturates. In the 450°C-3h aged sample, the increase in transformation strain was not observed since the shape memory effect curves were incomplete due to very low transformation temperatures. In the 500°C-3h aged condition, the transformation strain increases with stress up to 1500 MPa. In the 550°C-3h aged condition, the transformation strain initially increases with stress up to 1000 MPa and then saturates. The transformation strain initially increases with stress up to 1200 MPa, and then saturates for the 600°C-3h aged sample. The maximum transformation strain of 1.16% was obtained under 1200 MPa in the 600°C-3h aged condition. According to the TEM results, the density of precipitates is higher in the 500°C -3h aged condition compared to 550°C-3h aged sample. Due to the high density of precipitates, the distance between the particles might not be enough to for transformation or stress fields around the particles disrupt the selection of favored variants [110]. According to Hamilton et al., in addition to external stress, the stress field around precipitates induces the preferentially oriented martensite variants [111]. Consequently, less transformation was observed in 500°C-3h aged condition.

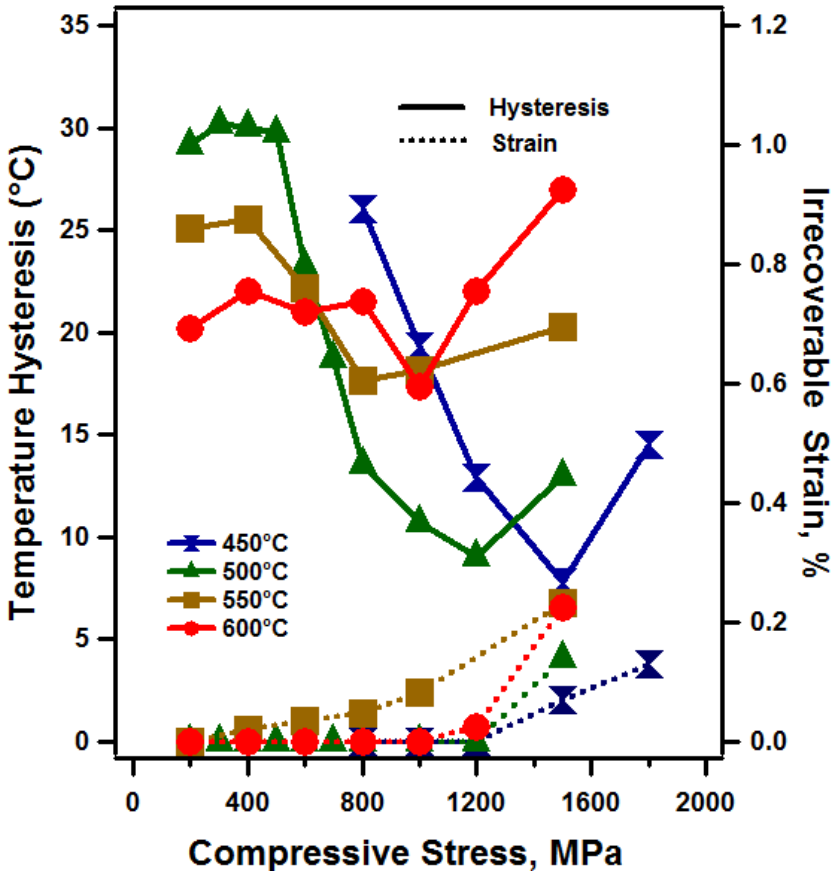


**Figure 4.15** Temperature hysteresis and irrecoverable strain as a function of applied stress.

Figure 4.15 shows the thermal hysteresis and irrecoverable strain responses of $Ni_{54}Ti_{46}$ alloys. In all aging conditions, temperature hysteresis was almost constant at low stress levels. However, it should be noted that triangular type behavior is observed at low stress levels. Then, temperature hysteresis decreased with increasing stress level. The volume fraction of favored martensite variants increased with increasing external stress which can be attributed to the decreased frictional resistance to interfacial motion [111]. At high stress levels, hysteresis increased with the formation of plastic strain, in all conditions. At low stress levels, 500°C-3h aged sample showed the highest thermal hysteresis of 30°C. At high stress levels, it showed temperature hysteresis of 9°C which

is lower than temperature hysteresis for 550°C-3h and 600°C-3h aged samples. The minimum temperature hysteresis is 17°C for 550°C-3h and 600°C-3h aged samples. A very narrow temperature hysteresis of 8°C is observed under 1500 MPa for 450°C-3h aged sample which is the lowest temperature hysteresis for all aging conditions. It was shown by Melton et al. that a temperature hysteresis was ~50°C under 185 MPa for equiatomic NiTi SMA [112].

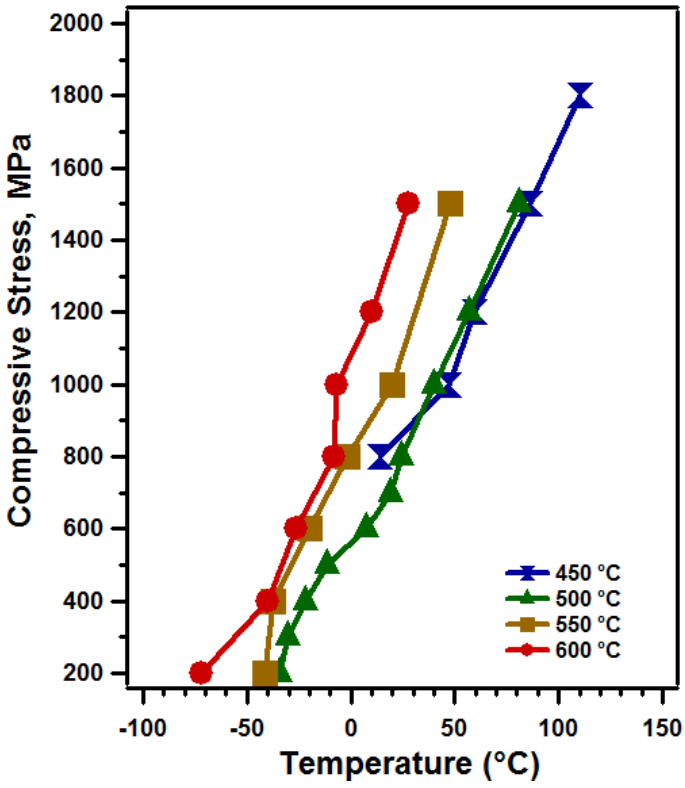


**Figure 4.16** Stress vs. temperature diagram of aged $Ni_{54}Ti_{46}$ alloys.

Figure 4.16 shows the $M_s^\sigma$ of aged $Ni_{54}Ti_{46}$ alloys as a function of applied stress. TTs can be tailored by adjusting the aging temperature in Ni-rich NiTi alloys since they are highly composition dependent [59, 60]. In Figure 4.16, higher aging temperature

leads to lower transformation temperature due to the increased volume fraction of precipitates that decreases the Ni content of the matrix.

The TTs show a linearly increasing trend with stress and the slope of this tendency can be represented by the Clausius-Clapeyron (Cs-Cl) relationship. The relationship can be written as follow,

$$\frac{d\sigma}{dT} = -\frac{\Delta H}{\varepsilon_0 T_0}$$

where $\varepsilon_0$ is the transformation strain in the direction of the uniaxial stress, $\Delta H$ is the transformation enthalpy, $T_0$ is the equilibrium temperature of transformation and $\sigma$ is the uniaxial stress. The Cs-Cl slopes were 10.7, 10.6, 13.2, and 13.7 MPa/°C for the 450°C-3h, 500°C-3h, 550°C-3h and 600°C-3h aged samples, respectively. The Cs-Cl slopes for near equiatomic NiTi varies between 5-8 MPa/°C [113].

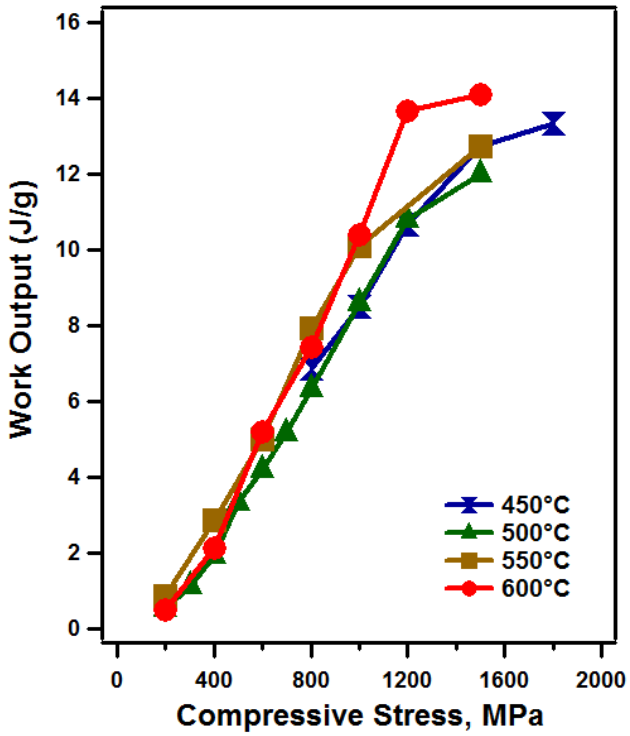


**Figure 4.17** Work output values as a function of applied stress.

Binary NiTi alloys can produce work outputs of 10 - 20 $Jg^{-1}$ [114]. In Figure 4.17, the work outputs increase with applied stresses due to the increased transformation strains. At high stress levels, the work outputs saturate since the transformation strains saturate. For the $Ni_{54}Ti_{46}$ alloy, the maximum measured work output is 13.3 $Jg^{-1}$ after 450°C -3h aging, 12 $Jg^{-1}$ after 500°C -3h aging, 12.72 $Jg^{-1}$ after 550°C -3h aging and 14.1 $Jg^{-1}$ after 600°C -3h aging.

## 4.7 Shape Memory Behavior of aged 550 °C-3h-FC $Ni_{54}Ti_{46}$ SMA

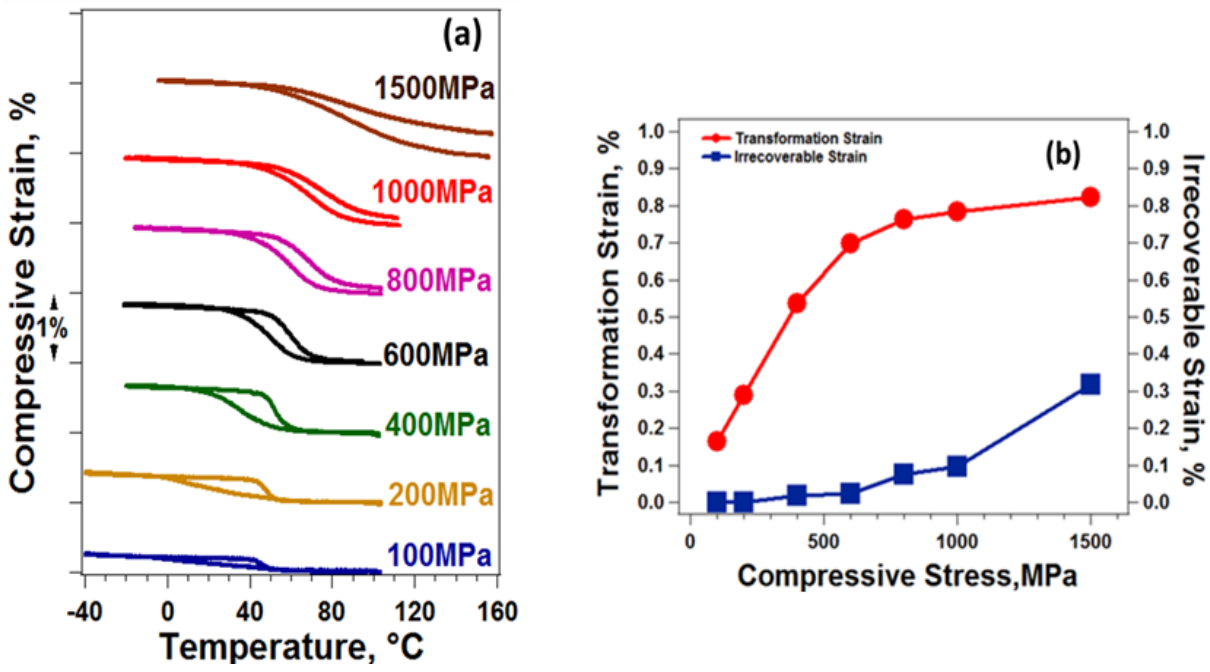


**Figure 4.18 (a)** Thermal cycling in compression test results for 550°C-3hr-FC sample, **(b)** transformation and irrecoverable strains as a function of applied stress.

Figure 4.18 shows the thermal cycling in compression responses of 550°C-3hr-FC sample. The $Ni_{54}Ti_{46}$ ingots were contained in Argon filled quartz ampoules and homogenized at 1000℃ for 4 hours and quenched in water. Following homogenization,

they were aged at 550°C for 3 hours to generate precipitates. Aged SMAs were cooled down by furnace cooling (FC) with a rate of 2 °C/min. The sample with the aforementioned treatment will be referred to as 550°C-3hr-FC in the text from hereafter. The specimen was loaded to selected compressive stress values in austenite, cooled down below the martensite finish temperature ($M_f^\sigma$, martensite (B19') finish temperature under stress) and then heated above the austenite finish temperature ($A_f^\sigma$, austenite finish temperature under stress) to complete one heating/cooling cycle. Applied stress was held constant during each cycle. Multiple thermal cycling tests were performed at compressive stress levels ranging from 100 MPa to 1500 MPa. It is clear from Figure 4.18 that the recoverable strain increases with stress. While transformation strain remained at 0.29% under 200MPa, it increased to 0.78% under 1000 MPa. The TTs increase with stress, as well. $M_s^\sigma$ (martensite (B19') start temperature under stress) and $A_f^\sigma$ were 51 °C and 58 °C under 400 MPa while they increased to 89 °C and 94 °C under 1000 MPa, respectively. The temperature hysteresis was determined graphically as the difference in temperature between the cooling and heating curves corresponding at the midpoint of the transformation strain. The temperature hysteresis was found to substantially decrease with stress and it was 22 °C under 200 MPa and 9 °C under 1000 MPa. Under ultra high compressive stress level of 1500 MPa, the temperature hysteresis increases 28 °C due to the plastic deformation that manifests itself as irrecoverable strain. The irrecoverable strain was calculated at ($A_f^\sigma$+20)°C by taking the difference between the strain values of cooling and heating curves. The irrecoverable strain of the sample is 0.32% at 1500 MPa. Moreover, increasing the applied stress from 1000 MPa to 1500 MPa elevated the irrecoverable strain from 0.09% to 0.32%.

It should be noted that $M_s^\sigma$ and $A_s^\sigma$ (austenite start temperature under stress) were 37 °C and 43 °C ($A_s^\sigma > M_s^\sigma$) under 200 MPa, respectively, while they were 73 °C and 54 °C ($M_s^\sigma > A_s^\sigma$) under 800 MPa. $A_s$ is governed by the accumulated elastic, dissipation and chemical energies where it can be below $M_s$ if the elastic energy storage is very high [115]. Increased external stress yields more elastic energy storage due to the increasing transformation strain. The elastic strain energy accumulated during the forward transformation helps the back transformation from martensite to austenite. Two thermoelastic martensitic transformation categories have been reported by Dunne and Wayman : Class I, where the difference in $M_s$ and $M_f$ is small and $A_s > M_s$, and Class II, in which the difference between $M_s$ and $M_f$ is large and $M_s > A_s$ [116]. As applied stress increases, the level of elastic energy stored gets higher and since the material is strong, it has not been released and thus less heating is sufficient to start backward transformation. Therefore, as applied stress increases the transformation type changes from Class I to Class II.

Figure 4.19 shows the compression test results of 550°C-3hr-FC material. The test specimen was loaded and unloaded at -20 °C (below $A_s$) where upon unloading could not fully recover the applied strain. Subsequent to heating it up to a temperature at the vicinity of $A_f$, it recovered the retained strain which can be deemed as good shape memory behavior. When the sample was loaded and unloaded at a temperature above $A_f$, superelastic behavior was observed with large recoverable strain.

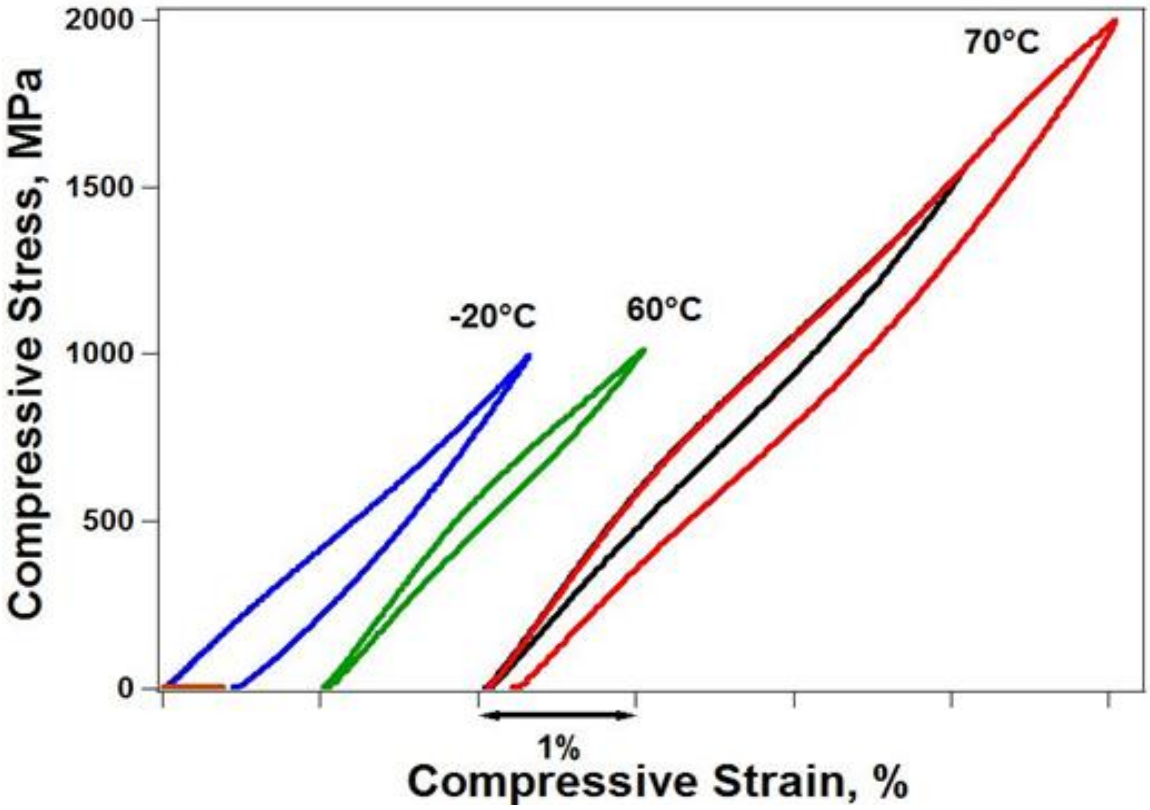


**Figure 4.19** The compressive stress vs. strain (superelasticity) responses of $Ni_{54}Ti_{46}$ for 550°C-3hr-FC sample.

The alloy started demonstrating fully recoverable superelasticity at 60 °C (i.e., $A_f$+3$^o$C), while it had only 0.17% irrecoverable strain upon loading to 4% reaching a load level of 2000 MPa at 70 °C (i.e., $A_f$+13$^o$C). Figure 4.19 demonstrates that aged $Ni_{54}Ti_{46}$ alloys are capable of very high strength without the need of extensive thermomechanical treatments. In literature, it was reported that $Ni_{50.8}Ti_{49.2}$ (at. %) polycrystals have transformation strain of 2.7% and 2.6% after heat treatments at 500 $^o$C for 15 hours and at 400 $^o$C for 1.5 hours, respectively [117]. Figure 4.19 showed that the test temperature drastically affects the critical stress for backward (martensite to austenite) transformation. When the sample is loaded at a higher temperature, a higher critical stress is obtained.

While the critical stress was 565 MPa at 60 °C, it was 669 MPa for a test temperature of 70 °C. The slope of the transformation plateau increases with increasing test temperature accompanied with a significant strain hardening effect.

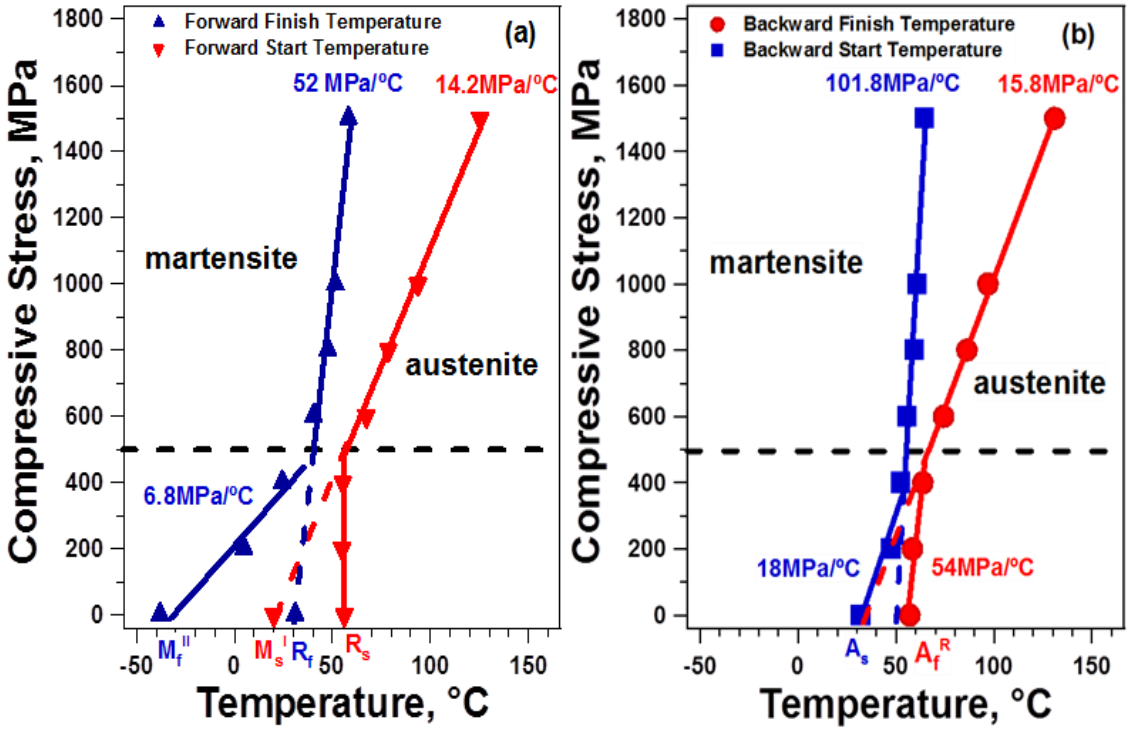


**Figure 4.20** Stress vs. temperature phase diagram of 550°C-3hr-FC aged $Ni_{54}Ti_{46}$ alloys for **a)** Forward (austenite to martensite) and **b)** Backward (martensite to austenite) transformations.

Figure 4.20 shows the phase diagrams of 550°C-3hr-FC specimen that were constructed by the TTs extracted from thermal cycling test results shown in Figure 4.18. The TTs which are determined from DSC tests in stress free condition (Figure 4.2), are also added to Figure 4.20. The TTs show a linearly increasing trend with stress and the slope of this tendency can be represented by the Classius-Clapeyron (Cs-Cl) relationship. It is clear that the change in TTs above 500 MPa is different than the change in TTs below 500 MPa. During forward transformation, two forward-finish-temperature (FFT)

slopes were obtained as functions of stress. Cs-Cl slope of the FFT is 6.8 MPa/°C below 500 MPa while it is 52 MPa/°C above 500 MPa. Forward-start-temperature (FST) slope was 14.2 MPa/°C above 500 MPa where below 500 MPa it was very high. Figure 4.20b shows the TTs as a function of applied stress during the backward transformation of martensite to austenite. Similar to forward transformation, two-stage behavior is also observed in backward transformation. The backward-start-temperature (BST) slope was 18 and 101.8 MPa/°C below and above the 500MPa, respectively. Backward-finish-temperature (BFT) slope of 54 and 15.8 MPa/°C were obtained below and above 500 MPa, respectively.

As an important observation during thermal cycling, an asymmetric "triangle type" behavior was observed at low stress levels (below 500 MPa) while this behavior was symmetric at higher stress levels (above 500 MPa). The change in thermal cycling responses with stress can be attributed to the i) change in martensite morphology or ii) change in a transformation sequence with stress.

It was shown by Sutou et al. that in Cu-based SMAs, stress induced martensitic transformation requires additional energy compared to thermally induced stress transformation after aging [118]. Thus, the TTs obtained from thermal cycling under no stress (e.g. DSC curves) do not match to the TTs obtained by extrapolation of Cs-Cl slope. A similar phenomenon might be taking place in Ni rich NiTi alloys where due the presence of high volume fraction of particles and R-phase formation, stress induced martensite morphology below 500MPa would be different than the stress induced martensite morphology above 500 MPa. Thus, two different Cs-Cl slopes below or above 500MPa could be observed.

The change in thermal cycling response with stress might also be attributed to the change in transformation sequence and inhomogeneous distribution of precipitates. It is clear that when the FST line above 500 MPa is extended, it coincides with $M_s^I$ (Figure 4.20a) while the extrapolated FFT line above 500 MPa matches with $R_f$. Extended FST line below 500 MPa coincides with $R_s$ while extrapolated FFT line below 500 MPa matches with $M_f^{II}$ (Figure 4.20a). It is well known that austenite to R-phase TTs are weakly dependent on applied stress (high Cs-Cl slope) while austenite to B19' TTs are highly stress dependent (low Cs-Cl slope) [119-121].

In general, during cooling after aging, austenite to R phase transformation is initiated near precipitates followed by R to B19' (martensite) transformation [104]. In some cases, the inhomogeneous distribution of $Ni_4Ti_3$ precipitates in Ni-rich NiTi results in complex multi-stage martensitic transformations [103]. It should be kept in mind that the alloys studied are highly Ni-rich which also results in inhomogeneous distribution of precipitates. Thus, the interparticle distance might be small in certain regions while being larger at other regions in the microstructure. When this distance between particles is very small, the parent phase could be locked by internal stress, and transformation start can be impeded [122]. This fact is related to what has been observed that in Ni-rich $Ni_{50.3}Ti_{49.7}$ alloys where martensitic transformation is suppressed with a decrease in grain size and especially below a critical grain size only B2 to R-phase transformation is possible [123]. If grain size is decreased further, no transformation is observed. The aged highly Ni-rich $Ni_{54}Ti_{46}$ sample has a heterogeneous microstructure with varying distribution of particle size and interparticle distances, certain regions of the sample might only transform to R-phase, while other regions could transform to B19' martensite. Since R-phase

temperatures are almost stress independent, stable FFT was observed in the regions with very small interparticle distances, resulting in the change of thermal cycling under stress behavior when high stress is applied.

It can be argued from the phase diagram (Figure 4.20) that at low stress levels (< 500 MPa) during cooling, $M_s^\sigma$ is lower than $R_s^\sigma$ (R phase start temperature under stress) and thus austenite starts transforming to R-phase initially and then B19' martensite where the FFT is governed by $M_f^\sigma$ which is lower than $R_f^\sigma$ (R phase finish temperature under stress ). At high stress levels, since the $R_s^\sigma$ and $R_f^\sigma$ are almost independent of stress while austenite to martensite transformation temperatures are highly stress dependent, $M_s{}^\sigma$ increases above $R_s^\sigma$ and $M_f^\sigma$ increases above $R_f^\sigma$. Thus, B2 to B19' transformation starts initially and in certain regions with narrow interparticle distance B2 to R phase transformation occurs where the FFT is governed by $R_f^\sigma$ which is lower than $M_f^\sigma$ for B2-B19' transformation. Thus, although the start temperature for forward transformation is increasing, the finish temperature for forward transformation is almost constant.

## 4.8 Conclusions

Shape memory behavior of highly Ni-rich $Ni_{54}Ti_{46}$ alloys was studied. This chapter also was performed to reveal the effects of aging on the microstructure and shape memory properties of $Ni_{54}Ti_{46}$ Ni-rich SMA. $Ni_4Ti_3$ precipitates were observed in both homogenized and aged specimens. While fine $Ni_4Ti_3$ precipitates with ~10-30 nm in size are homogeneously distributed in the homogenized specimen, the $Ni_4Ti_3$ precipitates grew after aging at 550°C and high density of lenticular precipitates were observed on $\{111\}_{B2}$ planes. The volume fractions of the $Ni_4Ti_3$ precipitates were about 55% after 500°C-3h aging and 43% after 550°C aging. TTs are tailored by changing aging. Both the

decrease in cooling rate and increasing the aging time leads to increase of $M_s$ temperature due to the Ni depletion of matrix with $Ni_4Ti_3$ precipitate formation. $M_s$ temperatures were -61°C and 20°C for 550°C- 3h- WQ and 550°C- 3h- FC aged samples, respectively. Multiple step transformation observed after aging. While the first transformation was B2 to R phase transformation, the second transformation was an R-phase of B19' transformation during cooling. It was found that mechanical and shape memory properties of $Ni_{54}Ti_{46}$ were highly precipitation characteristics and applied stress dependent. The asymmetric "triangle type" behavior for shape memory effect was observed below 500 MPa while the behavior was symmetric at higher stress levels. The shape memory behavior was investigated in compression and it was discovered that they have a low transformation strain (~1%) but very high strength and very narrow temperature hysteresis. The shape memory effect was observed even under an ultra high stress level of 1500 MPa without prior training in all aged samples. The maximum transformation strain of 1.16% is obtained under 1200 MPa in the 600°C -3h aged condition. A very narrow temperature hysteresis of 8°C is observed under 1500 MPa for 450°C -3h aged sample. The maximum work output is 14.1 $Jg^{-1}$ after 600°C -3h aging. At room temperature, the superelastic behavior was observed accompanied with a large recoverable strain (4%) in 550°C -3h aged condition. This ultra-high strength Ni-rich NiTi SMAs are promising for medical applications due to their distinct superelasticity and shape memory properties coupled with its biocompatibility. A narrow hysteresis and high stability of the shape memory effect also makes this alloy attractive for actuator applications.

# 5 Effects of orientation on the shape memory behavior of $Ni_{51}Ti_{49}$ single crystals

## 5.1 Introduction

Anisotropic properties of SMAs are very essential to demonstrate the shape memory and superelastic strains which can be optimized along a certain direction for sensor and actuator applications [20]. It is well known that stress-induced martensitic transformation is strongly temperature and crystal orientation dependent [16-19]. Moreover, utilizing single crystals could eliminate the grain boundary effects thus allowing for an uncomplicated investigation of precipitate effects.

In this study, the shape memory behavior of $Ni_{51}Ti_{49}$ alloys along the [001], [011] and [111] crystallographic orientations were studied systematically. The thermal cycling under compressive stress and superelastic responses have been examined for all orientations. The transformation strains, irrecoverable strains and temperature hysteresis are determined.

The $Ni_{51}Ti_{49}$ single-crystals were grown by Bridgman Technique in an inert gas. The as received $Ni_{51}Ti_{49}$ single-crystals were contained in Argon filled quartz ampoules and homogenized at 1000℃ for 2 hours and quenched in ambient temperature water. Subsequently, homogenized samples were given aged at 500°C for 1.5 hours to form precipitates.

## 5.2 DSC Results

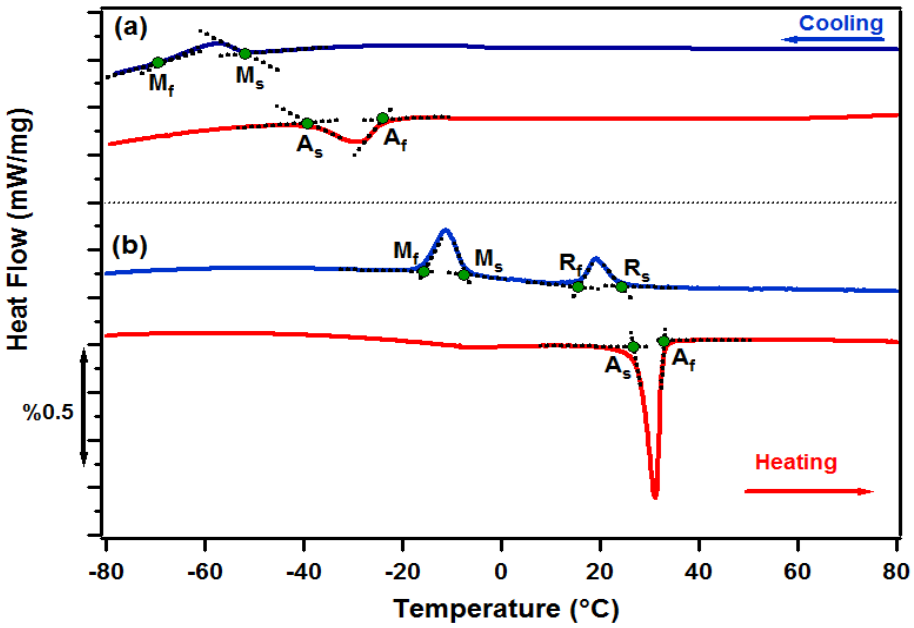


**Figure 5.1** DSC responses of $Ni_{51}Ti_{49}$ single crystals after **a)** solution treatment and **b)** aged at 500°C for 1.5 hours.

Figure 5.1a shows the DSC result of the solution-treated $Ni_{51}Ti_{49}$ single crystal. The peaks can be attributed to the B2 to B19' martensite formation during cooling and vice versa upon heating. The TTs of the solution-treated sample were determined as; $M_s$ = -52 °C, $M_f$ = -68 °C, $A_s$ = -37 °C, $A_f$ = -23 °C. Figure 5.1b shows the DSC result of the aged $Ni_{51}Ti_{49}$ single crystal. During cooling, the first peak (at about 20°C) is attributed to the B2 to R-phase formation while the second peak is attributed to R to B19' martensite formation. Upon heating, B19' martensite to austenite transformation occurred. The TTs were determined as; $R_s$ = 25 °C, $R_f$ = 16 °C, $M_s$ = -7 °C, $M_f$ = -16 °C, $A_s$ = 27 °C, $A_f$ = 33 °C. The TTs were increased after aging which can be attributed to the formation of $Ni_4Ti_3$ precipitates that decreases the Ni concentration of the matrix [5]. Since the TTs of Ni rich

Ni-Ti alloys decrease with increasing the Ni content of matrix, lower Nickel content of the matrix after aged samples resulted in an increase in TTs [103].

## 5.3 Thermal cycling under external stress

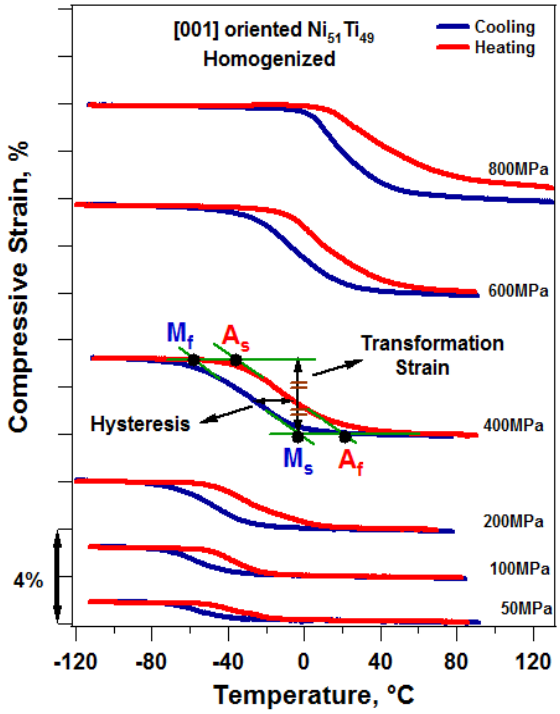


**Figure 5.2** Thermal cycling under constant stress responses of homogenized $Ni_{51}Ti_{49}$ single crystals along the [001] orientation.

The strain-temperature curves generated during thermal cycling under stress are presented in Figure 5.2 for the [001]-oriented homogenized sample. The specimen was compressed to selected stress values in austenite, cooled down below the martensite finish temperature ($M_f$) and then heated above the austenite finish temperature ($A_f$) to complete one thermal cycle. Applied stress was held constant during each cycle. The stress levels were increased incrementally to 50 MPa, 100 MPa, 200 MPa, 400 MPa, 600 MPa and 800 MPa.

Figure 5.2 shows the methods used for determination of transformation strain, TTs and temperature hysteresis. The transformation strain increases with stress. In [001], the transformation strains were found to be 0.66% under 50 MPa and 3.83% under 800 MPa.

The TTs in thermal cycling curves were determined by tangent method. $M_s^\sigma$ (martensite (B19') start temperature under stress) was -40°C under 50 MPa while it increased to 42°C under 800 MPa along the [001] orientation.

The irrecoverable strain was calculated at $A_f^\sigma$+20°C by taking the difference between the strain values of cooling and heating curves. The irrecoverable strain was 0.7% under 800 MPa along the [001] orientation.

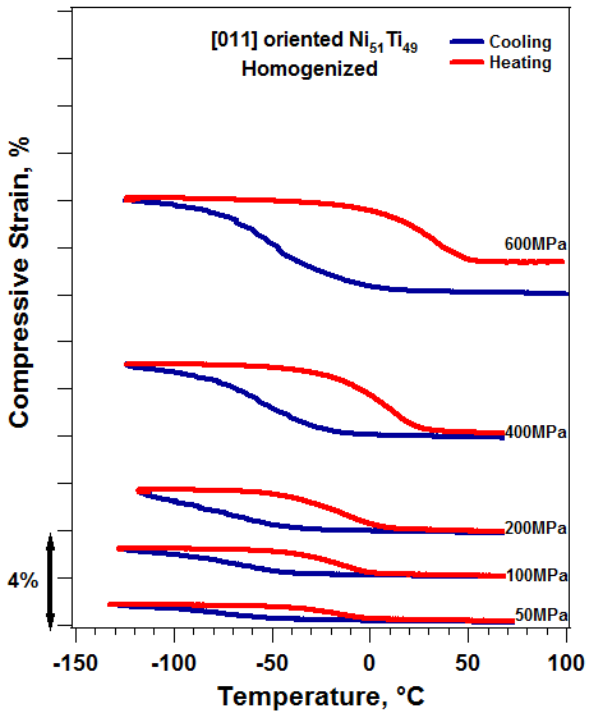


**Figure 5.3** Thermal cycling under constant stress responses of homogenized $Ni_{51}Ti_{49}$ single crystals along the [011] orientation.

The strain-temperature curves generated during thermal cycling under stress are presented in Figure 5.3 for the [011] oriented homogenized sample. The stress levels were increased incrementally to 50 MPa, 100 MPa, 200 MPa, 400 MPa and 600 MPa. In [011], transformation strain was 0.58 % under 50 MPa and increased to 3.72% under 600 MPa and $M_s^{\sigma}$ was -49°C and -4°C under 50 MPa and 600 MPa, respectively. The thermal hysteresis is defined as the width of the strain-temperature loops measured at the midpoint of the transformation strain as shown in Figure 5.2. The temperature hysteresis was found to substantially decrease with stress and it was 59°C under 50 MPa and 54°C under 100 MPa along the [011] orientation. The irrecoverable strain was 1.3% under 600 MPa along the [011] orientation.

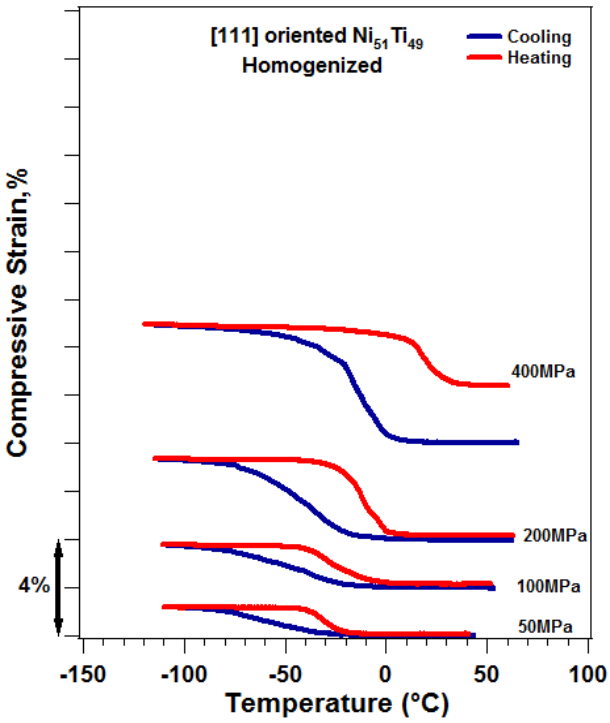


**Figure 5.4** Thermal cycling under constant stress responses of homogenized $Ni_{51}Ti_{49}$ single crystals along the [111] orientation.

The strain-temperature curves generated during thermal cycling under stress are presented in Figure 5.4 for the [111]-oriented of homogenized sample. The stress levels were increased incrementally to 50 MPa, 100 MPa, 200 MPa and 400 MPa. In [111], transformation strain was 1.14 % under 50 MPa and increased to 4.71% under 400 MPa. In [111] orientation, $M_s^{\sigma}$ was -29°C and 2°C under 50 MPa and 400 MPa, respectively. The temperature hysteresis was found to substantially decrease with stress and it was 27°C under 50 MPa and 23°C under 100 MPa along the [111] orientation. The irrecoverable strain was 2.3% under 400 MPa along the [111] orientation.

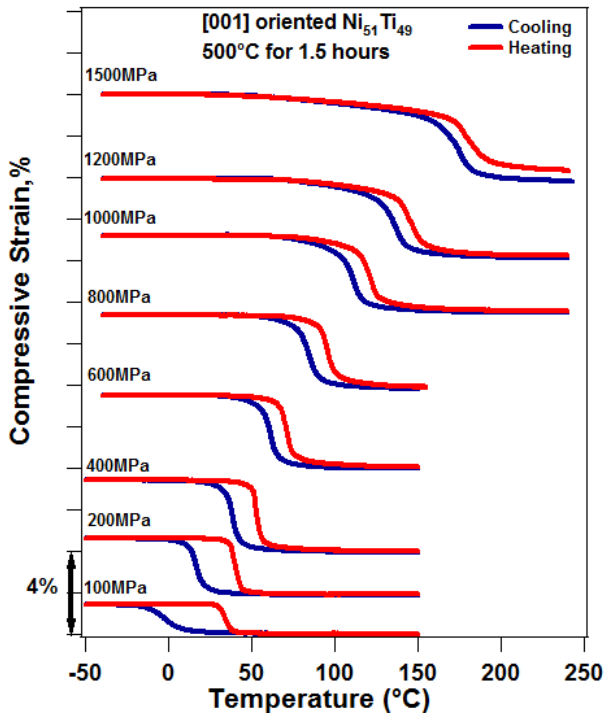


**Figure 5.5** Thermal cycling under constant stress responses of aged $Ni_{51}Ti_{49}$ single-crystals along the [001] orientation.

Figure 5.5 shows the thermal cycling under compressive stress responses of 500°C-1.5 hours aged single crystal along the [001] orientation. At low stress levels (<

300 MPa), two-stage B2-R-B19' transformations are observed during cooling while single step B19'-B2 transformation is observed during heating. At high stress level (>300MPa), one-stage (B2-B19') transformation was observed on cooling. The change in thermal cycling responses with stress can be attributed change in a transformation sequence with stress [124]. At low stress levels (< 300 MPa) during cooling, $M_s^\sigma$ is lower than $R_s^\sigma$ (R-phase start temperature under stress) and thus austenite starts transforming to R-phase initially and then B19' martensite. On the contrary, $M_s^\sigma$ increases above $R_s^\sigma$ at high stress levels since $R_s^\sigma$ is almost independent of stress while $M_s^\sigma$ temperatures are highly stress dependent. Therefore, one-stage B2 to B19' transformation was observed on cooling at high stress levels.

The transformation strains initially increase and then saturate. Transformation strain was 1.37 under 100 MPa and 3.27% under 600 MPa in [001] orientation. It increased to 3.65% under 1500 MPa. The temperature hysteresis was found to substantially decrease with stress where it was 37°C under 100 MPa and 15°C under 400 MPa along the [001] orientation. The temperature hysteresis was 23°C under 200 MPa, 10°C under 1000 MPa and 9°C under ultra high compressive stress level of 1500 MPa. The irrecoverable strain was 0.18% at 600 MPa in [001] orientation. Moreover, increasing the applied stress from 600 MPa to 1500 MPa elevated the irrecoverable strain from 0.18% to 0.62% along the [001] orientation. The TTs increase with stress, as well where $M_s^\sigma$ was 7°C under 100 MPa while it increased to 65°C under 600 MPa along the [001] orientations.

The strain-temperature curves generated during thermal cycling under stress are presented in Figure 5.6 for the [011] oriented aged single crystal. Similar to [001]

orientation, two-stage B2-R-B19' transformations are observed during cooling at low stress levels (< 300 MPa) while one-stage (B2-B19') transformation was observed at high stress levels (>300MPa).

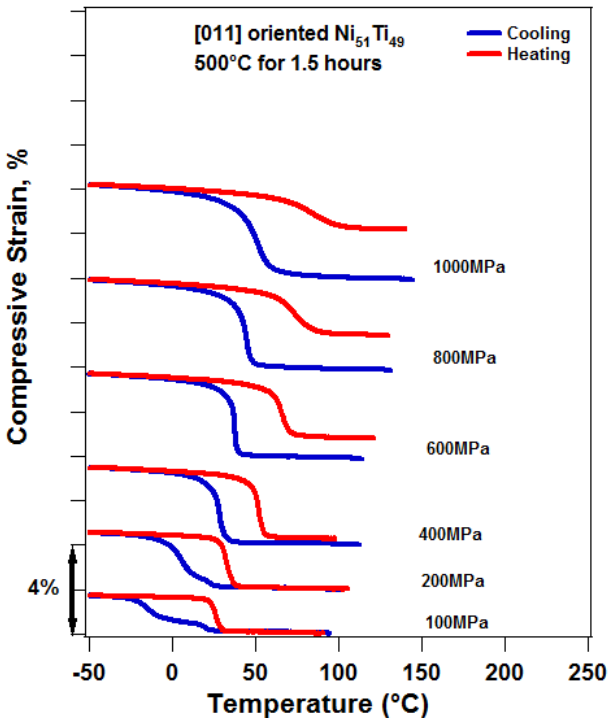


**Figure 5.6** Thermal cycling under constant stress responses of aged $Ni_{51}Ti_{49}$ single-crystals along the [011] orientation.

Transformation strain was 1.5% under 100 MPa and 3.3% under 600 MPa in [011] orientation. It increased to 3.7% under 1000 MPa in [011]. The temperature hysteresis substantially decreased with stress where it was 36°C under 100 MPa and 24°C under 400 MPa. Above 400 MPa, temperature hysteresis increases gradually due to plastic deformation that manifests itself as irrecoverable strain. Temperature hysteresis was 29°C, 39°C and 52°C under 600MPa, 800MPa and 1000MPa, respectively. When the applied stress increases from 400 MPa to 1000 MPa, the irrecoverable strain elevates

from 0.24% to 2.19%. The TTs increase with stress where $M_s^\sigma$ was -7°C under 100 MPa while it increased to 39°C under 600 MPa.

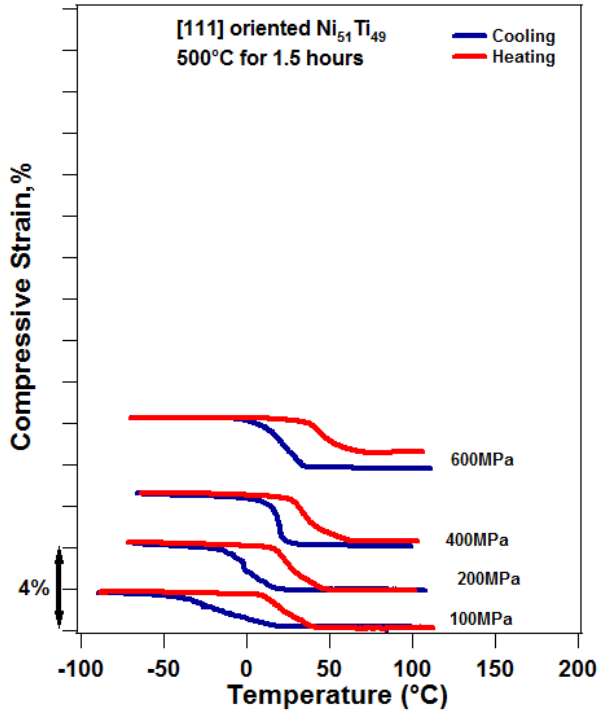


**Figure 5.7** Thermal cycling under constant stress responses of aged $Ni_{51}Ti_{49}$ single-crystals along the [111] orientation.

Figure 5.7 shows the thermal cycling under compressive stress responses of 500°C-1.5h aged single crystal along the [111] orientation. The stress levels were increased incrementally to 50 MPa, 100 MPa, 200 MPa, 400 MPa and 600 MPa. Transformation strain was 1.56% under 100 MPa and 2.28% under 600 MPa. The temperature hysteresis was 39°C under 100 MPa and 19°C under 400 MPa. Above 400 MPa, temperature hysteresis increased gradually due to plastic deformation. The irrecoverable strain was 0.74% at 600 MPa. $M_s^\sigma$ was 18°C under 100 MPa while it increased to 35°C under 600 MPa along the [111] orientations.

## 5.4 Isothermal stress strain behavior

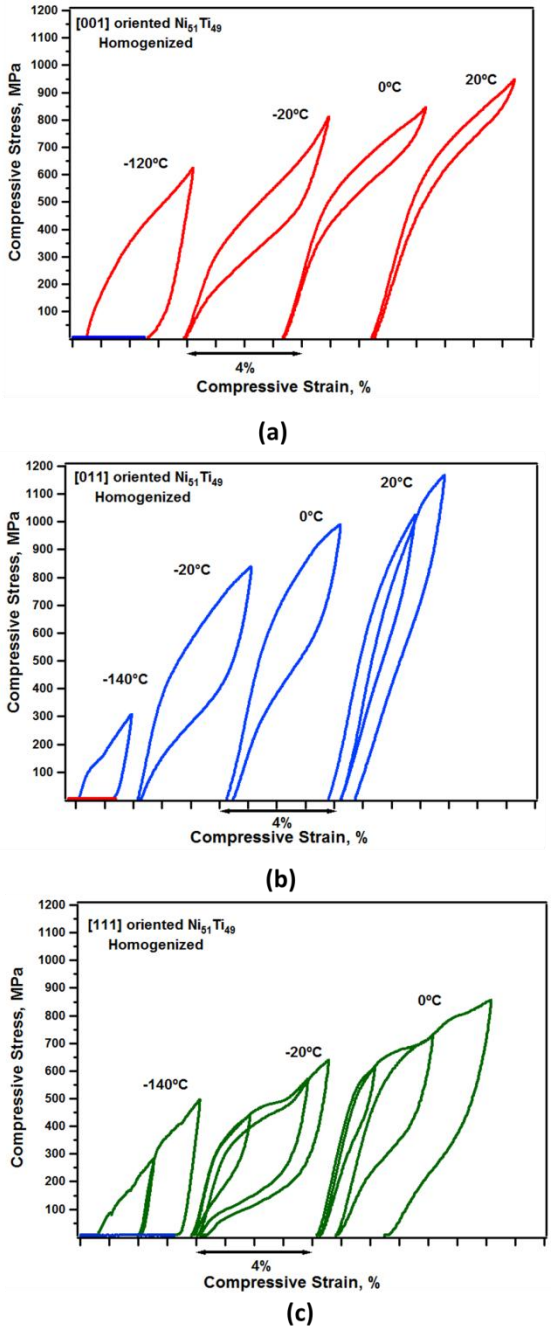


**Figure 5.8** The compressive stress-strain response of homogenized $Ni_{51}Ti_{49}$ single-crystals along the [001], [011], and [111] orientations as a function of temperature.

The compressive stress-strain responses of the homogenized single crystals along the [001], [011], and [111] orientations are shown in Figure 5.8. The samples were deformed at -140°C (below $M_f$) to show variant reorientation behavior and at selected temperatures above $A_f$ to show superelasticity. In all orientations, superelastic behavior was observed with a large recoverable strain (4%). Figure 5.8 shows that temperature drastically affects the critical stress for transformation. When the sample is loaded at a higher temperature, a higher critical stress is obtained.

The compressive stress–strain curves of the aged single crystals along the [001], [011], and [111] orientations obtained at selected temperatures are plotted in Figure 5.9. It should be noted that -80$^o$C was below $M_f$ while 40$^o$C was above $A_f$. At -80$^o$C, martensite reorientation takes place during loading and the remained strain after unloading is recovered upon heating.

The alloy showed fully recoverable superelasticity in [001] orientation while it had 0.2% and 0.3% irrecoverable strain in [011] and [111] orientations, respectively, at 40°C. The superelastic response with a total strain of 7% is obtained at high temperature in [001] orientation. According to compressive stress vs strain curves at 60$^o$C (Figure 5.9b and 5.9c), significant residual strain was observed after unloading the [011] and [111] oriented single crystals. The largest superelastic window of $\Delta T$ = 140°C was observed in [001] orientation.

The stress hysteresis, $\Delta\sigma$, decreases with increasing test temperature along the [001] orientation as shown in Figure 5.9a. $\Delta\sigma$ is 148 MPa at 40$^o$C while it is 89 MPa at 160$^o$C. The similar behavior was also observed by Chumlyakov et al. [125], where the temperature dependence of $\Delta\sigma$ is attributed to the effects of external stresses on the

nucleation and growth of martensite crystals when four crystallographic variants of particles are formed by aging.

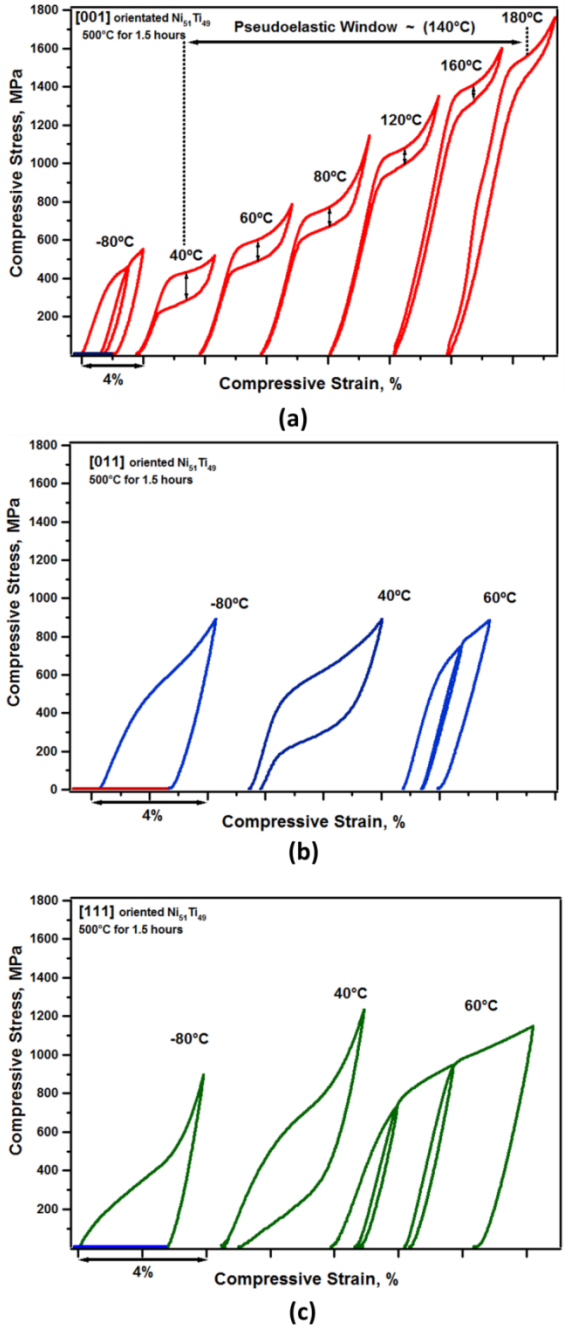


**Figure 5.9** The compressive stress-strain responses of aged $Ni_{51}Ti_{49}$ single-crystals as a function of temperature.

## 5.5 Discussion

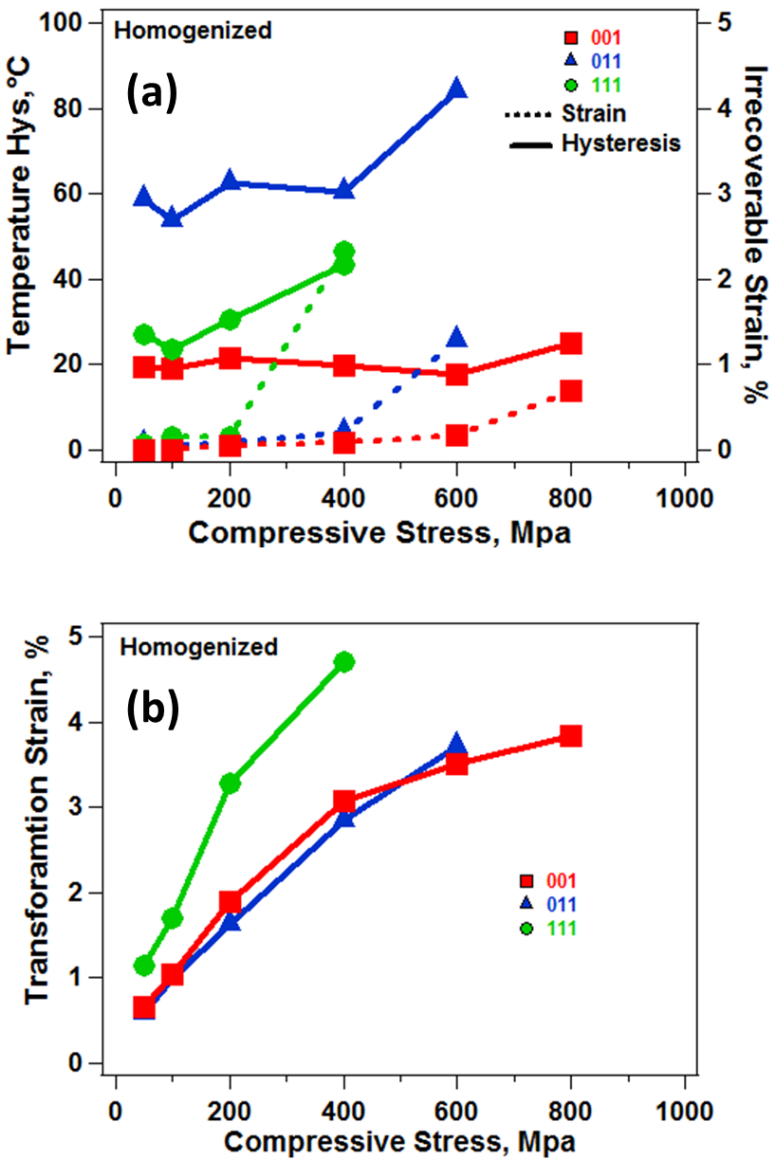


**Figure 5.10 (a)** Temperature hysteresis and irrecoverable strain and **(b)** transformation strain as a function of applied stress for homogenized $Ni_{51}Ti_{49}$ single crystals.

Figure 5.10a shows the thermal hysteresis and irrecoverable strain as a function of applied stress along the three selected orientations of homogenized $Ni_{51}Ti_{49}$. [011]-oriented single crystals showed the highest thermal hysteresis. The hysteresis did not change with external stress for homogenized [001]-oriented $Ni_{51}Ti_{49}$ single-crystal. The similar behavior was reported by Hamilton et al. in $Ni_{50.4}Ti_{49.6}$ [111]. The slip systems of NiTi are reported to be <010>{110} and <010}>{100} [126]. The resolved shear stress for these slip systems is zero in [001] orientation [125]. Therefore, [001]-oriented single crystals show no signs of plastic strain.

The transformation strains of homogenized samples are shown as a function of stress in Figure 5.10b. It is clear that [111] orientation has the highest transformation strain amongst the studied homogenized single crystals. At 200 MPa, [111] orientation produced a noticeably higher transformation strain when compared with each of the other orientations. At 400 MPa, the transformation strain is still highest in [111] orientation but so does its irrecoverable strain. [001]-oriented single crystals show no signs of irrecoverable strain, whereas, [111]-oriented single crystals show noticeable irrecoverable strain. The onset of irrecoverable strain occurred at a lower stress level (approximately at 200MPa) in [111] orientation than the two other oriented samples.

With increasing stress, the transformation strains increase due to increased volume of favored martensite variants. The maximum transformation strain for the [111] orientation is significantly higher than for the [001] and [011] orientations. In [001], the transformation strain was 3.83% under 800 MPa. In [011], transformation strain was 3.72% under 600 MPa. In [111], transformation strain was 4.71% under 400 MPa.

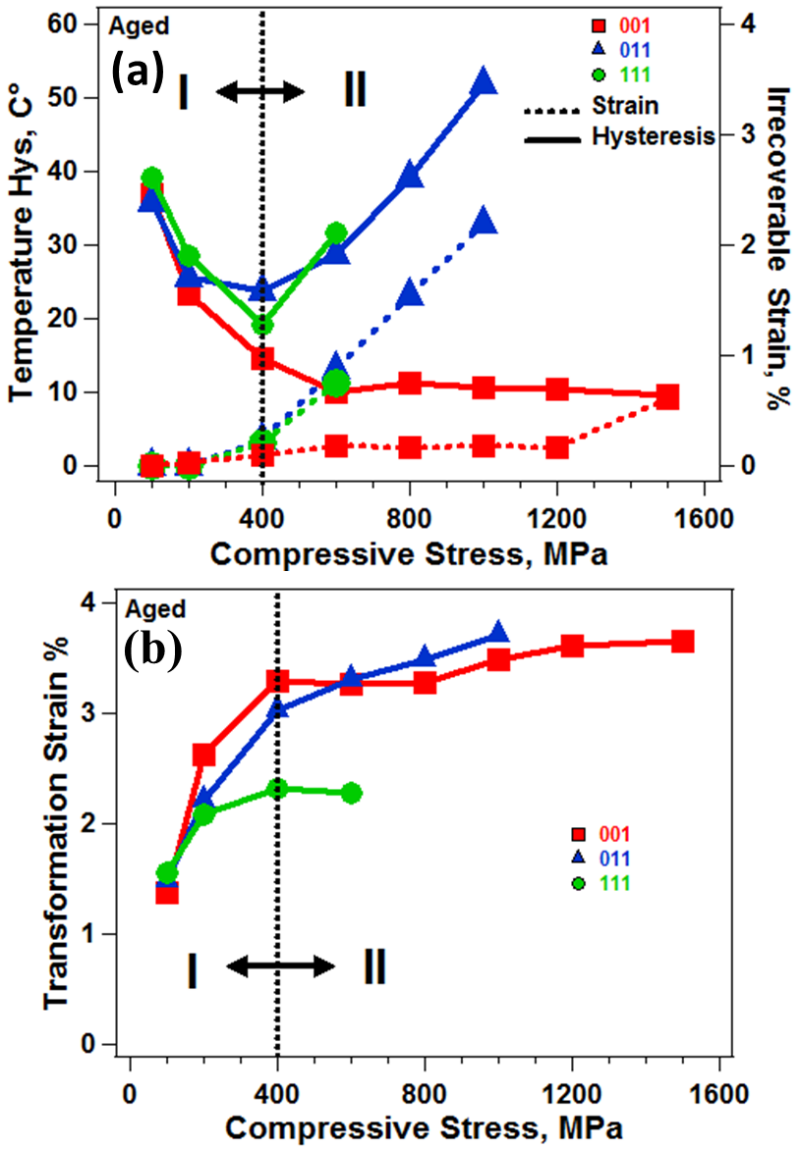


**Figure 5.11 (a)** Temperature hysteresis and irrecoverable strain as a function of applied stress and **(b)** transformation strain as a function of applied stress for aged alloys.

Figure 5.11a shows the thermal hysteresis and irrecoverable strain of aged single crystals as a function of applied stress in three orientations. In the aged condition, the hysteresis initially decreases rapidly for the all cases at low stress regime (Region I), and increases for [011] and [111]-oriented samples at high stress regime (Region II) while it is saturated for [001]-oriented crystals.

At 200 MPa, none of the samples produced irrecoverable strain. At 400 MPa, the onset of the irrecoverable strain occurred in all orientations. At 600 MPa, irrecoverable strain increased noticeably along the [011] and [111] orientations while it was almost constant along the [001] orientation. The critical stress level for slip is approximately 400 MPa for both [011] and [111] orientations. The increasing hysteresis at high stress regime (II) for the [011] and [111]-oriented samples can be attributed to increasing the plastic deformation with stress above 400 MPa.

In Figure 5.11b, it is clear that [111]-oriented single crystals have the smallest transformation strain. Maximum transformation strain of the hard [001] orientation is significantly higher than the softer [111]. Transformation strains were 3.27%, and 2.28% under 600 MPa in [001] and [111] orientations, respectively. It increased to 3.65% under 1500 MPa in [001].

The change in hysteresis with stress correlates well with the corresponding change in transformation strain. The initial decrease in hysteresis can be related to the decrease in the number of martensite variants (or increased number of favored martensite variants) formed with stress. Since fewer martensite variants are formed, the interaction between the variants diminishes, resulting in a smaller hysteresis. The initial wide hysteresis for the aged [001]-oriented single crystal compared to the homogenized [001]-oriented crystal is attributed to the friction dissipation due precipitates. As a conclusion, less variant for [001] and less friction cause low energy dissipation which leads to obtain small hysteresis.

These results confirm that the shape memory properties are strongly affected by the crystal orientation and precipitate formation.

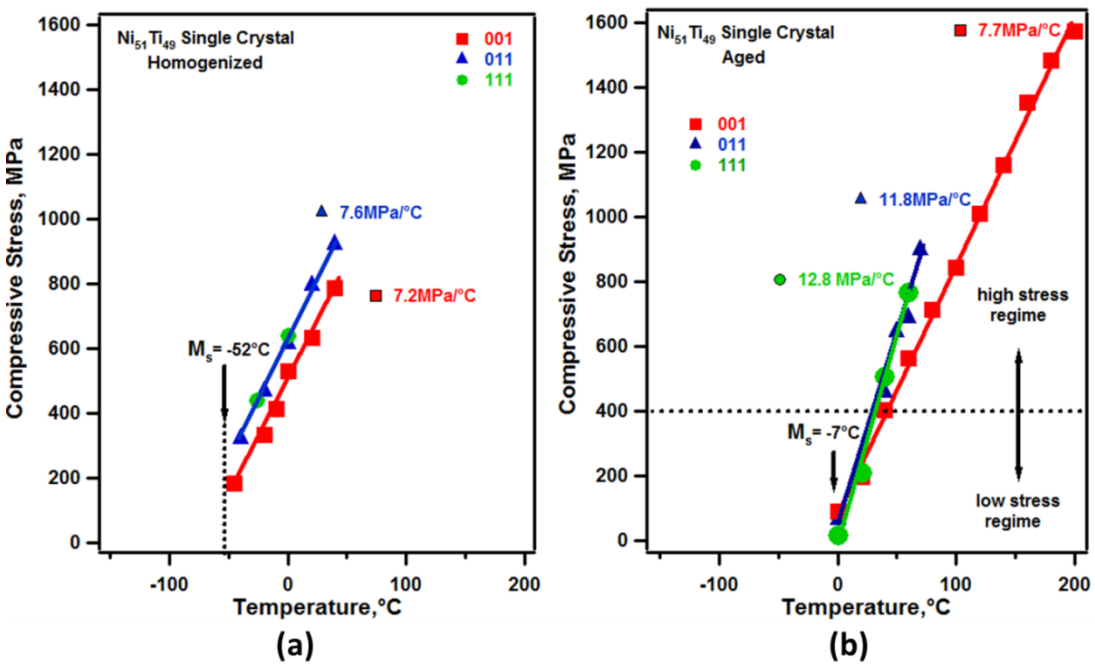


**Figure 5.12** Stress vs. temperature phase diagram of **(a)** homogenized and **(b)** aged $Ni_{51}Ti_{49}$ single-crystals.

In Figure 5.12 shows the critical stress for transformation as a function of temperature obtained from isothermal stress-strain responses for homogenized and aged $Ni_{51}Ti_{49}$ single crystal specimens. The $M_s$ of aged sample is determined from DSC tests in stress free condition and added to Figure 5.12 (shown with arrows). The TTs show a linearly increasing trend with stress which can be represented by the Classius-Clapeyron (Cs-Cl) relationship [127]. During forward transformation, the forward-start-temperature (FST) slopes were obtained as functions of stress for three orientations. Cs-Cl slopes of FST are 7.2 MPa/°C, 7.6 MPa/°C and 7.6 MPa/°C for [001], [011], and [111]-oriented homogenized samples, respectively. In aged conditions, Cs-Cl slopes of FST are 7.7 MPa/°C, 11.8 MPa/°C and 10.4 MPa/°C for [001], [011], and [111] orientations, respectively. The transformation stress levels are highly orientation dependent in high

stress regime while they are not orientation dependent in low stress regime for aged samples as shown in Figure 5.12b.

## 5.6 Conclusion

The effects of heat treatment and orientation on the shape memory properties of $Ni_{51}Ti_{49}$ single-crystals are investigated under compression, and results are summarized below:

1) Aged specimens have higher strength than the homogenized specimens in all orientations.
2) Almost perfect shape memory behavior was observed even at stress levels as high as 1500 MPa in [001]-oriented aged sample. The alloy's ability to show shape memory behavior under such high stresses can be attributed to the high strength of the precipitation-hardened single crystal due to a high density of precipitates. The largest superelastic window ($\Delta T = 140°C$) was observed.
3) In [001]-oriented aged sample, very narrow temperature hysteresis of 10°C was observed under ultra high compressive stress level of 1500 MPa with 3.65% transformation strain.
4) In [001] and [011] orientations, homogenized samples showed large hardening during loading compared to aged samples.
5) In the homogenized condition, [011]-oriented single crystals showed the highest thermal hysteresis when compared to the other two orientations. The hysteresis did not change with external stress for homogenized [001]-oriented $Ni_{51}Ti_{49}$ single-crystal. In the aged condition, the hysteresis initially decreases for the all cases at low stress levels, and increases for [011] and [111]-oriented samples at

high stress levels that can be attributed to increased plastic deformation with stress.

# 6 Two-Way Shape Memory Effect in $Ni_{51}Ti_{49}$ Single Crystals

## 6.1 Introduction

In this chapter, the TWSME properties of Ni-rich $Ni_{51}Ti_{49}$ single crystals oriented along the [111] direction were systematically investigated in compression. The TWSME responses of homogenized and aged samples along with the effects of deformation temperatures and applied stress were systematically investigated and discussed. Additionally, the TWSME response of [111]-oriented $Ni_{51}Ti_{49}$ was systematically investigated in compression after aging under stress. Since all the tests are done in compression, in this chapter, positive and negative TWSME strains mean that compressive and tensile strains, respectively, are observed upon cooling. DSC, TEM and thermomechanical tests (thermal cycling under stress and superelasticity) were carried out.

## 6.2 Influence of precipitates and dislocations on the two-way shape memory effect in $Ni_{51}Ti_{49}$ single crystal alloys

The single crystal samples were grown by the Bridgman technique in an inert gas atmosphere. The as-grown $Ni_{51}Ti_{49}$ single crystals were contained in Argon filled quartz ampoules and subjected to solution annealing at 1000℃ for 2 hours followed by water quenching. Then, some samples were subsequently aged at 500°C for 1.5 hours and water quenched. TWSME tests were done under 5 MPa of compressive loading, which is considered to be low to affect the variant selection but required to keep the grips in contact with the samples to measure strain.

The following methods were used to generate the TWSME which are shown in Figure 6.1.

1. The compressive deformation of martensite below $M_f$.

2. The compressive deformation of austenite above $M_d$ where the specimen would plastically deform without phase transformation.

3. Temperature cycling under constant compressive load.

4. The compressive loading of austenite at temperatures below $M_d$ where both the phase transformation and plastic deformation could take place.

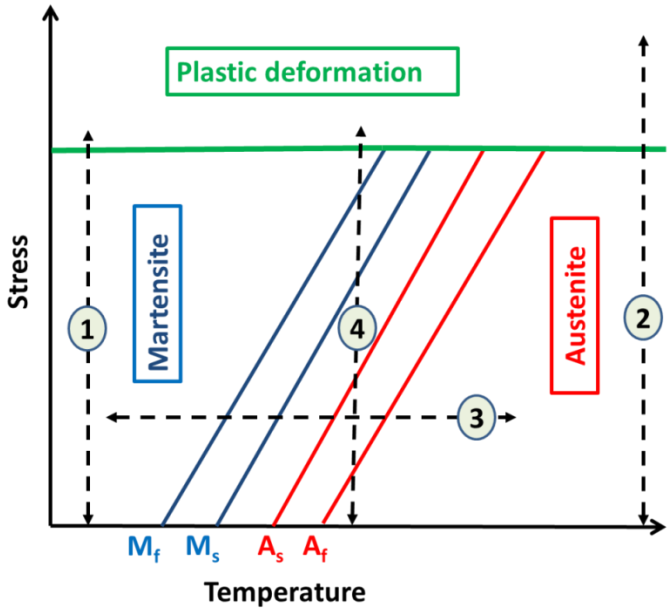


**Figure 6.1** Schematic of the loading paths in stress-temperature phase diagram. Critical stress for plastic deformation is assumed to be constant for simplicity.

### 6.2.1 DSC Results

According to DSC results, the TTs of homogenized $Ni_{51}Ti_{49}$ single crystal alloy were; $M_s$ = -52°C, $M_f$ = -68°C, $A_s$ = -37°C, $A_f$ = -23°C, and the TTs of aged (500°C - 1.5h) $Ni_{51}Ti_{49}$ single crystal alloy were; $R_s$ = 25°C, $R_f$ = 16°C, $M_s$ = -7°C, $M_f$ = -16°C, $A_s$ = 27°C, $A_f$ = 33°C (Chapter 5.2).

### 6.2.2 Microstructure of solution-treated and aged single crystals

TEM observation was carried out to investigate the microstructure of the solution-treated and aged specimens. The solution-treated specimen was composed of a single B2 austenite phase, while $Ni_4Ti_3$ precipitates were observed in the aged specimen. Figures 6.2a and 6.2b show the bright field STEM image taken from the aged specimen and the corresponding selected area diffraction (SAD) pattern, respectively. There are superlattice reflections at 1/7 positions along $<321>_{B2}^{*}$ in reciprocal space, which correspond to the $Ni_4Ti_3$ precipitates. The average size of the $Ni_4Ti_3$ precipitates is around 180 nm. The R-phase can be confirmed by the superlattice reflections at 1/3 positions along $<110>_{B2}^{*}$.

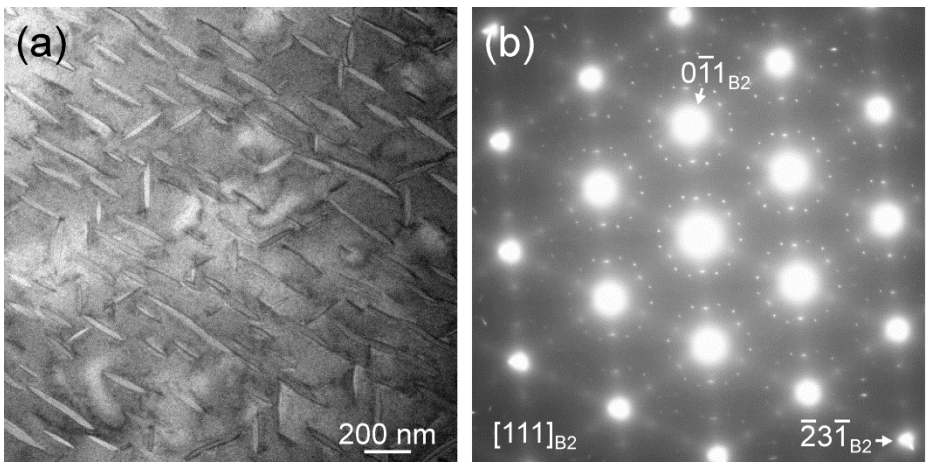


**Figure 6.2 (a)** Bright field STEM micrograph and **(b)** corresponding SAD pattern of the $Ni_{51}Ti_{49}$ single crystal aged at 500°C for 1.5 hours.

Figure 6.3 shows the HRTEM micrograph of the aged specimen and corresponding fast Fourier transforms (FFTs). The symbols A, R and Ni4Ti3 represent B2 austenite, R-phase and $Ni_4Ti_3$ precipitate, respectively. It is confirmed that R-phase is formed around the precipitates due to the stress fields caused by the precipitates [128]. The orientation relationship between R-phase and $Ni_4Ti_3$ precipitate was reported as $[111]_R$ ($[0001]_H$) // $[111]_{Ni4Ti3}$ ($[0001]_H$) [129]. Considering the crystal orientations shown in Figure 6.3a, it was found that the R-phase and $Ni_4Ti_3$ precipitates observed in Figure 6.3a have the same orientation relationship ($[111]_R$ // $[111]_{Ni4Ti3}$).

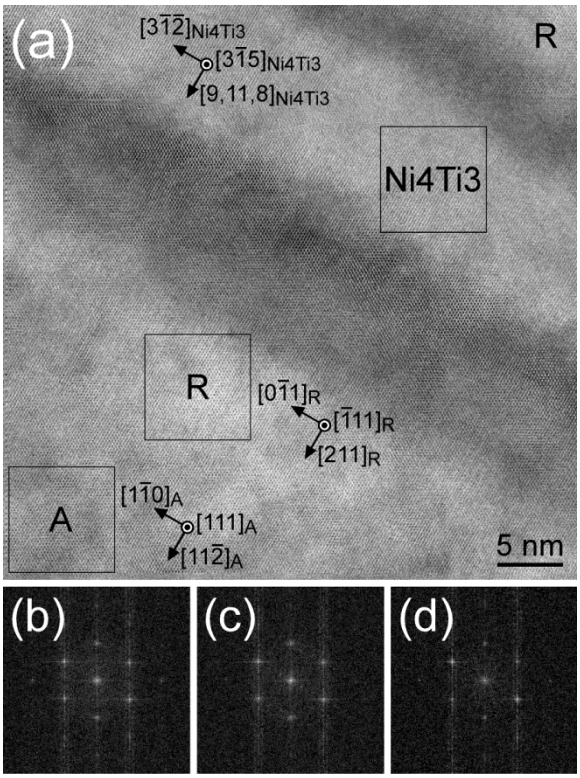


**Figure 6.3 (a)** High resolution bright field STEM micrograph of the aged specimen and **(b, c and d)** FFTs obtained from the framed areas A, R and Ni4Ti3 in (a), respectively. Symbols A, R and Ni4Ti3 indicate B2 austenite, R-phase and $Ni_4Ti_3$ precipitate, respectively.

### 6.2.3 TWSME of solution-treated single crystals

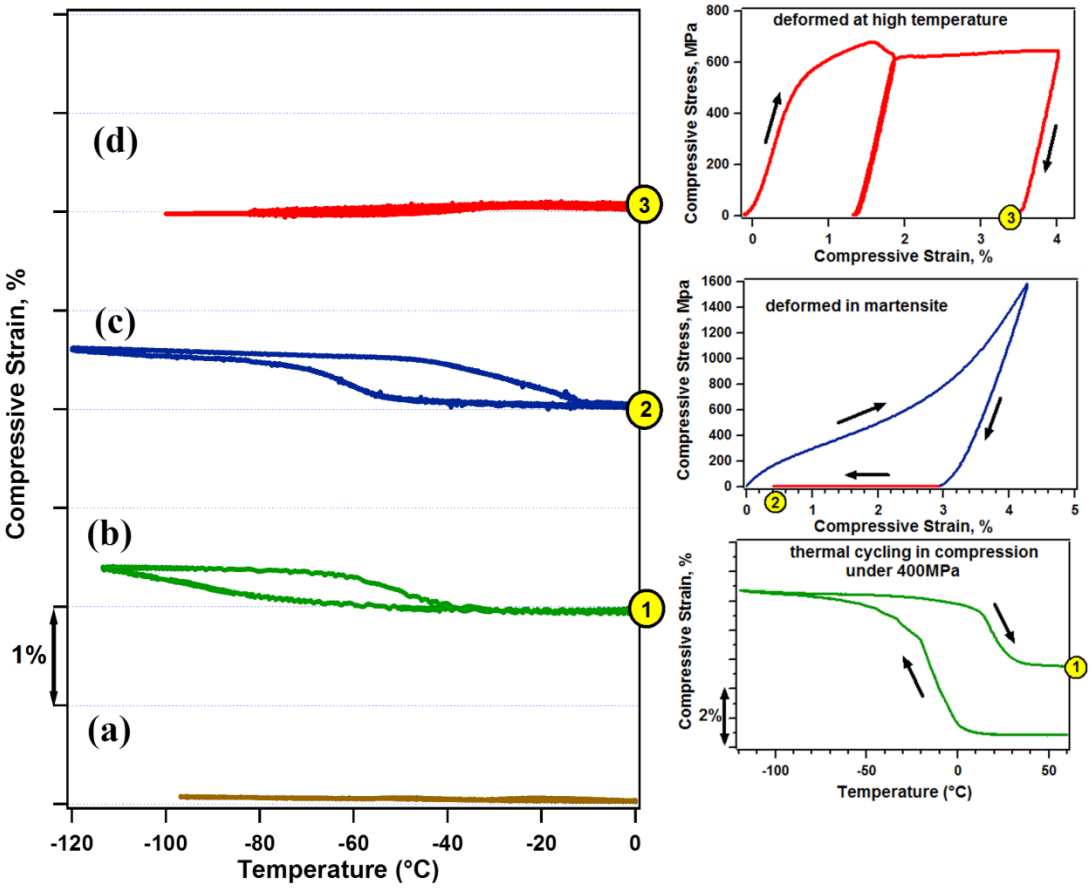


**Figure 6.4** TWSME of the solution-treated [111]-oriented $Ni_{51}Ti_{49}$ single crystal after **a)** solution treatment, **b)** thermal cycling under 400 MPa, **c)** deformation in martensite phase at -150°C, and **d)** deformation at 200°C which is above $M_d$. Corresponding stress-strain and strain-temperature graphs are inserted to show compression response to obtain TWSME.

In order to reveal TWSME of solution-treated $Ni_{51}Ti_{49}$ single crystal alloys along the [111] orientation, the samples were deformed at selected conditions in compression as-shown in Figure 6.4. In Figure 6.4a, the specimen was loaded to 5 MPa in austenite and then it was cooled down below $M_f$ and then heated above the $A_f$ to complete one thermal cycling cycle that is the TWSME behavior. It is clear that the TWSME strain

($\varepsilon_{tw}$) was not observed right after solution treatment. Figure 6.4b shows the TWSME experiment after thermal cycling under 400 MPa where an irrecoverable strain of 2.3% was observed upon completion of the cycle. A positive (compressive) TWSME strain of 0.41% was obtained in this case. Figure 6.4c shows the TWSME after deformation in martensite where the single crystal was compressed till total-strain ($\varepsilon_{tot}$) of 4.2% and then unloaded at -150 °C. It was heated to a temperature above $A_f$ where the remained strain ($\varepsilon_{re}$) was recovered and an irrecoverable strain of 0.4% was observed. When the sample is thermally cycled under 5 MPa, compressive (positive) TWSME strain of 0.6% was observed. Figure 6.4d shows the compressive strain vs. temperature result after deformation above $M_d$ at 200°C. The sample was deformed up to 3.6% and then unloaded where 3.2% irrecoverable strain is observed. During thermal cycling under 5 MPa, no TWSME strain was observed.

### 6.2.4 TWSME of as-aged [111]-oriented $Ni_{51}Ti_{49}$

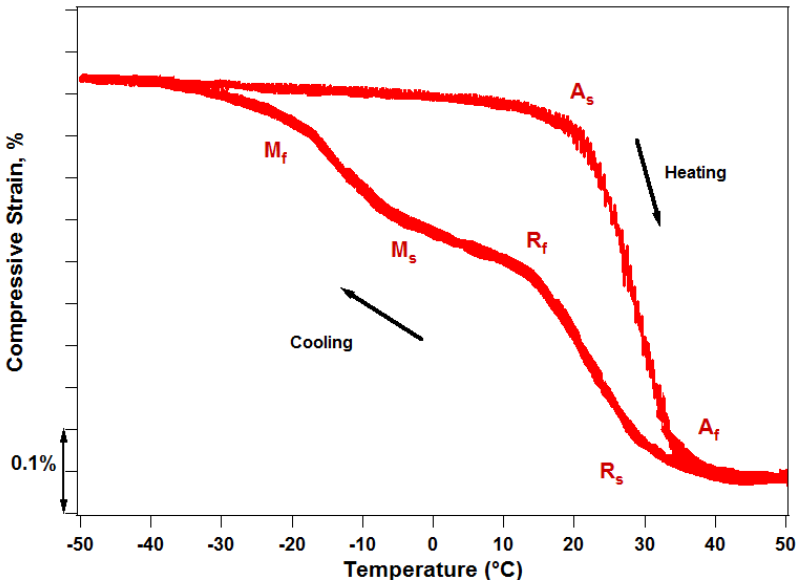


**Figure 6.5** TWSME of as-aged $Ni_{51}Ti_{49}$ single crystal alloys.

Figure 6.5 shows the thermal cycling responses of as-aged $Ni_{51}Ti_{49}$ single crystal alloys under 5 MPa applied stress. The specimens were cooled down below $M_f$ and then heated above $A_f$ where $\varepsilon_{tw}$ of 0.4% was obtained. The aged single crystals showed the two-stage (B2-R-B19′) transformation during cooling, and both transformations produced the positive $\varepsilon_{tw}$.

### 6.2.5 TWSME of aged $Ni_{51}Ti_{49}$ after deformation in martensite phase

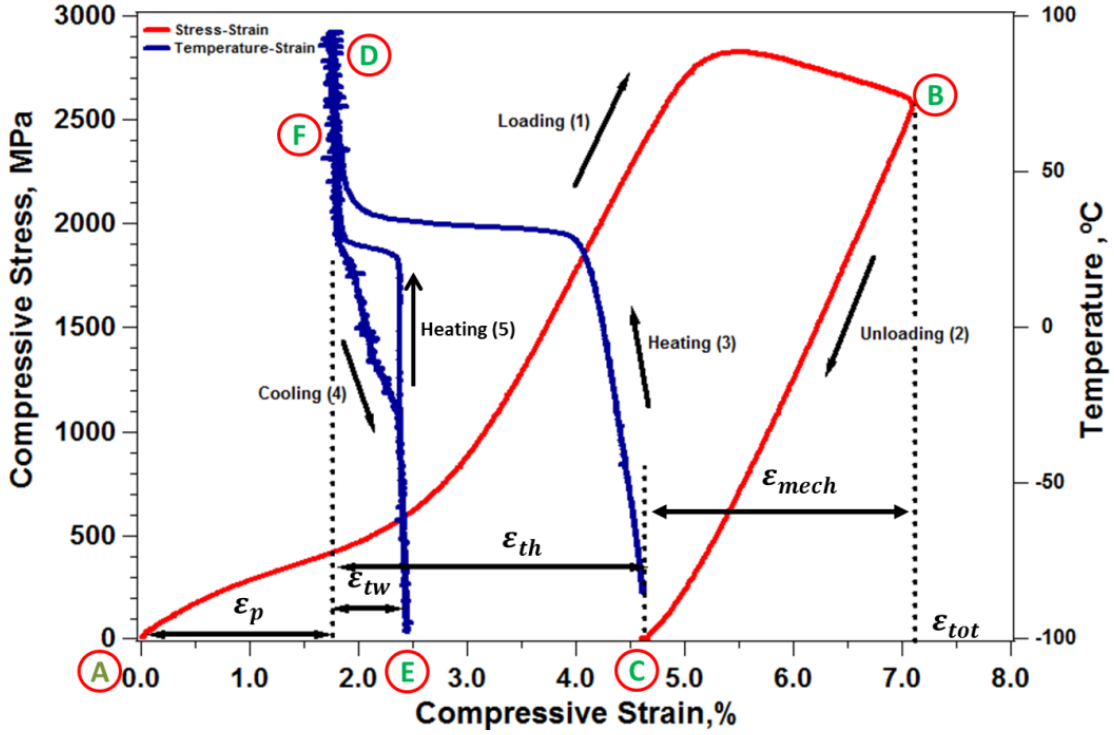


**Figure 6.6** Stress vs Strain and Temperature vs Strain curves of aged $Ni_{51}Ti_{49}$ single crystal alloys.

Figure 6.6 shows the deformation of aged single crystal in martensite and the corresponding TWSME behavior. Upon application of compressive stress, variant reorientation and then elastic deformation of martensite plates take place. At higher

stress, a second yield was observed which can be attributed to the plastic deformation of martensite. The test specimen was loaded (A-B) to a total-strain of 7% and unloaded (B-C) at -80 °C. Upon unloading, a remained strain of 4.6% and recovery strain ($\varepsilon_{mech}$) of 2.4% were observed. Subsequent heating (C-D) resulted in thermally induced recovery strain ($\varepsilon_{th}$) of 2.8% and plastic strain ($\varepsilon_p$) of 1.8%. The specimen is cooled down below $M_f$ (D–E) and then heated above the $A_f$ (E-F) and compressive (positive) $\varepsilon_{tw}$ of 0.7% is generated. Since the aged single crystal showed $\varepsilon_{tw}$ of 0.4% before deformation (Figure 6.5), we can conclude that the plastic deformation of martensite increased $\varepsilon_{tw}$. It is noted that contribution of R-phase transformation to $\varepsilon_{tw}$ did not change with deformation and the 0.3% increase of $\varepsilon_{tw}$ is produced by the subsequent B19′ transformation.

### 6.2.6 TWSME of aged $Ni_{51}Ti_{49}$ after deformation above $M_d$

TWSME of the aged single crystal was determined after selected level of deformations above $M_d$ (at 200°C) and shown in Figure 6.7. If loaded at a temperature above $M_d$, NiTi behaves like a conventional alloy with the material exhibiting elastic and then plastic deformations. The aged single crystal was loaded (A-B) to selected total-strain value and then unloaded (B-C) at 200 °C. The specimen was cooled down (C-D) and heated (D-E) to observe TWSME. The elastic deformation is observed until a strain of 0.8% and yield stress is determined as 600 MPa. The deformed specimen shows the two-stage (B2-R-B19′) transformation during cooling and one stage (B19′-B2) transformation during heating of TWSME. After TWSME test the sample is loaded to next total-strain value and TWSME test is repeated. Tensile (negative) $\varepsilon_{tw}$ of 1.4, 1.7, 1.9 and 1.9% were observed after $\varepsilon_{tot}$ of 2, 4, 6, and 10 %, respectively. Thus, it is clear that when an aged alloy is plastically deformed in austenite, the negative TWSME is observed

as shown in Figure 6.7. It should be noted that both the R-phase and B19′ transformations produced the negative $\varepsilon_{tw}$.

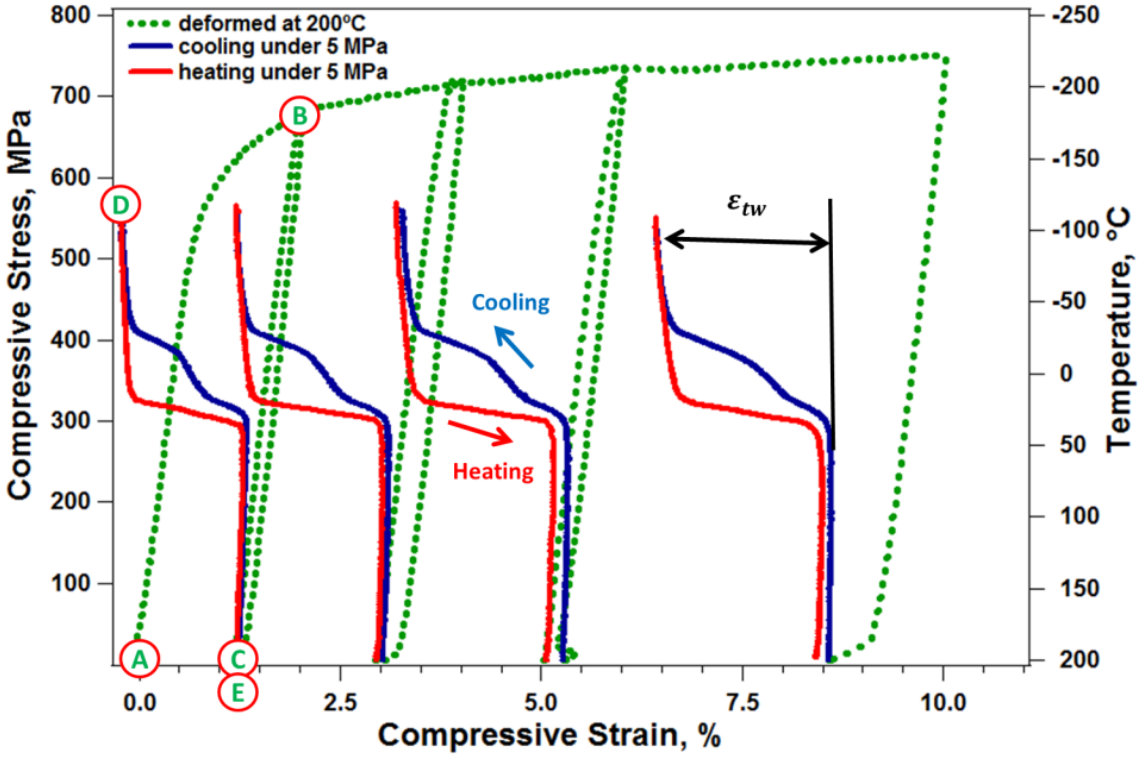


**Figure 6.7** Incremental compressive stress-strain response of aged $Ni_{51}Ti_{49}$ single crystal alloys at 200°C. TWSME after each loading cycle is included in the graph.

### 6.2.7 TWSME of aged $Ni_{51}Ti_{49}$ single crystal after thermal cycling under constant stress

Figure 6.8 shows the response of aged sample that is loaded to 600 MPa in austenite (1-2), and then thermally cycled (2-4). The transformation strain was 2.4% and the irrecoverable strain ($\varepsilon_{irr}$) was 0.8 % under 600 MPa. Then, TWSME test was performed (5-6-7) and negative (tensile) $\varepsilon_{tw}$ of 1.4% was obtained. The aged specimen

showed the negative TWSME after thermal cycling under stress, which is in contrast to the solution-treated specimen which showed the positive TWSME (Figure 6.4b).

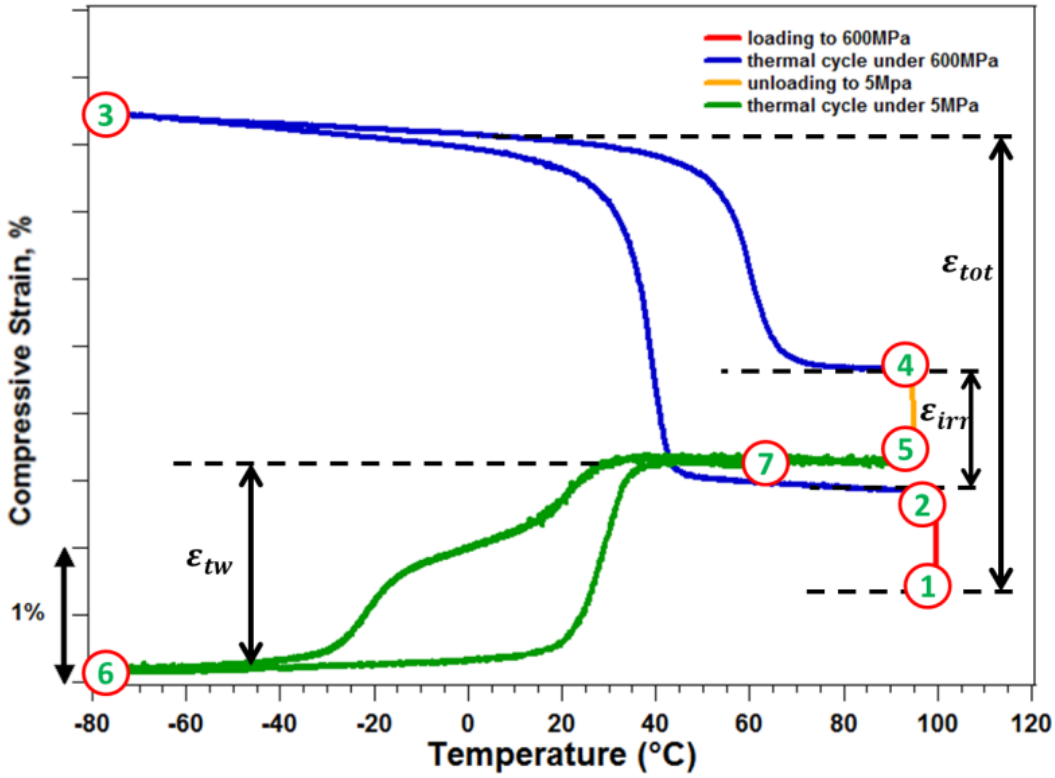


**Figure 6.8** Thermal cycling under 600 MPa and the corresponding TWSME of aged $Ni_{51}Ti_{49}$ single crystal.

### 6.2.8 TWSME of aged $Ni_{51}Ti_{49}$ single crystal after deformation of austenite below $M_d$

Figure 6.9a shows that compressive stress vs strain curves at 60 °C which is above $A_f$ but below $M_d$. The sample was loaded till the selected strain levels of 2, 7, 11, 14, and 20% and unloaded. After unloading, the sample was heated to 150 °C to transform the retained martensite to austenite where only a small partial recovery strain is observed. Then, TWSME tests were performed. Figure 6.9b shows the TWSME

responses of the single crystal that are conducted after unloading and subsequent heating as marked in Figure 6.9a. The two-stage (B2-R-B19′) transformation was observed during cooling and one stage (B19′-B2) transformation during heating of TWSME. Tensile (or negative) $\varepsilon_{tw}$ of 1, 1.3, 1.1, 0.8, and 0.6% was observed after deformation strain of 2, 7, 11, 14, and 20%, respectively.

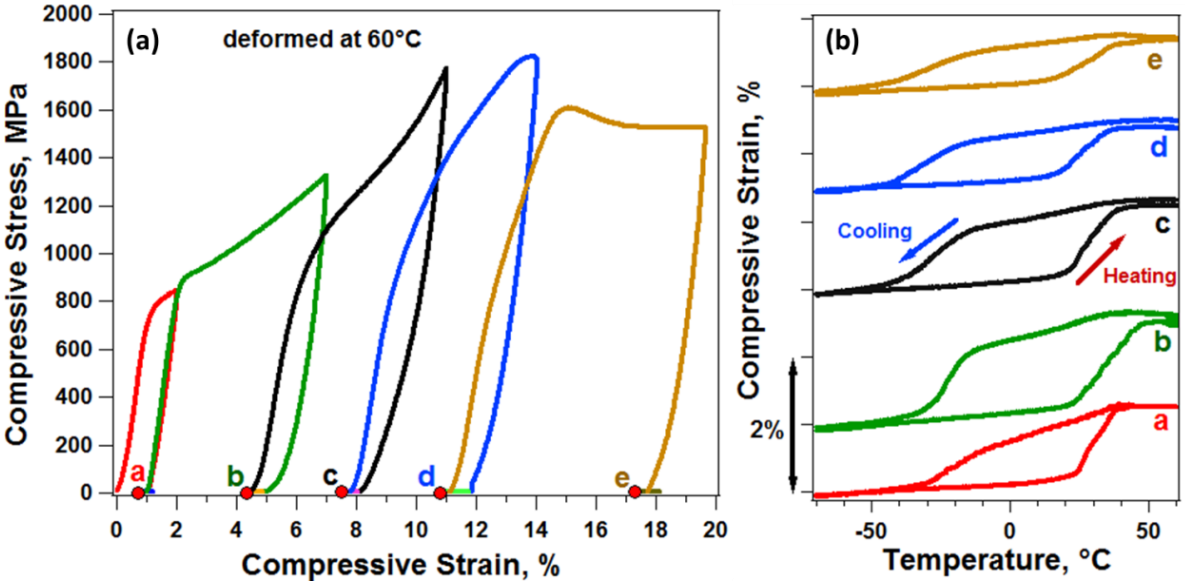


**Figure 6.9 a)** Stress-strain curves of aged $Ni_{51}Ti_{49}$ single crystal alloys subjected to selected levels of total strain at 60°C and **b)** the corresponding TWSME responses.

### 6.2.9 Discussion

#### 6.2.9.1 TWSME of solution-treated single crystals

The $Ni_{51}Ti_{49}$ single crystal did not show TWSME right after solution treatment, whereas positive TWSME was observed in the solution-treated specimens deformed in martensite and by thermal cycling under high stress (resulted in irrecoverable strain) experiments. On the other hand, the solution-treated specimen deformed in austenite did not show TWSME. It has been reported by many researchers that the positive TWSME

can be obtained when a specimen is plastically deformed in the martensite phase [5, 33, 34, 103, 128, 130-134]. Since the solution-treated specimen showed positive TWSME after thermal cycling under stress, it is considered that the dislocations were introduced in the martensite phase during thermal cycling. The positive TWSME has been also confirmed in $Ni_{49.7}Ti_{50.3}$, $Ni_{50}Ti_{50}$ and $Ni_{50.2}Ti_{49.8}$ alloys after thermal cycling under stress [90, 135, 136]. Miyazaki and Kimura investigated the effects of prestrain on the TWSME as a function of deformation temperature in a solution-treated $Ni_{51}Ti_{49}$ alloy [137]. They observed that in tension, the positive TWSME can be observed when dislocations are introduced in the martensite, while the dislocations introduced in the austenite phase did not result in TWSME. They have attributed the observed TWSME to the spring-back behavior of dislocations. When the deformed martensite is transformed back to austenite by heating, the elongated specimen will contract with a large driving force. The work hardened dislocation structure will also be contracted upon the reverse transformation. After the contraction, the dislocations will produce a spring-back force to make the specimen regain an elongation. Therefore, the dislocations introduced in the martensite produce the positive TWSME. On the other hand, the spring-back force cannot be caused by the dislocations introduced in the austenite phase, resulting in lack of TWSME. This explanation of the positive TWSME can be also applied to the specimens deformed in compression presented in this study. The dislocation structure formed in martensite by compressive deformation will be elongated upon the reverse transformation during heating. The spring-back force produced by the elongated dislocation structure makes the specimen regain a compression, resulting in the positive TWSME (Figure 6.4b and 6.4c). On the other hand, the solution-treated specimen deformed in austenite did not show

TWSME (Figure 6.4d) since the introduced dislocations do not produce the spring-back force.

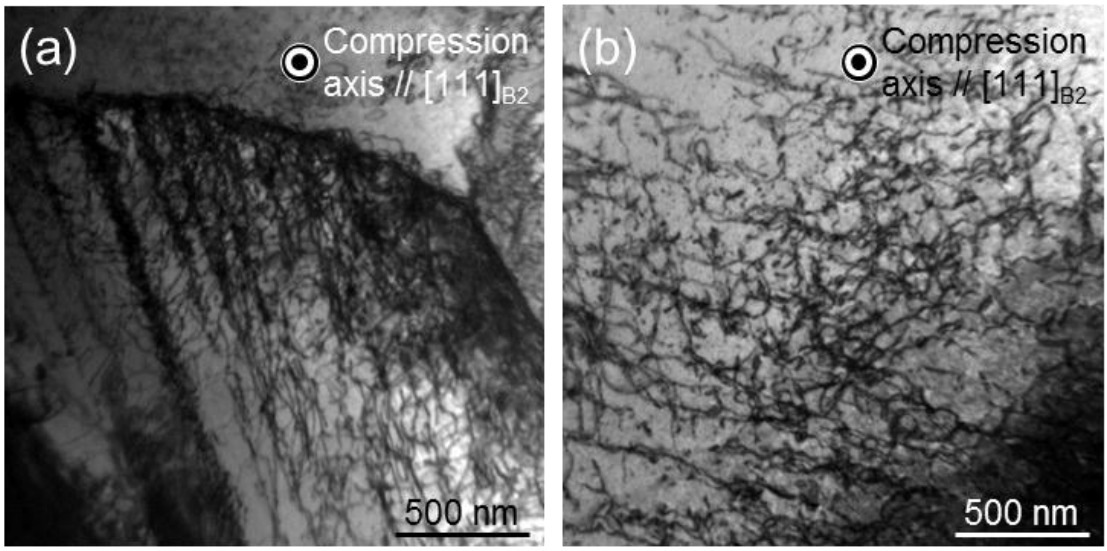


**Figure 6.10** Bright field TEM images of the solution-treated $Ni_{51}Ti_{49}$ single crystals **(a)** deformed in martensite and **(b)** deformed in austenite.

Figure 6.10a shows the bright field TEM image taken at room temperature from the solution-treated specimen deformed in martensite as shown in Figure 6.4c. The specimen is austenite since the TTs are below room temperature as shown in Figure 5.1a. It is clear that the dislocations are aligned on specific crystal planes. Previously, Kudoh et al. suggested that the slip system of the B19′ martensite is $(001)_{B19'}[100]_{B19'}$ [138]. Considering the lattice correspondence between the martensite and austenite (Table 6.1), the $(001)_{B19'}[100]_{B19'}$ system corresponds to one of the $\{011\}_{B2}<100>_{B2}$ systems, for example $(110)_{B2}[001]_{B2}$, in the austenite. The dislocations formed in the martensite become the dislocations in the austenite when the specimen is transformed back to the austenite upon heating. Since there is only one $(001)_{B19'}[100]_{B19'}$ slip system in a single

martensite variant, the dislocations formed in a martensite variant may align on the $(001)_{B19'}$ planes. When the specimen is transformed back to the austenite by heating, the dislocations align on one of the $\{011\}_{B2}$ planes in the austenite. Such aligned dislocations are considered to help the selection of specific martensite variants during cooling. As a result, the specimen deformed in the martensite phase shows improved positive TWSME (Figure 6.4b and 6.4c). When the specimen is deformed in the austenite phase, there are many $\{011\}_{B2}<100>_{B2}$ slip systems available for deformation (such as $(110)_{B2}[001]_{B2}$ and $(101)_{B2}[010]_{B2}$). Moreover, there are other slip systems such as $\{001\}_{B2}<100>_{B2}$ [139, 140] that prevents the alignment of dislocations on certain planes as shown in Figure 10b. Therefore, the selection of martensite variants does not occur and TWSME is not observed in the specimen deformed in austenite (Figure 6.4d).

**Table 6.1** Twelve lattice correspondence variants (CVs) [141]. Subscripts M and A indicate martensite and austenite, respectively.

| | CV1 | CV1′ | CV2 | CV2′ | CV3 | CV3′ | CV4 | CV4′ | CV5 | CV5′ | CV6 | CV6′ |
|---|---|---|---|---|---|---|---|---|---|---|---|---|
| $[100]_M$ | $[100]_A$ | $[\bar{1}00]_A$ | $[100]_A$ | $[\bar{1}00]_A$ | $[010]_A$ | $[0\bar{1}0]_A$ | $[010]_A$ | $[0\bar{1}0]_A$ | $[001]_A$ | $[00\bar{1}]_A$ | $[001]_A$ | $[00\bar{1}]_A$ |
| $[010]_M$ | $[011]_A$ | $[0\bar{1}\bar{1}]_A$ | $[0\bar{1}1]_A$ | $[01\bar{1}]_A$ | $[101]_A$ | $[\bar{1}0\bar{1}]_A$ | $[10\bar{1}]_A$ | $[\bar{1}01]_A$ | $[110]_A$ | $[\bar{1}\bar{1}0]_A$ | $[\bar{1}10]_A$ | $[1\bar{1}0]_A$ |
| $[001]_M$ | $[0\bar{1}1]_A$ | $[0\bar{1}1]_A$ | $[0\bar{1}\bar{1}]_A$ | $[0\bar{1}\bar{1}]_A$ | $[10\bar{1}]_A$ | $[10\bar{1}]_A$ | $[\bar{1}0\bar{1}]_A$ | $[\bar{1}0\bar{1}]_A$ | $[\bar{1}10]_A$ | $[\bar{1}10]_A$ | $[\bar{1}\bar{1}0]_A$ | $[\bar{1}\bar{1}0]_A$ |

#### 6.2.9.2 TWSME of aged single crystals

The $Ni_{51}Ti_{49}$ single crystal showed positive TWSME after aging at 500 °C for 1.5 hours as shown in Figure 6.5, although the solution-treated single crystal did not show any TWSME. One of the reasons for the positive TWSME could be the inhomogeneous distribution of $Ni_4Ti_3$ precipitates which is produced by the inhomogeneity of single crystals along the single crystal growth direction. The stress fields around the precipitates cause the selection of martensite variants, which is considered to result in the positive

TWSME. It should also be noted that the applied stress of 5 MPa (to ensure the contact of the grips) could result in selection of R-phase variants since R-phase could easily be stress-induced due to its small transformation strain compared to B19′ martensite. The stress-induced R-phase is considered to transform to specific variants of B19′ martensite which produce further compressive strain during cooling.

It is clear that when the aged samples are deformed in martensite, they showed an increased positive $\varepsilon_{tw}$. In contrast, when they are deformed in austenite or by the thermal cycling under stress, negative $\varepsilon_{tw}$ is observed. In order to understand the origin of negative $\varepsilon_{tw}$, microstructure of aged single crystals are investigated by TEM.

TEM observation was conducted from the direction parallel to the compression axis, $[111]_{B2}$ orientation, for the aged crystals deformed in martensite and austenite. Figure 6.11 depicts the bright field images showing the $Ni_4Ti_3$ precipitates and B19′ martensite and the corresponding SAD patterns of the deformed samples. It should be noted that in addition to austenite, martensite was also observed in all aged specimens. Since the $M_s$ of the aged specimen is -7 °C as shown in Figure 5.1b, it is believed that the martensite phase was formed thermally in the twin-jet polishing process which was made at around -15 °C. In the specimen deformed in austenite, the $Ni_4Ti_3$ precipitates cannot be clearly observed because of the high density of dislocations around the precipitates (Figure 6.11c).

The dominant martensite variants were found to be different in the two cases. There are twelve lattice correspondence variants in the B19′ martensite [141] as shown in Table 6.1. The martensite variants which were mainly observed in the aged specimen deformed in martensite are CV1, CV1′, CV3, CV3′, CV5 and CV5′. The variants CV1

and CV3 can be confirmed in the SAD pattern shown in Figure 6.11b. On the other hand, for the aged specimen deformed in austenite, the dominant martensite variants are CV2, CV4 and CV6 (Figure 6.11d).

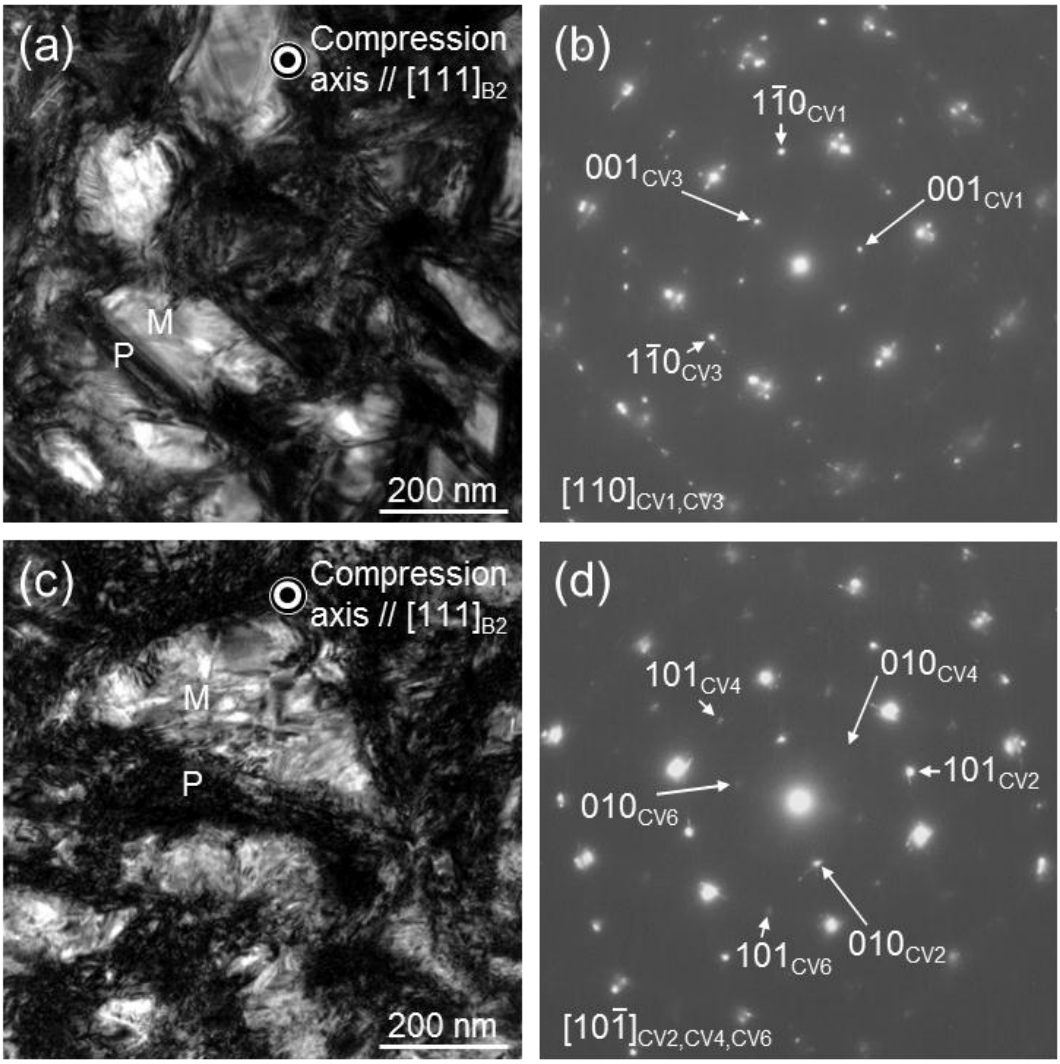


**Figure 6.11** Bright field TEM images showing the $Ni_4Ti_3$ precipitates and B19′ martensite and the corresponding SAD patterns of the aged $Ni_{51}Ti_{49}$ single crystals deformed in **(a and b)** martensite and **(c and d)** austenite. Symbols P and M in the bright field images indicate $Ni_4Ti_3$ precipitate and B19′ martensite, respectively.

The transformation strain along the $[111]_{B2}$ direction was calculated based on the lattice deformation theory [142] and the results are shown in Table 6.2. In this theory,

austenite is assumed to transform fully into a single variant martensite without the twins. The following lattice parameters were used to calculate the transformation strain: $a_0$ = 0.3015 nm [143], and $a$ = 0.2889 nm, $b$ = 0.4120 nm, $c$ = 0.4622 nm and $\beta$ = 96.8° [144]. The positive sign and negative sign of the transformation strain correspond to the extension and contraction along the $[111]_{B2}$ direction, respectively. The martensite variants which were mainly observed in the aged specimen deformed in martensite (CV1, CV1′, CV3, CV3′, CV5 and CV5′) produce the contraction of the specimen, corresponding to the positive TWSME after compression. On the other hand, the martensite variants observed in the aged specimen deformed in austenite (CV2, CV4 and CV6) results in tensile strain corresponding to the negative TWSME after compression.

**Table 6.2** Directions derived from the $[111]_A$ direction and calculated transformation strains for the twelve martensite variants. The positive sign and negative sign of the transformation strain correspond to the extension and contraction along the $[111]_A$ direction, respectively.

| | CV1 | CV1′ | CV2 | CV2′ | CV3 | CV3′ | CV4 | CV4′ | CV5 | CV5′ | CV6 | CV6′ |
|---|---|---|---|---|---|---|---|---|---|---|---|---|
| Axial direction: $[111]_A$ | $[110]_M$ | $[\bar{1}\bar{1}0]_M$ | $[10\bar{1}]_M$ | $[\bar{1}0\bar{1}]_M$ | $[110]_M$ | $[\bar{1}\bar{1}0]_M$ | $[10\bar{1}]_M$ | $[\bar{1}0\bar{1}]_M$ | $[110]_M$ | $[\bar{1}\bar{1}0]_M$ | $[10\bar{1}]_M$ | $[\bar{1}0\bar{1}]_M$ |
| Transformation strain (%) | -3.64 | -3.64 | 9.79 | -1.34 | -3.64 | -3.64 | 9.79 | -1.34 | -3.64 | -3.64 | 9.79 | -1.34 |

It should be noted that the negative TWSME was only observed in the aged specimens, indicating that the $Ni_4Ti_3$ precipitates play an important role in the formation of negative TWSME. The aged specimens deformed in austenite and by thermal cycling under stress show the two-stage (B2-R-B19′) transformation and even the B2-R transformation alone produces the negative $\varepsilon_{tw}$ as shown in Figures 6.7 and 6.8. Since B2-R transformation occurs around the $Ni_4Ti_3$ precipitates, we can conclude that the specific

variants of the R-phase that produce the negative TWSME strain are formed during cooling by the internal stresses around the $Ni_4Ti_3$ precipitates.

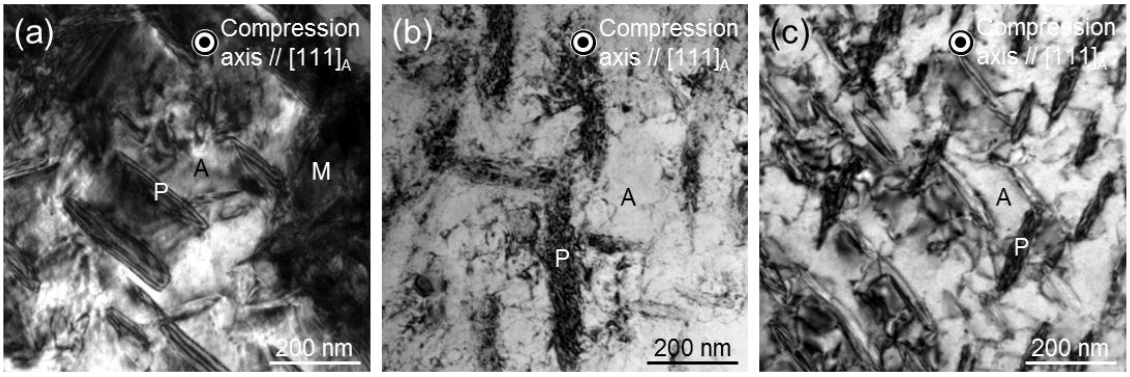


**Figure 6.12** Bright field TEM images showing the $Ni_4Ti_3$ precipitates and B2 austenite of the aged specimen **(a)** deformed in martensite, **(b)** deformed in austenite and **(c)** deformed by thermal cycling under stress. Symbols P, A and M indicate $Ni_4Ti_3$ precipitate, B2 austenite and B19′ martensite, respectively.

The bright field images of the aged single crystal after deformation which contain $Ni_4Ti_3$ precipitates and B2 austenite with dislocations were shown in Figure 6.12. In Figure 6.12a, dislocations were observed between the precipitates in the aged specimen deformed in martensite (see Figure 6.6). On the other hand, it is clear that the dislocations accumulate around the precipitates in the aged specimens deformed in austenite (see Figure 6.7) as-shown in Figure 6.12b. Figure 6.12c shows the bright field image of the aged specimen deformed by thermal cycling under stress (see Figure 6.8). The dislocations introduced by the thermal cycles are around the precipitates similar to the aged specimen deformed in austenite (Figure 6.12b) which shows the negative TWSME. Therefore, it is considered that the dislocations were mainly introduced in austenite

during thermal cycling under stress and the specimen showed negative TWSME as shown in Figure 6.8.

Since dislocations did not accumulate around the precipitates in the aged specimen deformed in martensite, dislocations are considered to be difficult to form on the boundary between the precipitate and martensite. Thus, it is expected that the dislocations do not affect the B2-R transformation considerably since they do not alter the stress fields around the precipitates. However, dislocations affect the subsequent B19′ transformation, resulting in the positive TWSME similar to the solution-treated specimen deformed in martensite. This is supported by the experimental results shown in Figures 6.5 and 6.6 where further plastic deformation of martensite did not increase the positive $\varepsilon_{tw}$ produced by B2-R transformation significantly but increased the strain produced by the subsequent B19′ transformation. On the other hand, in the aged specimen deformed in austenite and deformed by the thermal cycling under stress, the stress fields around the precipitates might be affected by the dislocations which are formed on the boundary between the precipitate and austenite matrix. It is known that the dislocation formation around the precipitates could result in back stresses around the particles [145, 146]. The Orowan dislocation loops were observed around precipitates and were responsible for creation of back stress [147]. Since B2-R transformation occurs around the precipitates due to the stress fields caused by lattice mismatch, the formation of back stress due to dislocation formation leads to the selection of R-phase variants that will result in tensile (negative) strain in the loading direction. It has been reported that the $[111]_R$ direction is derived from $<111>_{B2}$ directions and is the most expansible direction during the B2-R transformation [129]. Therefore, it is considered that the specific R-phase variants with

$[111]_R$ direction being parallel to the compression axis of $[111]_{B2}$ are selected due to the back stress creation to produce the tensile (negative) strain.

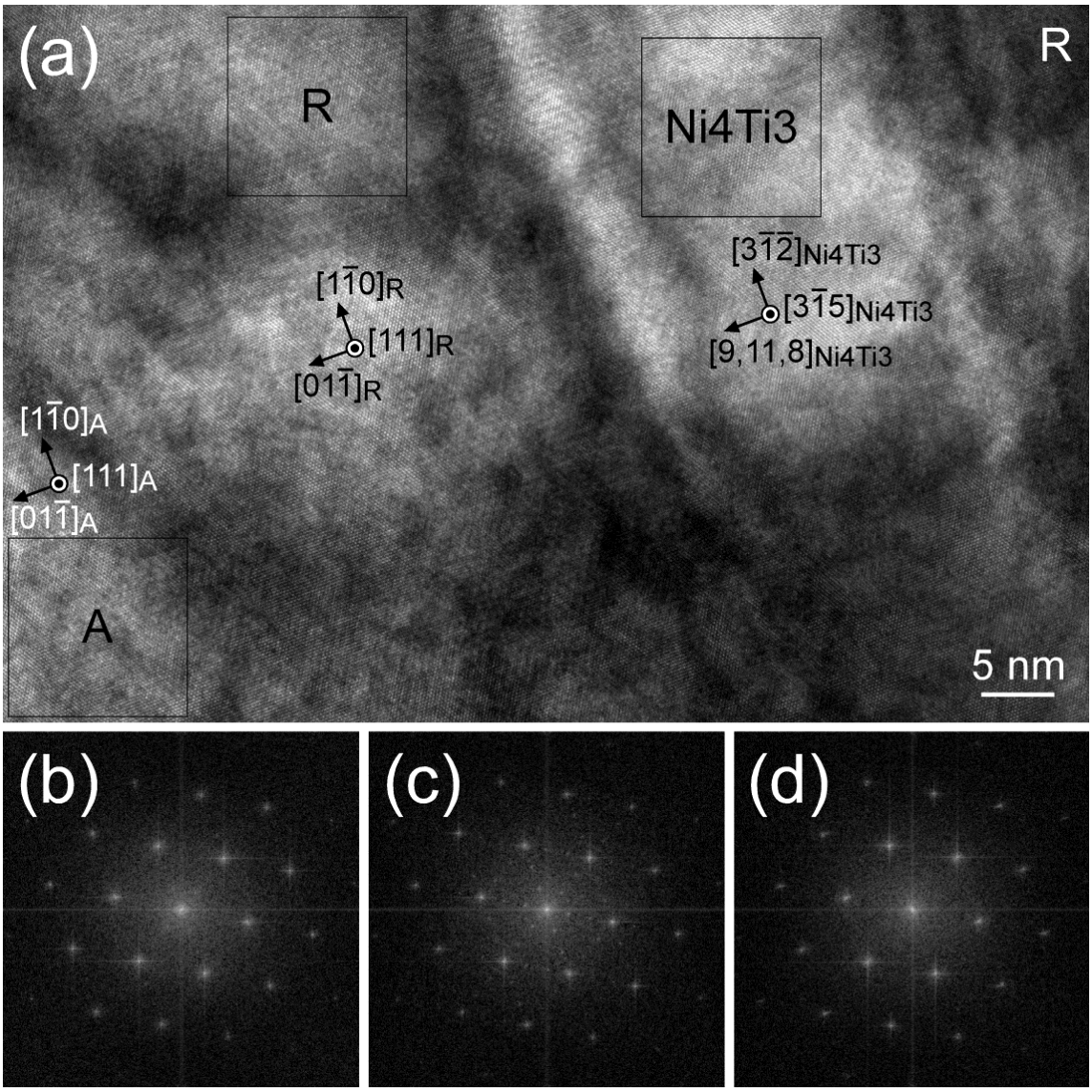


**Figure 6.13 (a)** HRTEM micrograph of the aged specimen deformed by thermal cycling under stress (see Figure 6.8) and **(b, c and d)** FFTs obtained from the framed areas A, R and Ni4Ti3 in (a), respectively. Symbols A, R and Ni4Ti3 indicate B2 austenite, R-phase and $Ni_4Ti_3$ precipitate, respectively.

Figure 6.13 shows the HRTEM images of the aged specimen deformed by thermal cycling under stress (see Figure 6.8) obtained along the compression axis of $[111]_{B2}$. The crystal orientation of the austenite and $Ni_4Ti_3$ precipitate is same while the R-phase variant is different from that observed in Figure 6.3. The $[111]_R$ direction of the R-phase variant is parallel to the $[111]_{B2}$ compression axis and the variant is expected to produce a negative TWSME strain during B2-R transformation.

After B2-R transformation, the selected variants of R-phase will transform to specific B19′ martensite variants which will further increase the negative TWSME strain. It has been reported that the $[10\bar{1}]_{B19'}$ is derived from $<111>_{B2}$ and is the most expansible direction during the B2-B19′ transformation [129]. In the specimen deformed in austenite, $[10\bar{1}]_{B19'}$ martensite variants were observed along the compression axis of $[111]_{B2}$ (Figure 6.11d). Therefore, it is concluded that $[111]_{B2}$ austenite is transformed to $[111]_R$ R-phase variants first and then transformed to $[10\bar{1}]_{B19'}$ martensite variants during the two-stage (B2-R-B19′) transformation. As a result, two-stage negative TWSME strains are produced as shown in Figures 6.7 and 6.8.

### 6.2.10 Generation of TWSME

As a summary, the schematics for TWSME creation of solution-treated and aged samples after compression tests were illustrated in Figure 6.14. First, single crystals were compressed either at a low temperature below $M_f$ or at a high temperature above $M_d$, and then they were unloaded. The dislocations were aligned on specific crystal planes when they were formed in martensite, while the deformation in austenite did not cause the alignment of dislocations on certain planes. After heating above $A_f$, the dislocation structure formed in martensite was elongated by the shape recovery of the specimen and produces the spring-back force. Then, the specimens were cooled down below $M_f$ and heated above $A_f$ to obtain TWSME. The positive (compressive) TWSME was observed in the specimen deformed in martensite since the spring-back force selected specific martensite variants which produced the contraction of the specimen, while the dislocations formed in the specimen deformed in austenite did not produce TWSME.

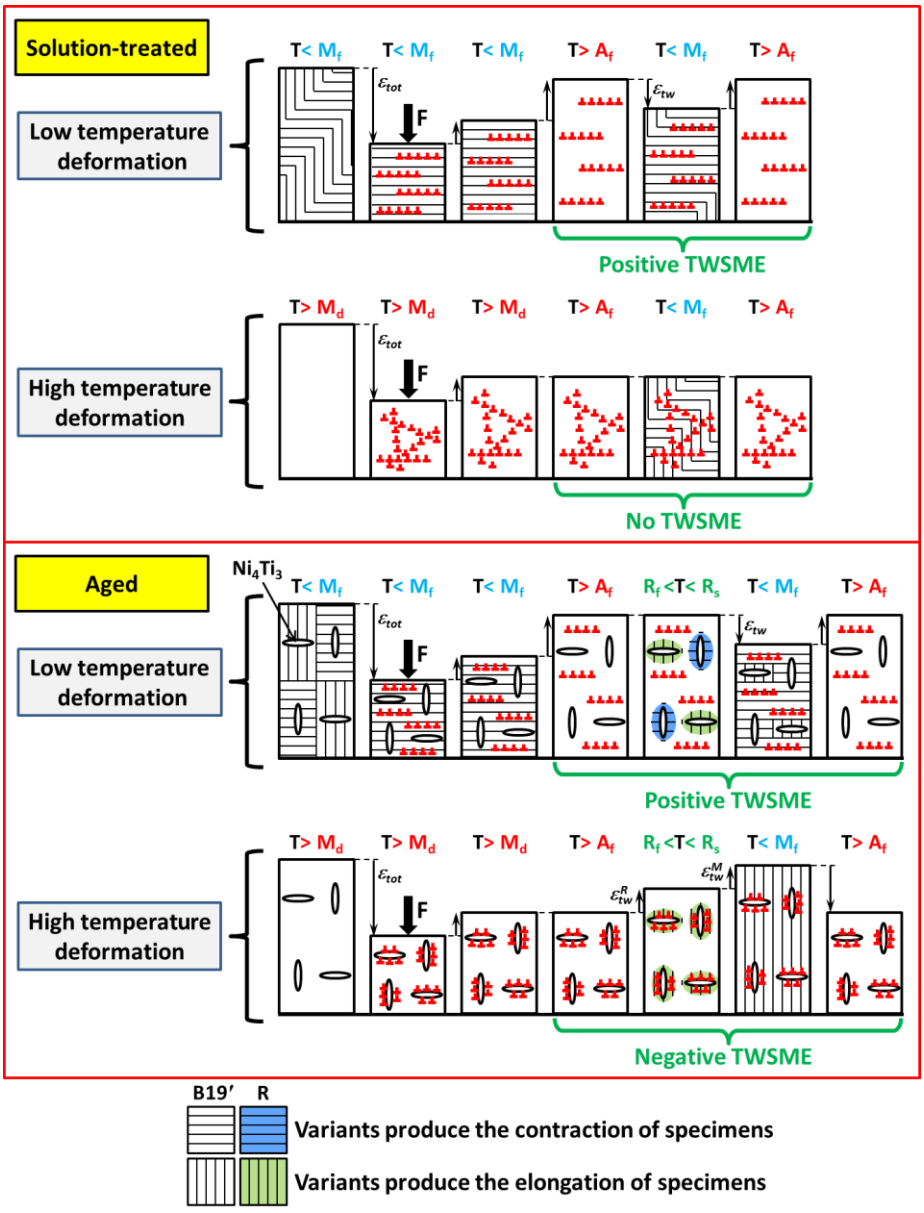


**Figure 6.14** Schematic illustration of generation of TWSME.

Figure 6.14 also shows the schematics for the generation of TWSME in the aged specimens. The test specimens were loaded and unloaded at a low temperature below $M_f$ or at a high temperature above $M_d$. The dislocations were observed between the precipitates when the specimen was deformed in martensite. On the other hand, the

dislocations introduced in austenite were observed around the precipitates. Similar to the solution-treated specimens, the dislocation structures formed in martensite were elongated after heating above $A_f$ and produced the spring-back force, while the specimen deformed in austenite did not show a shape change at above $A_f$. In order to obtain TWSME, the specimens were cooled down below $M_f$ and heated above $A_f$. If the sample was deformed in martensite, the dislocations did not affect the R-phase transformation considerably since they did not alter the stress fields around the precipitates while the spring-back forces caused the contraction of the specimen during B19′ martensite transformation, resulting in positive (compressive) TWSME similar to the solution-treated specimen. On the other hand, in the aged specimen deformed in austenite, the dislocation formation around the precipitates resulted in the back stress along the compressive direction. This stress field resulted in selections the specific variants of R-phase and B19′ martensite which led to the observation of the negative (tensile) TWSME upon the two-stage (B2-R-B19′) transformation.

The $\varepsilon_{tw}$ of aged SMAs are summarized in Figure 6.15 as a function of applied compressive total strain. Initially, thermal cycling test under 5 MPa applied stress was conducted for the as-aged $Ni_{51}Ti_{49}$ single crystals, and compressive $\varepsilon_{tw}$ of 0.4% was obtained. For the aged sample deformed at 200 °C, tensile $\varepsilon_{tw}$ shows a linearly increasing trend with increasing strain up to 6% of compressive strain and tends to saturate with further deformation. When the aged sample is deformed at -80 °C, increasing the applied compressive strain from 4% to 7% elevated the compressive $\varepsilon_{tw}$ from 0.5% to 0.7%. For the aged sample deformed at 60 °C, tensile $\varepsilon_{tw}$ increases with increasing strain up to compressive strain of 7%. As shown in Figure 6.15, the tensile $\varepsilon_{tw}$ decreases with further

deformation since the formation of the internal stresses is disturbed by the excessive introduction of dislocation [148]. A maximum two-way shape memory strain of 1.9% was obtained after 6% deformation of at 200 °C in the aged [111] oriented $Ni_{51}Ti_{49}$ single crystals.

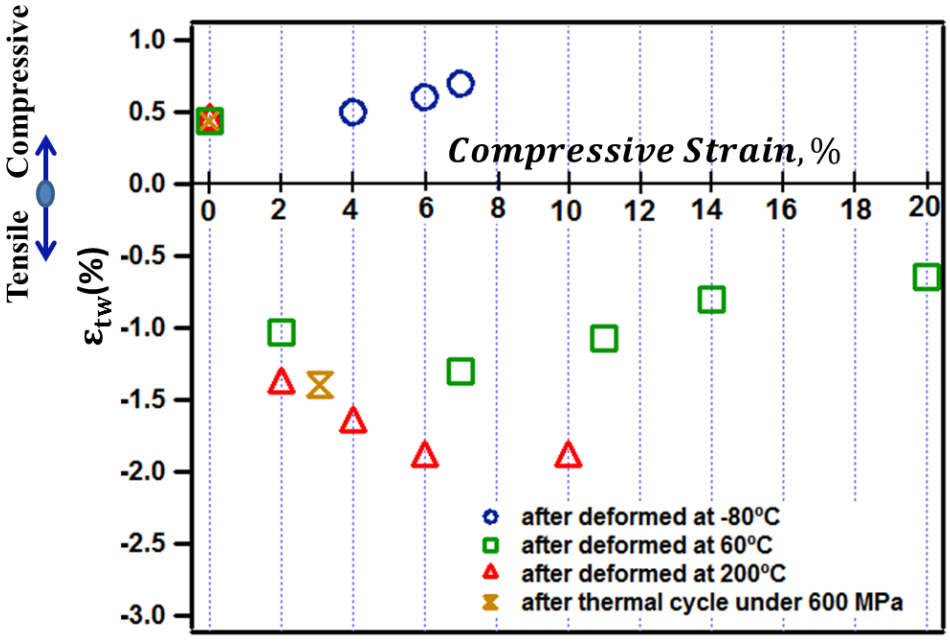


**Figure 6.15** $\varepsilon_{tw}$ as a function of applied strain for aged SMAs.

## 6.3 The effects of stress-assisted aging on the two-way shape memory behavior of [111]-oriented NiTi single crystal

The single crystal samples were grown by the Bridgman method in an inert gas atmosphere. The as-grown $Ni_{51}Ti_{49}$ single crystals were solution annealed at 1000℃ for 2 hours in Argon filled quartz ampoules and water quenched. Then, the crystals are aged at 500°C for 1.5 hours under an external compressive stress of 150 MPa applied along the [111] direction.

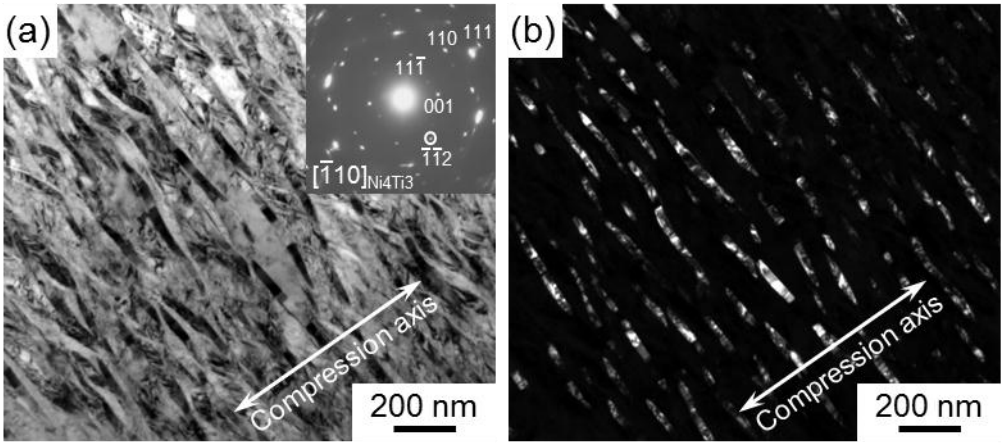


**Figure 6.16 (a)** Bright field image and the corresponding SAD pattern for the $Ni_{51}Ti_{49}$ single crystal aged at 500 °C for 1.5 hours under a compressive stress of 150 MPa. **(b)** Dark field image was taken using the $\bar{1}\bar{1}2_{Ni4Ti3}$ reflection circled in the SAD pattern in (a).

Figure 6.16a shows the bright field micrograph and the corresponding selected area diffraction (SAD) pattern obtained at room temperature for the $Ni_{51}Ti_{49}$ single crystal after stress-assisted aging. The SAD pattern was taken along the $[\bar{1}10]_{Ni4Ti3}$ zone axis and some reflections from $Ni_4Ti_3$ precipitates were indexed. In the dark field image (Figure 6.16b) taken by using the diffraction spot circled in the SAD pattern, a single family with two crystallographically equivalent variants of $Ni_4Ti_3$ precipitates was

observed on the $(111)_{B2}$ plane perpendicular to the $[111]_{B2}$ compression direction. It should be noted that the matrix in Figure 6.16 is a single B19′ martensite phase which is considered to be formed thermally during electropolishing process at -15 °C.

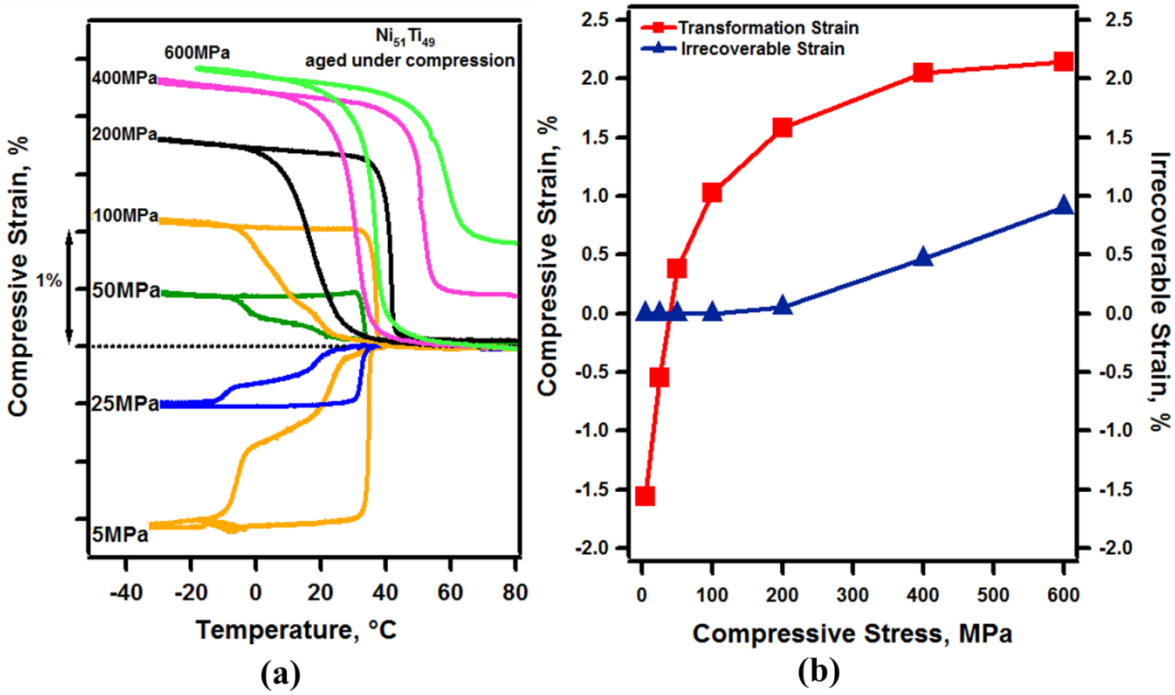


**Figure 6.17 (a)** Thermal cycling under selected constant compressive stresses, **(b)** transformation and irrecoverable strains as a function of applied stress for the [111] oriented $Ni_{51}Ti_{49}$ single crystal aged at 500 °C for 1.5 hours under a compressive stress of 150 MPa.

Figure 6.17 shows the thermal cycling under constant compressive stress responses of [111]-oriented $Ni_{51}Ti_{49}$ single crystal after a stress-assisted aging. The specimen was loaded in the austenite phase to selected stress levels, and then cooled down below the martensite finish temperature and heated above the austenite finish temperature. Multiple thermal cycling tests were performed at selected compressive stress levels ranging from 5 MPa to 600 MPa. During thermal cycling, two-stage (B2- R-

B19') transformation behavior was observed on cooling under low stress levels. At high stress levels, since the austenite to R-phase transformation temperatures are almost stress independent while austenite to B19' martensite transformation temperatures are highly stress dependent, B19' martensite transformation temperatures increase above R-phase transformation temperatures and R-phase transformation disappears [124].

The thermal cycling under 5 MPa is accepted as the TWSME behavior where a negative (tensile) TWSME strain ($\varepsilon_{tw}$) of 1.56% was observed. When the stress is increased to 25 MPa, the negative (tensile) transformation strain is decreased to 0.54% and 50 MPa is needed to suppress the observation of tensile strain. For stress levels above 50 MPa, the compressive transformation strain increases with stress. While the transformation strain is negative (tensile) (-1.56%) under 5 MPa, it is positive (compressive) (2.15%) under 600 MPa.

In Figure 6.17, it is clear that TTs increase with stress. $M_s$ and $A_f$ were -7 °C and 31 °C under 25 MPa while they were increased to 39 °C and 64 °C under 600 MPa, respectively. The irrecoverable strain was calculated by taking the difference between the strain values of cooling and heating curves at 70 °C. The irrecoverable strain was 0.05%, 0.46% and 0.9 under 200 MPa, 400 MPa and 600 MPa, respectively.

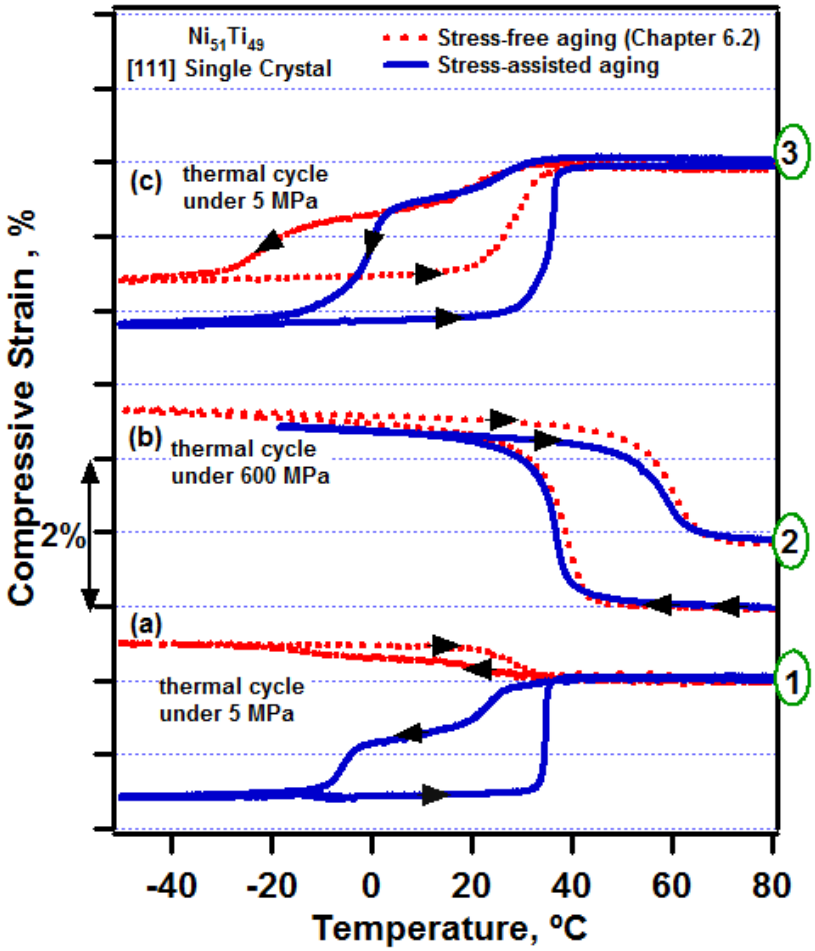


**Figure 6.18 (a)** TWSME, **(b)** thermal cycling under 600 MPa and **(c)** TWSME after thermal cycling under 600 MPa of stress-free and stress-assisted aged [111]-oriented $Ni_{51}Ti_{49}$ single crystals**.**

Figure 6.18(a) shows the thermal cycling responses of stress-free and stress-assisted aged $Ni_{51}Ti_{49}$ single crystal alloys under 5 MPa. The initial TWSME strain after stress-free aging was 0.4 %. On the other hand, when the sample is aged under stress, the precipitates are aligned and negative (tensile) TWSME strain of 1.56% was observed.

Figure 6.18(b) shows the thermal cycling responses under 600 MPa applied stress of aged [111]-oriented $Ni_{51}Ti_{49}$ single crystals. It is clear that responses are similar in both cases where recoverable strain of 1.5% and irrecoverable strain of 0.9% were observed. Figure 6.18(c) shows the subsequent TWSME responses of stress-free and stress-assisted aged $Ni_{51}Ti_{49}$ single crystal after thermal cycling under 600 MPa (Figure 6.18(b)). Negative (tensile) TWSME strain of 1.4% was obtained after thermal cycling under 600 MPa in the stress-free aged sample. The negative TWSME strain in the stress-assisted aged sample was increased after thermal cycling under 600MPa, where a large negative TWSME strain of 2.2% was obtained. It should be noted that while the

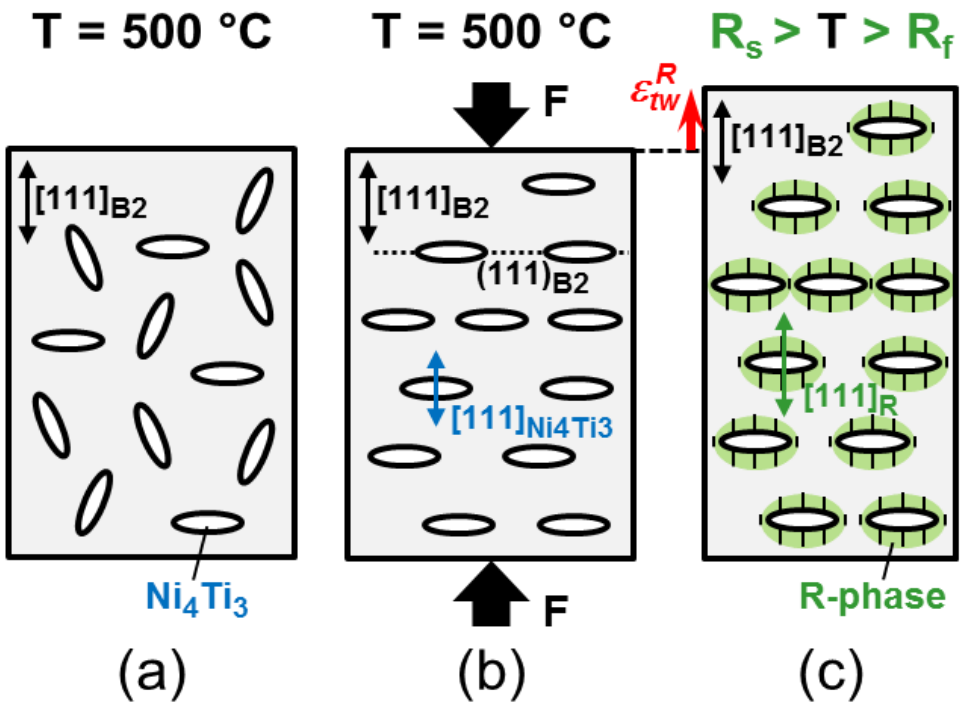


**Figure 6.19** Schematic illustrations of the formation of $Ni_4Ti_3$ precipitates in Ni-Ti SMAs after aging **(a)** in stress-free condition and **(b)** under compressive stress. **(c)** A schematic for the generation of negative (tensile) TWSME due to R-phase transformation after stress-assisted aging.

transformation strain is 2.14% compressive at 600 MPa, the subsequent TWSME strain is 2.2% tensile for the samples that are aged under stress.

The effects of aging and external stress on the formation of $Ni_4Ti_3$ precipitates were schematically illustrated in Figure 6.19. While stress-free aging produces four families of $Ni_4Ti_3$ precipitates on the four $\{111\}_{B2}$ planes (Figure 6.19a), a compressive stress applied along the $[111]_{B2}$ direction during aging results in one family of $Ni_4Ti_3$ precipitates on the $(111)_{B2}$ plane (Figure 6.19b). It has been reported that $Ni_3Ti_4$ precipitates shrink along the $[111]_{Ni4Ti3}$ (// $<111>_{B2}$) direction upon formation from the austenite matrix and creates tensile stress in the matrix along the $[111]_{Ni4Ti3}$ (// $<111>_{B2}$) direction [61, 129].

The tensile stress created in the matrix around $Ni_4Ti_3$ precipitates selects the specific R-phase and B19′ martensite variants. The orientation relationships between the $Ni_4Ti_3$ precipitate and R-phase and between the $Ni_4Ti_3$ precipitate and B19′ martensite were reported as $[111]_{Ni4Ti3}$ // $[111]_R$ and $[111]_{Ni4Ti3}$ // $[10\bar{1}]_{B19'}$, respectively [129]. In Chapter 6.2, the $[111]_{Ni4Ti3}$ // $[111]_R$ relationship has been confirmed in $Ni_{51}Ti_{49}$ single crystals after stress-free aging. The $[111]_R$ and $[10\bar{1}]_{B19'}$ directions are derived from $<111>_{B2}$ directions and they are the most expansible directions during the transformations from austenite. Therefore, the tensile stress along the $<111>_{B2}$ directions in the austenite matrix created by $Ni_4Ti_3$ precipitates facilitates the formation of $[111]_R$ R-phase variants and $[10\bar{1}]_{B19'}$ martensite variants.

Figure 6.19c shows the schematic for negative (tensile) TWSME creation due to R-phase transformation after stress-assisted aging. Since the specimen has only one family of $Ni_4Ti_3$ precipitates, the $[111]_R$ R-phase variants are selected and they elongate

the specimen along the $[111]_{B2}$ compression direction, resulting in negative (tensile) TWSME. After the R-phase transformation, the $[10\bar{1}]_{B19'}$ martensite variants are selected during the subsequent B19′ martensite transformation, which results in further increase in negative TWSME strain and two-stage behavior, as shown in Figure 6.17.

The negative TWSME strain of the samples that are aged under stress was increased after thermal cycling under 600MPa (Figure 6.18). It was previously reported that in stress-free aged specimens that dislocations introduced during thermal cycling under compressive stress accumulate around $Ni_4Ti_3$ precipitates and create back stresses along the external compression direction. The back stresses resulted in further selection of the $[111]_R$ and $[10\bar{1}]_{B19'}$ variants. Thus, the increase of the negative TWSME strain in the stress-assisted aged specimen can be attributed to the creation of back stresses by dislocations around $Ni_4Ti_3$ precipitates that facilitates the selection of the $[10\bar{1}]_{B19'}$ martensite variants.

## 6.4 Conclusion

Firstly, the two-way shape memory effect responses of Ni-rich [111]-oriented $Ni_{51}Ti_{49}$ single crystals are investigated under compression. Effects of aging and deformation temperature on TWSME were revealed and the corresponding microstructure was investigated. The important results are summarized below,

(1) The solution-treated single crystals did not show TWSME in the as-solution-treated condition and after deformation in austenite. On the other hand, positive (compressive) TWSME was observed when they are deformed in martensite or by thermally cycled under stress.

(2) The stress-free aged single crystals deformed in martensite showed positive TWSME. However, the stress-free aged specimens deformed in austenite and by the thermal cycling under stress showed negative (tensile) TWSME.

(3) The dislocations introduced in martensite phase are aligned on specific crystal planes and the stress fields around the dislocations cause the selection of martensite variants which results in the positive TWSME. TEM investigation revealed that the martensite variants observed in the stress-free aged specimen deformed in martensite were mainly CV1, CV1′, CV3, CV3′, CV5 and CV5′ which results in the contraction of the specimen, corresponding to the positive TWSME.

(4) The negative TWSME was only confirmed in aged specimens. It was proposed that the back stresses created by the dislocation formation around $Ni_4Ti_3$ precipitates results in the selection of the specific variants of R-phase and B19′ martensite which produce negative strain. TEM investigation confirmed that the martensite variants observed in the stress-free aged specimen deformed in austenite were mainly CV2, CV4 and CV6 which correspond to the negative TWSME.

(5) The two-way shape memory strain initially increases with increasing deformation strain and decreases with excessive introduced dislocations. A maximum two-way shape memory strain of 1.9% was obtained after 6% deformation of at 200 °C in the stress-free aged specimen.

Secondly, the effects of stress-assisted aging on the TWSME behavior of $Ni_{51}Ti_{49}$ single crystal along the [111] orientation were investigated. Single family of $Ni_4Ti_3$ particles was formed after aging at 500°C under an applied compressive stress of 150 MPa along the [111] direction. The important results are summarized below,

(1) Since a single family of $Ni_4Ti_3$ precipitates was formed, the $[111]_R$ and $[10\bar{1}]_{B19'}$ variants are formed due to the aligned stress fields along the precipitates to elongate the specimen along the $[111]_{B2}$ compression direction and result in negative (tensile) TWSME during cooling.

(2) The negative TWSME strain was increased after thermal cycling under constant stress.

(3) The maximum TWSME strain was observed to be negative (tensile) of 2.2% after thermal cycling training under 600 MPa compressive stress with the 2.15% transformation strain.

# 7 Conclusion

Nickel rich NiTi shape memory alloys have been widely used for bio-medical, electrical and mechanical applications due to their distinct superelasticity and shape memory properties as compared to near equi-atomic NiTi SMAs. In this study, shape memory properties and phase transformation behavior of high Ni-rich $Ni_{54}Ti_{46}$ (at.%) polycrystalline and Ni-rich $Ni_{51}Ti_{49}$ (at.%) single-crystalline SMAs are determined. Conclusions are summarized below.

1- High Ni-rich $Ni_{54}Ti_{46}$ (at.%) polycrystalline alloys

The effects of aging on the phase transformation behavior and mechanical properties of a Ni-rich $Ni_{54}Ti_{46}$ are investigated. Samples were homogenized at 1000°C, followed by heat treatment in the temperature range from 450°C to 600°C. Phase transformation was investigated in aged $Ni_{54}Ti_{46}$ SMA with differential scanning calorimetry, X-ray diffraction and transmission electron microscopy to observe the influence of precipitates and R-phase on the phase transformation. Additionally, their hardness was measured as a function of both aging time and temperature.

- The multi-step transformations are observed after heat treatments due to precipitation formation.
- Depending on aging heat treatments, transformation strain of 2-3% can be obtained in SE and SM.
- Applied stress and operation temperature considerably affect the transformation strain and hysteresis, and also alters the transformation sequence in these SMAs.

- Stress independent R-phase transformation was found to be responsible for the change in shape memory behavior with stress.
- High Ni-rich NiTi alloys has the ability exhibit perfect shape memory effect under high stress levels of 1 GPa and perfect superelasticity when up to 2 GPa was applied after selected heat treatments in compression.
- The shape memory behavior of $Ni_{54}Ti_{46}$ alloys was investigated under compression and it has been shown that they have a low transformation strain but very high strength, narrow temperature hysteresis (10°C) and dramatic change in shape memory behavior with stress.
- $Ni_{54}Ti_{46}$ alloy has the ability to exhibit perfect superelasticity was observed under high stress levels (~2 GPa) with reversible strain of 4%.
- The fine and homogeneously distributed $Ni_4Ti_3$ precipitates are observed. The volume fraction of the $Ni_4Ti_3$ precipitates was ~55% for 500°C aged specimen and ~43% for 550°C aged specimen.
- Precipitation formation is found to be an effective method to improve the strength of the material and also control the shape memory properties.
- It was revealed heat treatments could significantly alter the transformation temperatures and shape memory effects response.

2- Ni-rich $Ni_{51}Ti_{49}$ (at.%) single-crystalline alloys

The effects of aging and orientation on the shape memory and mechanical properties of $Ni_{51}Ti_{49}$ alloys are investigated. In addition, the effects of aging and

deformation on the two-way shape memory effect properties of single crystalline Ni-rich $Ni_{51}Ti_{49}$ alloys are revealed.

- R-phase transformation is observed after aging in all orientations.
- The shape memory behavior of $Ni_{51}Ti_{49}$ alloys was found to be highly orientation dependent. [001]-oriented $Ni_{51}Ti_{49}$ single crystals have high strength and show perfect superelasticity for a wide temperature range ($\Delta T$ = 140°C). Narrow temperature hysteresis of 10°C was observed under ultra high compressive stress level of 1500 MPa with 3.65% transformation strain in [001] orientation.
- When the samples were compressed in martensite state, positive (compressive) TWSME was observed. After compression above $M_d$, the homogenized samples did not show TWSME while the stress-free aged samples displayed negative (tensile) TWSME.
- TEM investigation revealed that compression in martensite and austenite phases results in different dislocation structures in the microstructure. Thus, the stress fields around the precipitates and dislocations form dissimilar martensite variants that results in the positive and negative TWSME strains. Since R-phase formation is highly stress dependent, small changes in the internal stress fields affect the selection of R-phase variants and thus, the martensite variants.
- A maximum negative (tensile) TWSME strain of 1.9% was obtained in the stress-free aged sample after 6% compression at 200 °C.

- The negative TWSME strain in the stress-assisted aged sample was increased after thermal cycling under 600 MPa, where a large negative TWSME strain of 2.2% was obtained. It should be noted that while the transformation strain is 2.14% compressive at 600 MPa, the maximum TWSME strain is 2.2% tensile after training for stress-assisted aged sample.

## References

[1] S.A. Shabalovskaya, Bio-Medical Materials and Engineering, 12 (2002) 69-109.

[2] A.A. Khamei, K. Dehghani, Materials Chemistry and Physics, 123 (2010) 269-277.

[3] Julien GJ (2002) Manufacturing of Nitinol parts and forms, U. S. Patent 6422010

[4] Julien GJ (2002) Manufacturing of Nitinol parts and forms, U. S. Patent 6422010

[5] Y. Motemani, M. Nili-Ahmadabadi, M.J. Tan, M. Bornapour, S. Rayagan, Journal of Alloys and Compounds, 469 (2009) 164-168.

[6] M. Nishida, C. Wayman, T. Honma, Metallurgical and Materials Transactions A, 17 (1986) 1505-1515.

[7] M. Nishida, C. Wayman, T. Honma, MTA, 17 (1986) 1505-1515.

[8] J.I. Kim, Y. Liu, S. Miyazaki, Acta Materialia, 52 (2004) 487-499.

[9] A.R. Pelton, J. Dicello, S. Miyazaki, Minimally Invasive Therapy & Allied Technologies, 9 (2000) 107-118.

[10] K. Mahesh, K., F. Braz Fernandes, M., R. Silva, J.C., (2009) 05014.

[11] D.J. Clingman, F.T. Calkins, J.P. Smith, 2003, pp. 219-229.

[12] G.J. Julien, Google Patents, 2002.

[13] G.J. Julien, Google Patents, 2006.

[14] K. Dehghani, A. Khamei, Materials Science and Engineering: A, 527 (2010) 684-690.

[15] F. Jiang, Y. Liu, H. Yang, L. Li, Y. Zheng, Acta Materialia, 57 (2009) 4773-4781.

[16] W. Yuan, S. Yi, Materials Science and Engineering: A, 271 (1999) 439-448.

[17] H. Horikawa, S. Ichinose, K. Morii, S. Miyazaki, K. Otsuka, MTA, 19 (1988) 915-923.

[18] S. Miyazaki, S. Kimura, K. Otsuka, Y. Suzuki, Scripta Metallurgica, 18 (1984) 883-888.

[19] T. Buchheit, J. Wert, Metallurgical and Materials Transactions A, 27 (1996) 269-279.

[20] S.C. Weighardt, H.J. Maier, Y.I. Chumlyakov, Journal of Alloys and Compounds.

[21] H. Sehitoglu, I. Karaman, R. Anderson, X. Zhang, K. Gall, H. Maier, Y. Chumlyakov, Acta Materialia, 48 (2000) 3311-3326.

[22] H. Sehitoglu, X. Zhang, J. Jun, I. Karaman, K. Gall, Y. Chumlyakov, ICF10, Honolulu (USA) 2001, 2013.

[23] K. Wada, Y. Liu, Materials Science and Engineering: A, 481–482 (2008) 166-169.

[24] Z. Wang, X. Zu, X. Feng, J. Dai, Materials Letters, 54 (2002) 55-61.

[25] M. Nishida, C.M. Wayman, R. Kainuma, T. Honma, Scripta Metallurgica, 20 (1986) 899-904.

[26] M.S. Shakeri, J. Khalil-Allafi, V. Abbasi-Chianeh, A. Ghabchi, Journal of Alloys and Compounds, 485 (2009) 320-323.

[27] A. Gyobu, Y. Kawamura, H. Horikawa, T. Saburi, Materials Science and Engineering: A, 273 (1999) 749-753.

[28] M. Nishida, T. Honma, Scripta Metallurgica, 18 (1984) 1293-1298.

[29] K. Enami, A. Nagasawa, S. Nenno, Scripta Metallurgica, 9 (1975) 941-948.

[30] Y.I. Chumlyakov, E.Y. Panchenko, V.B. Aksenov, I.V. Kireeva, M.P. Kuksa, I. Karaman, H. Sehitoglu, J. Phys. IV France, 115 (2004) 21-28.

[31] J.-F. Li, Z.-Q. Zheng, X.-W. Li, Z.-W. Peng, Materials & Design, 30 (2009) 314-318.

[32] J. Michutta, M. Carroll, A. Yawny, C. Somsen, K. Neuking, G. Eggeler, Materials Science and Engineering: A, 378 (2004) 152-156.

[33] V.N. Khachin, V.E. Gyunter, D.B. Chernov, Physics of Metals and Metallography, 42 (1976) 186-189.

[34] E.P. Ryklina, I.Y. Khmelevskaya, S.D. Prokoshkin, K.E. Inaekyan, R.V. Ipatkin, Materials Science and Engineering: A, 438–440 (2006) 1093-1096.

[35] A. Ölander, Journal of the American Chemical Society, 54 (1932) 3819-3833.

[36] L.C. Chang, T.A. Read, Trans. Met. Soc. AIME, 189 (1951) 47.

[37] D.C. Lagoudas, Shape memory alloys: modeling and engineering applications, Springer, 2008.

[38] Buehler, W. J.,letter to Amy Axt Hanson, 15 June 1991.

[39] I.A. Arbuzova, L.G. Khandros, Fiz. Met. Metall., 17 (1964) 390.

[40] Hanson, A. A. Technology Review 1991, 94(4), 26.

[41] F.E. Wang, W.J. Buehler, S.J. Pickart, Journal of Applied Physics, 36 (1965) 3232-3239.

[42] F.E. Wang, B.F. DeSavage, W.J. Buehler, W.R. Hosler, Journal of Applied Physics, 39 (1968) 2166-2175.

[43] P.K. Kumar, D.C. Lagoudas, Introduction to Shape Memory Alloys, Shape Memory Alloys, Springer US, 2008, pp. 1-51.

[44] F. Laves, H. Wallbaum, Naturwissenschaften, 27 (1939) 674-675.

[45] W.J. Buehler, F.E. Wang, Ocean Engineering, 1 (1968) 105-120.

[46] A.A. Khamei, K. Dehghani, Journal of Alloys and Compounds, 490 (2010) 377-381.

[47] S. Miyazaki, K. Otsuka, Metallurgical and Materials Transactions A, 17 (1986) 53-63.

[48] Laves F, Wallbaum HJ. Naturwissenschaften 1939;27:674.

[49] Duwez P, Taylor JL. Trans AIME 1950;188:1173.

[50] Margolin H, Ence E, Nielsen JP. J Metals (Trans AIME) 1953(February):243.

[51] G.R. Purdy , J.G. Parr JG. Trans AIME 1961;221:636.

[52] D.M. Poole, W. Hume-Rothery, J. Inst. Met., 83 (1954–1955), p. 473

[53] Wasilewski RJ, Butler SR, Hanlon JE, Worden D. Metall Trans 1971;2:229.

[54] Massalski TB, Okamoto H, Subramanian PR, Kacprzak L, editors. Binary alloy phase diagrams, 2nd edition, vol. 3. Materials Park, OH: ASM International; 1990. p. 2874.

[55] K. Otsuka, X. Ren, Progress in materials science, 50 (2005) 511-678.

[56] Nishida M, Wayman CM, Honma T. Metall Trans 1986;17A:1505.

[57] Kainuma R, Matsumoto M, Honma T. Bull Inst Mineral Dressing and Metall, Tohoku Univ (SENKEN IHO) 1987;43:149. [inJapan ese].

[58] W. Tang, Metallurgical and Materials Transactions A, 28 (1997) 537-544.

[59] R.R. Adharapurapu, K.S. Vecchio, Exp Mech, 47 (2007) 365-371.

[60] J. Michutta, C. Somsen, A. Yawny, A. Dlouhy, G. Eggeler, Acta Materialia, 54 (2006) 3525-3542.

[61] T. Tadaki, Y. Nakata, K.i. Shimizu, K. Otsuka, Trans. Jpn. Inst. Met., 27 (1986) 731-740.

[62] J. Michutta, M.C. Carroll, A. Yawny, C. Somsen, K. Neuking, G. Eggeler, Materials Science and Engineering A, 378 (2004) 152-156.

[63] L. Bataillard, J.-E. Bidaux, R. Gotthardt, Philosophical magazine A, 78 (1998) 327-344.

[64] W. Tirry, D. Schryvers, Acta materialia, 53 (2005) 1041-1049.

[65] D. Li, L. Chen, Acta materialia, 45 (1997) 2435-2442.

[66] O. Bojda, G. Eggeler, A. Dlouhý, Scripta materialia, 53 (2005) 99-104.

[67] J. Khalil-Allafi, G. Eggeler, A. Dlouhy, W.W. Schmahl, C. Somsen, Materials Science and Engineering A, 378 (2004) 148-151.

[68] P. Filip, K. Mazanec, Scripta materialia, 45 (2001) 701-707.

[69] J. Khalil-Allafi, A. Dlouhy, G. Eggeler, Acta Materialia, 50 (2002) 4255-4274.

[70] K. Gall, H. Maier, Acta Materialia, 50 (2002) 4643-4657.

[71] C. Efstathiou, H. Sehitoglu, Scripta Materialia, 59 (2008) 1263-1266.

[72] T.E. Buchheit, J.A. Wert, Metallurgical and Materials Transactions A, 25 (1994) 2383-2389.

[73] Y. Motemani, M. Nili-Ahmadabadi, M. Tan, M. Bornapour, S. Rayagan, Journal of Alloys and Compounds, 469 (2009) 164-168.

[74] Y.-q. ZHANG, S.-y. JIANG, Y.-n. ZHAO, M. TANG, Transactions of Nonferrous Metals Society of China, 22 (2012) 2685-2690.

[75] R. Adharapurapu, K. Vecchio, Exp Mech, 47 (2007) 365-371.

[76] A. Dlouhý, O. Bojda, C. Somsen, G. Eggeler, Materials Science and Engineering: A, 481 (2008) 409-413.

[77] J. Kim, Y. Liu, S. Miyazaki, Acta Materialia, 52 (2004) 487-499.

[78] A.J.W. Johnson, R.F. Hamilton, H. Sehitoglu, G. Biallas, H.J. Maier, Y.I. Chumlyakov, H.S. Woo, Metallurgical and Materials Transactions A: Physical Metallurgy and Materials Science, 36 (2005) 919-928.

[79] P. Šittner, P. Lukáš, V. Novák, M.R. Daymond, G.M. Swallowe, Materials Science and Engineering: A, 378 (2004) 97-104.

[80] S. Miyazaki, K. Otsuka, Metallurgical and Materials Transactions A, 17 (1986) 53-63.

[81] S. Miyazaki, K. Otsuka, Philosophical Magazine A, 50 (1985) 393-408.

[82] H. Morawiec, Strószlig, D., T. Goryczka, D. Chrobak, Scripta Materialia, 35 (1996) 485-490.

[83] Q. Chen, X.F. Wu, T. Ko, Scripta Metallurgica et Materialia, 29 (1993) 49-53.

[84] P. Šittner, M. Landa, P. Lukáš, V. Novák, Mechanics of Materials, 38 (2006) 475-492.

[85] X. Zhang, H. Sehitoglu, Materials Science and Engineering A, 374 (2004) 292-302.

[86] T. Fukuda, A. Deguchi, T. Kakeshita, T. Saburi, Materials Transactions, JIM, 38 (1997) 1057-1062.

[87] J. Khalil-Allafi, B. Amin-Ahmadi, Journal of Materials Science, 45 (2010) 6440-6445.

[88] J. Perkins, R. Sponholz, MTA, 15 (1984) 313-321.

[89] L. Contardo, G. Guénin, Acta Metallurgica et Materialia, 38 (1990) 1267-1272.

[90] Y. Liu, P.G. McCormick, Acta Metallurgica et Materialia, 38 (1990) 1321-1326.

[91] R. Stalmans, J. Van Humbeeck, L. Delaey, Acta Metallurgica et Materialia, 40 (1992) 501-511.

[92] J. Perkins, R.O. Sponholz, MTA, 15 (1984) 313-321.

[93] A. Nagasawa, K. Enami, Y. Ishino, Y. Abe, S. Nenno, Scripta Metallurgica, 8 (1974) 1055-1060.

[94] E. Cingolani, M. Ahlers, M. Sade, Acta Metallurgica et Materialia, 43 (1995) 2451-2461.

[95] R. Stalmans, J. Van Humbeeck, L. Delaey, Acta Metallurgica et Materialia, 40 (1992) 2921-2931.

[96] J. Perkins, Scripta Metallurgica, 8 (1974) 1469-1476.

[97] K. Wada, Y. Liu, Journal of Alloys and Compounds, 449 (2008) 125-128.

[98] E. Cingolani, M. Ahlers, Materials Science and Engineering: A, 273–275 (1999) 595-599.

[99] Z. Wang, X. Zu, J. Dai, P. Fu, X. Feng, Materials Letters, 57 (2003) 1501-1507.

[100] M.J. Bigeon, M. Morin, Scripta Mater. 35 (1996) 1373.

[101] E. Cingolani, M. Ahlers, Mater. Sci. Eng. A 273–275 (1999) 595.

[102] P.G. McCormick, Y. Liu, Acta Metall. Mater. 42 (1994) 2407.

[103] A. Dlouhy, J. Khalil-Allafi, G. Eggeler, Philosophical Magazine, 83 (2003) 339-363.

[104] J. Khalil-Allafi, G. Eggeler, W.W. Schmahl, D. Sheptyakov, Materials Science and Engineering: A, 438–440 (2006) 593-596.

[105] G. Fan, W. Chen, S. Yang, J. Zhu, X. Ren, K. Otsuka, Acta Materialia, 52 (2004) 4351-4362.

[106] J. Michutta, C. Somsen, A. Yawny, A. Dlouhy, G. Eggeler, Acta materialia, 54 (2006) 3525-3542.

[107] M. Paryab, A. Nasr, O. Bayat, V. Abouei, A. Eshraghi, Metalurgija, 16 (2010) 123-131.

[108] T. Duerig, A. Pelton, D. Stöckel, Materials Science and Engineering: A, 273–275 (1999) 149-160.

[109] H.E. Karaca, I. Kaya, H. Tobe, B. Basaran, M. Nagasako, R. Kainuma, Y. Chumlyakov, Materials Science and Engineering: A, 580 (2013) 66-70.

[110] M. Nishida, C. Wayman, A. Chiba, Metallography, 21 (1988) 275-291.

[111] R. Hamilton, H. Sehitoglu, Y. Chumlyakov, H. Maier, Acta Materialia, 52 (2004) 3383-3402.

[112] K.N. Melton, O. Mercier, Acta Metallurgica, 29 (1981) 393-398.

[113] K. Melton, O. Mercier, Acta Metallurgica, 29 (1981) 393-398.

[114] D. Grummon, JOM, 55 (2003) 24-32.

[115] D. Dunne, C. Wayman, Metallurgical and Materials Transactions B, 4 (1973) 147-152.

[116] D. P. Dunne and C. M. Wayman, Metall. Trans. A, 1973, 4A, 137

[117] K. Gall, H. Sehitoglu, Y.I. Chumlyakov, I.V. Kireeva, Acta Materialia, 47 (1999) 1203-1217.

[118] Y. Sutou, N. Koeda, T. Omori, R. Kainuma, K. Ishida, Acta Materialia, 57 (2009) 5748-5758.

[119] L. Orgéas, D. Favier, Acta Materialia, 46 (1998) 5579-5591.

[120] C. Urbina, S. De la Flor, F. Ferrando, Materials Science and Engineering: A, 501 (2009) 197-206.

[121] J. Olbricht, A. Yawny, J. Pelegrina, A. Dlouhy, G. Eggeler, Metallurgical and Materials Transactions A, 42 (2011) 2556-2574.

[122] M. Nishida, C.M. Wayman, A. Chiba, Metallography, 21 (1988) 275-291.

[123] T. Waitz, V. Kazykhanov, H.P. Karnthaler, Acta Materialia, 52 (2004) 137-147.

[124] H. Karaca, I. Kaya, H. Tobe, B. Basaran, M. Nagasako, R. Kainuma, Y. Chumlyakov, Materials Science and Engineering: A, 580 (2013) 66-70.

[125] Y.I. Chumlyakov, I. Kireeva, E.Y. Panchenko, V. Aksenov, V. Kirillov, A. Ovsyannikov, E. Zakharova, H. Sehitogly, Russian physics journal, 46 (2003) 811-823.

[126] H. Sehitoglu, R. Hamilton, D. Canadinc, X. Zhang, K. Gall, I. Karaman, Y. Chumlyakov, H. Maier, Metallurgical and Materials Transactions A, 34 (2003) 5-13.

[127] S. Eucken, T.W. Duerig, Acta Metallurgica, 37 (1989) 2245-2252.

[128] A. Dlouhý, O. Bojda, C. Somsen, G. Eggeler, Materials Science and Engineering: A, 481–482 (2008) 409-413.

[129] R. Kainuma, M. Matsumoto, T. Honma, Proceedings of the International Conference on Martensitic Transformations. ICOMAT-86, 1986, pp. 717-722.

[130] O. Benafan, S.A. Padula, Ii, R.D. Noebe, T.A. Sisneros, R. Vaidyanathan, Journal of Applied Physics, 112 (2012) 093510-093511.

[131] Y. Liu, Y. Liu, J. Van Humbeeck, Acta Materialia, 47 (1998) 199-209.

[132] K. Wada, Y. Liu, Acta Materialia, 56 (2008) 3266-3277.

[133] R. Lahoz, L. Gracia-Villa, J.A. Puértolas, Journal of engineering materials and technology, 124 (2002) 397-401.

[134] Y.I. Yoo, J.J. Lee, Physics Procedia, 22 (2011) 449-454.

[135] H. Scherngell, A.C. Kneissl, Scripta Materialia, 39 (1998) 205-212.

[136] R. Lahoz, J.A. Puértolas, Journal of Alloys and Compounds, 381 (2004) 130-136.

[137] Miyazaki S, Kimura M. Amsterdam: Elsevier; 1994. p. 1101

[138] Y. Kudoh, M. Tokonami, S. Miyazaki, K. Otsuka, Acta Metallurgica, 33 (1985) 2049-2056.

[139] T. Ezaz, J. Wang, H. Sehitoglu, H.J. Maier, Acta Materialia, 61 (2013) 67-78.

[140] I.C. Yu, The Physics of Metals and Metallography, 89 (2000) 196-205.

[141] S. Miyazaki, K. Otsuka, C.M. Wayman, Acta Metallurgica, 37 (1989) 1873-1884.

[142] T. Saburi, S. Nenno, Solid to Solid Phase Transformations, (1981) 1455-1479.

[143] ] Philip TV, Beck PA. Trans AIME 1957;209:1269.

[144] K. Otsuka, T. Sawamura, K. Shimizu, physica status solidi (a), 5 (1971) 457-470.

[145] C.J. Bayley, W.A.M. Brekelmans, M.G.D. Geers, International Journal of Solids and Structures, 43 (2006) 7268-7286.

[146] J.C. Fisher, E.W. Hart, R.H. Pry, Acta Metallurgica, 1 (1953) 336-339.

[147] R. Monzen, Y. Kawaguchi, T. Mori, Acta Metallurgica, 30 (1982) 965-972.

[148] K. Okita, N. Okabe, T. Sato, T. Nakao, Materials Transactions, 47 (2006) 753-758.

# VITA

Irfan Kaya was born in 1983 in Izmir, Turkey. He got his bachelor degree from Suleyman Demirel University, Isparta, Turkey. He got the scholarship from Turkish Ministry of National Education throughout graduate education in the USA, 2007. Then he received his degree of Master of Science from Virginia Commonwealth University, Virginia, USA. In August 2010, he was admitted to graduate school at the University of Kentucky. He has been a PhD student at University of Kentucky since 2010. He has published 3 journal articles during his graduate tenure. In addition, he has 1 journal article under review and 4 journal articles to be submitted.